FREQUENCY AND VOLTAGE CONTROL OF A HIGH-PENETRATION, NO-STORAGE WIND-DIESEL SYSTEM

ANDREW G. TOMILSON

Frequency and Voltage Control of a

High-Penetration, No-Storage Wind-Diesel System

by

© Andrew G. Tomilson, BASc., P.Eng.

A thesis submitted to the School of Graduate
Studies in partial fulfilment of the
requirements for the degree of
Master of Engineering

Faculty of Engineering & Applied Science
Memorial University of Newfoundland

July 1998

St. John's Newfoundland Canada

Abstract

Studies have shown that the integration of wind turbines into an autonomous diesel-electric system (i.e., wind-diesel) can be economically viable, and that the potential market for wind-diesel is considerable. *High-penetration, no-storage wind-diesel* (HPNSWD) is considered to be the most economical approach to implementing wind-diesel. A HPNSWD system requires a fast-acting dump load controller to maintain the system frequency stability and quality, and, under some applications, additional voltage control is needed to maintain the voltage quality.

In this thesis a detailed comprehensive dynamic model of a HPNSWD system is presented. The model is implemented in the software packages MATLAB and SIMULINK, and is based on the wind-diesel test-bed at the Atlantic Wind Test Site (AWTS) in PEI, Canada. Simulations using 1st, 2nd and 3rd-order electric machine models are compared with simulations using the full-order electric machine models. Wherever possible, components of the model are validated with available measurements from the AWTS system.

Three different frequency transducers (one phase detector and two frequency detectors) are modelled and incorporated into the design of a PID dump load frequency controller. The fast frequency detector (360 Hz pulse rate) outperforms the phase detector of the same speed. The slow frequency detector (36 Hz pulse rate) is unable to sufficiently dampen the swing of the system against the wind turbine's rotor.

The simulated voltage transients that result from the disconnection of the wind turbine are found to be well above the specified limit. When a capacitor bank is added to the

wind turbine these voltage transients are reduced, but the susceptibility of the system to flicker emissions due to wind turbulence remains high and unchanged.

In this thesis, a static VAR compensator (SVC) is uniquely applied to the wind-diesel system to improve its voltage stability. With the SVC configured to compensate the reactive power of the wind turbine, the wind turbine disconnections yield similar responses as with the capacitor bank, but the flicker emissions due to wind turbulence are virtually eliminated. Adding a novel voltage control loop to the SVC reduces the voltage transients from the wind turbine disconnections to well within the specifications. In addition, the voltage stability of the entire system is improved.

Acknowledgments

The author is deeply indebted to his supervisors: Dr. John Quaicoe, Dr. Ray Gosine, and Dr. Michael Hinchey. In particular, the author would like to thank them for their support, guidance and patience, without which this thesis would not be possible. In addition, the author is grateful to Dr. Neil Bose for his many consultations. Dr. Bose's knowledge of wind turbines has proven invaluable.

The author sincerely appreciates the financial support provided by the Natural Sciences and Engineering Research Council of Canada and the School of Graduate Studies, Memorial University of Newfoundland. Appreciation is also due the Centre for Cold Ocean Resources Engineering for the use of their facilities.

Mr. Carl Brothers at the Atlantic Wind Test Site has been very helpful. He has provided much insight into these studies. The author would also like to thank Mr. Réal Reid and Mr. Bernard Saulnier at Hydro-Québec for their consultations. Mr. David Lombardi at Atlantic Orient Canada Inc., Mr. Don Levy at Westinghouse Canada Inc., Mr. Allen Windhom at Kato Engineering, Mr. Pascal Rembraud at Henry & Fils Ltd., and Mr. Joel Dewall at Barber Colman Company have graciously provided technical information for this thesis.

Much gratitude is due Ms. Cuiyan Ma for her support and encouragement during different phases of this research, and for her editorial assistance in writing this thesis.

Table of Contents

List of Tables

List of Figures

Glossary of Abbreviations and Symbols

1 Abbreviations

AVR	- automatic voltage regulator (used with synchronous generator)
AWTS	- Atlantic Wind Test Site, PEI, Canada
CDN	- Canadian (currency)
CSA	- Canadian Standards Association
EMTP	- Electromagnetic Transients Program (power system simulation)
ETMSP	- Extended Transient-Midterm Stability Program (power system simulation)
FVC	- frequency to voltage converter
HPNSWD	- high-penetration, no-storage wind-diesel
IEC	- International Electrotechnical Commission
IG	- induction generator
IG2f	- 2nd-order induction generator model with fixed saturation
IG2v	- 2nd-order induction generator model with variable saturation
IG4f	- 4th-order induction generator model with fixed saturation
IG4v	- 4th-order induction generator model with variable saturation
PD	- proportional-plus-derivative (control)
PI	- proportional-plus-integral (control)
PID	- proportional-plus-integral-plus-derivative (control)
SG	- synchronous generator
SG1s	- 1st-order synchronous generator model with saturation
SG1u	- 1st-order synchronous generator model without saturation
SG2s	- 2nd-order synchronous generator model with saturation
SG2u	- 2nd-order synchronous generator model without saturation
SG3s	- 3rd-order synchronous generator model with saturation
SG3u	- 3rd-order synchronous generator model without saturation
SG5s	- 5th-order synchronous generator model with saturation
SG5u	- 5th-order synchronous generator model without saturation
SVC	- static VAR compensator
TSR	- tip speed ratio (wind turbine)
US	- United States of America (currency)
VAR	- reactive volt-amperes (power)
WT	- wind turbine
ZCR	- zero-crossing relay

2 Symbols

a_{ef}, B_{ef} - effective windspeed spacial filter parameters
A_{EX}, B_{EX} - exciter saturation function parameters
A_G, B_G - generator magnetic saturation function parameters
B - electrical susceptance (pu)
C_p - wind turbine power coefficient (pu)
D - damping constant (pu)
d_0, d_1, d_2, d_3 - *diesel engine's polynomial torque fit coefficients*
D_d - diesel engine damping constant (pu)
D_{ig} - induction generator and gearbox damping constant (pu)
D_S - wind turbine low-speed shaft torsional damping constant (pu)
D_{sg} - synchronous generator damping constant (pu)
E - generator electromotive force (EMF) (pu)
E_{fd} - synchronous generator field voltage (pu)
$E_{fd.ef}$ - synchronous generator's effective field voltage (pu)
E'_d, E'_q - d and q axis voltage behind transient reactance (pu)
E''_d, E''_q - d and q axis voltage behind subtransient reactance (sec)
f_{sat} - generator magnetic saturation function
G - electrical conductance (pu)
H - inertia constant (sec)
H_d - diesel engine inertia constant (sec)
H_{ig} - induction generator and gearbox inertia constant (sec)
H_{sg} - synchronous generator inertia constant (sec)
H_t - wind turbine's rotor inertia constant (sec)
I - current (pu)
I_B - base current (A)
j - square root of -1
J - moment of inertia ($kg \cdot m^2$)
$K_{1.sg}$, $K_{2.sg}$, $K_{d.sg}$ - synchronous generator 3rd-order model parameters
K_A - AVR amplifier gain
K_c - clutch friction coefficient
K_{cp}, K_{ex} - constant of $C_p(\lambda)$ fit equation
K_{cr} - Ziegler-Nichols critical controller gain
K_d - PID controller's derivative gain
K_{dr} - governor droop constant
K_E - exciter constant
K_F - AVR stabilizer gain
K_g - diesel governor gain
K_i - PID controller's integral gain
K_L - wind turbine induction lag gain
K_p - PID controller's proportional gain
K_S - wind turbine's low-speed shaft torsional spring constant (sec^{-1})

K_v - SVC voltage control gain
m_f - diesel engine fuelling rate (pu)
n - number of diesel engine cylinders
N - diesel engine rotational speed (rpm)
N_g - wind turbine's gearbox ratio
N_T - number of wind turbines
P - active power (W)
P_{Big} - wind turbine's induction generator power rating (W)
P_{cr} - Ziegler-Nichols oscillation period at critical gain
P_{Demand} - demand load power (logistic model)
P_{Diesel} - diesel generator power (logistic model)
P_{Dump} - dump load power (logistic model)
p_{ig} - number of induction generator pole pairs
P_{Loss} - power lost in storage system (logistic model)
P_{m0} - diesel engine base power (W)
P_R -wind turbine's rotor power (pu)
p_{sg} - number of synchronous generator pole pairs
P_{t0} - wind turbine base power (W)
P_{WTG} - wind turbine generator power (logistic model)
Q - reactive power (VAR)
R - electrical resistance (pu)
R_t - radius of the wind turbine's rotor (m)
S - apparent power (VA)
S_{B3} - 3-phase base volt-amperes (VA)
S_{B3sg} - synchronous generator 3-phase volt-ampere rating (VA)
S_E - exciter saturation function
S_G - generator magnetic saturation function
S_T - engine constant: 2 or 4 for a two-stroke or a four-stroke engine, respectively
T_B - base torque (N•m)
T_f - diesel engine undelayed torque (pu)
T_{ig} - induction generator electromagnetic torque (pu)
T_{ig0} - wind turbine high-speed shaft base torque (N•m)
T_m - diesel engine torque (pu)
T_{m0} - diesel engine base torque (N•m)
T_R - wind turbine rotor torque with induction lag (pu)
T_S - wind turbine low-speed shaft torque (pu)
T_{sg} - synchronous generator electromagnetic torque (pu)
T_{t0} - wind turbine low-speed shaft base torque (N•m)
T_W - wind turbine rotor quasi-steady aerodynamic torque (pu)
U_W - effective windspeed over the wind turbine's swept area (m/s)
$\bar{U}_W$ - undisturbed (mean) windspeed (m/s)
U_{Wpt} - point windspeed (m/s)
V - voltage (pu)

V_B - base voltage (V)
V_{oc} - synchronous generator open circuit terminal voltage (pu)
V_R - AVR output voltage (pu)
V_{ref} - AVR reference voltage (pu)
V_{Rmin}, V_{Rmax} - AVR minimum and maximum output (pu)
V_t - synchronous generator terminal voltage (pu)
$W_{Storage}$ - energy content of the storage system (logistic model)
X - electircal reactance (pu)
X_d, X_q - generator d and q axis synchronous reactance (pu)
X_{ig} - induction generator open circuit reactance (pu)
$X_{M.ig}$ - induction generator magnetizing reactance (pu)
X_{md}, X_{mq} - generator d and q axis magnetizing reactance (pu)
X_{mdu} - unsaturated value of X_{md} (pu)
X_{xd} - synchronous generator 3rd-order model parameter
X''_d, X''_q - generator d and q axis subtransient reactance (pu)
X'_d, X'_q - generator d and q axis transient reactance (pu)
X'_{ig} - induction generator open circuit transient reactance (pu)
Y - electrical admittance (pu)
Z - electrical impedance (pu)
Z_B - base impedance (ohms)
β - blade pitch of the wind turbine (deg)
λ - wind turbine's tip speed ratio
λ_0 - tip speed ratio where $C_p(\lambda_0,0) = 0$
ρ - air density (kg/m^3)
τ_{A1}, τ_{A2}, τ_{A3} - AVR amplifier time constants (sec)
τ_{ac} - diesel fuel actuator time constant (sec)
τ_D - diesel engine dead-time (sec)
τ_{DL} - dump load time constant (sec)
τ_{dr} - diesel governor load share module droop time constant (sec)
τ_E - exciter time constant (sec)
τ_{F1}, τ_{F2}, τ_{F3} - AVR stabilizer time constants (sec)
τ_L - wind turbine induction lag time constant (sec)
τ_{p1}, τ_{p2} - diesel governor transfer function poles (sec)
τ_R - AVR input filter time constant (sec)
τ_{svc} - SVC time constant (sec)
τ_v - SVC's voltage transducer time constant (sec)
τ_{z1}, τ_{z2} - diesel governor transfer function zeros (sec)
τ'_0 - induction generator open-circuit transient time constant (sec)
τ'_{d0}, τ'_{q0} - generator d and q axis open-circuit transient time constants (sec)
τ''_{d0}, τ''_{q0} - generator d and q axis open-circuit subtransient time constants (sec)
ψ - generator flux linkage per second (pu)
ψ_B - generator's base flux linkage per second (V)
ω - reference frame angular velocity (pu)

ω_0 - rated grid frequency (electrical rad/s)
ω_B - base frequency (electrical rad/s)
ω_d - diesel engine angular velocity (pu)
ω_{dref} - diesel governor reference speed (pu)
ω_{ig} - induction generator rotor angular velocity (pu)
ω_{ig0} - wind turbine high-speed shaft and IG base angular velocity (mechanical rad/s)
ω_{m0} - diesel engine and SG rotor base angular velocity (mechanical rad/s)
ω_r - synchronous generator rotor angular velocity (pu)
ω_t - angular velocity of the wind turbine's rotor (pu)
ω_{t0} - wind turbine low-speed shaft base angular velocity (mechanical rad/s)

superscripts

^{r} - indicates that the variable is expressed in the rotor reference frame
^{s} - indicates that the variable is expressed in the stator reference frame
^{T} - matrix transpose operation

subscripts

$_{DL}$ - dump load quantity
$_{ds, qs}$ - generator direct and quadrature axis stator windings
$_{dr, qr}$ - generator direct and quadrature axis rotor windings
$_{eq}$ - equivalent admittance quantity
$_{fd}$ - generator field winding (direct axis)
$_{ig}$ - induction generator quantity
$_{l}$ - generator leakage component
$_{m}$ - generator magnetizing component
$_{Le}$ - equivalent load quantity
$_{L}$ - village load quantity
$_{kd, kq}$ - generator direct and quadrature axis rotor damper windings
$_{r}$ - generator rotor quantity
$_{s}$ - generator stator quantity
$_{sg}$ - synchronous generator quantity
$_{TL}$ - transmission line quantity
$_{TR}$ - transformer quantity

Chapter

1 Introduction

1.1 The Potential for Wind-Diesel Systems

There are nearly 400 communities in Canada where, due to immense distances, connection to a major electrical utility grid is impractical [1]. Of these, approximately 170 communities, with a total population of 90,000, lie in regions with good wind resources (>6 m/s average annual windspeed). In industrialized nations such as Canada, most remote communities have their own well established, reliable, autonomous electrical power generation system. The vast majority of these small autonomous grids are supplied by diesel-electric generating plants (diesel generators). Worldwide there are many more such systems. King and Johnson [2] estimated the existing worldwide diesel generating capacity to be 15 GW in regions with at least 6 m/s average annual windspeeds. Furthermore, with the electrification of developing countries such as China, where approximately one third of the population has no electricity supply [3], the number of autonomous, diesel powered grids will increase substantially. The estimated worldwide growth potential through village

electrification in good wind resource areas is greater than 26 GW [2].

Even though diesel generators are reliable and relatively efficient, owing to their remoteness and lack of economies of scale, the cost of supplying electricity with diesel generators to isolated communities is usually very high. In 1992, Hydro-Québec reported an operating deficit of $65.7 million (CDN) to supply electricity to their remote networks (92 MW of installed capacity) [4]. During 1991, it cost 60.41¢/kWh to supply electricity to the 14 Ungava Bay and Hudson Bay communities ($12 million deficit), with the cost of diesel fuel alone being 17.11¢/kWh. In 1993, the fuel costs for these same 14 villages ranged from 11.9 to 16.9¢/kWh [5]. Similarly, Newfoundland and Labrador Hydro reported that 1993's marginal fuel costs ranged from 5.85 to 14.32¢/kWh for 31 of their isolated systems [6]. Because of the high generation costs and the volatility in the price of diesel fuel, alternative sources of electricity are of great interest to remote communities, especially sources that do not rely upon the expensive transportation of fuel over long distances. Since many remote communities are located in coastal regions with excellent wind resources, wind energy is of primary interest.

The oil crisis of the 1970s has renewed interest in the generation of electricity from the wind. As a result of this interest, wind energy technology has matured substantially. The cost of wind generated electricity from commercial scale wind turbines has dropped from 44¢/kWh (US) in 1981, to approximately 8¢/kWh (US) in 1996 [7]. Over the same period, wind turbine availability[1] has improved from 60% to 97-99% [7], and projected operational

---

[1] Availability refers to the percentage of time that the turbine is available, i.e. not shut down for maintenance or repairs.

lifetimes have increased to 20-25 years.

The aforementioned costs refer mainly to grid connected wind farms. Wind turbines and small wind farms in remote locations incur higher construction and maintenance costs due to their diminished accessibility, and higher per unit costs because of their smaller scale. Even with these higher costs, Hydro-Québec's economic studies [4,5,8] have indicated that sites with a good wind resource can be economically viable when operated in conjunction with diesel generation. The estimated cost of wind generated electricity for a northern Québec village with an average wind speed of 7.5 m/s was 9.27¢/kWh (CDN) [4]. This is substantially less than the corresponding 17¢/kWh diesel fuel cost. Hydro-Québec based these calculations only on direct costs, but in one of their studies [5] they also calculated the social costs based on the control costs of atmospheric emissions. Including the return from diminished social costs, their fiscal savings over the life of the project would increase from $2.1 million to $3.7 million. As a result of the recent Kyoto convention on greenhouse gas reductions [9], which also includes the potential for emissions trading, considerable financial rewards for reduced diesel emissions are imminent.

1.2 Overview of Wind-Diesel Systems

Given the significant economic (and environmental) incentives to add wind energy to remote diesel generator systems, the technical aspects must also be addressed.

The peak demand loads of remote communities in Canada typically run from 45 kW to 6.7 MW [5,6]. The installed capacity in the generation plant, typically comprising three

to five diesel generators, is usually large enough (approximately twice the peak demand) to allow for future demand load growth, and to accommodate at least one machine being out of service.

In most modern installations, the sizes of the diesel generator are staggered such that the appropriately sized generator(s) can be engaged to most efficiently meet the demand load at that time. Diesel engine manufacturers advise a minimum operating load of approximately 20 to 40 per cent in order to maintain high fuel efficiency and to avoid excessive fouling and wear.

Wind is a random and highly variable source of energy. The time scales of wind variation range from *long-term* seasonal to hourly fluctuation, down to *short-term* fluctuation in the order of minutes to seconds due to local turbulence (gusts). Long-term wind trends can be forecast from weather patterns and disperse monitoring stations, but no algorithms have yet been found to reliably predict the short-term trends of the wind.

Demand loads also exhibit short-term and long-term frequency trends, but unlike the wind, they are relatively easy to predict (both in frequency and amplitude) since they follow the community's habits. With the knowledge of the demand pattern throughout the day, the load can be anticipated, and the appropriate diesel generation capacity can be brought on line to provide a reliable and optimally efficient supply.

With a significant amount of wind energy in the power mix, it is the short-term fluctuation of the wind that is the greatest impediment to wind-diesel integration. Diesel generators respond rapidly to load variations in order to keep the system's frequency and voltage within an acceptable range. This makes them well suited for operation with wind

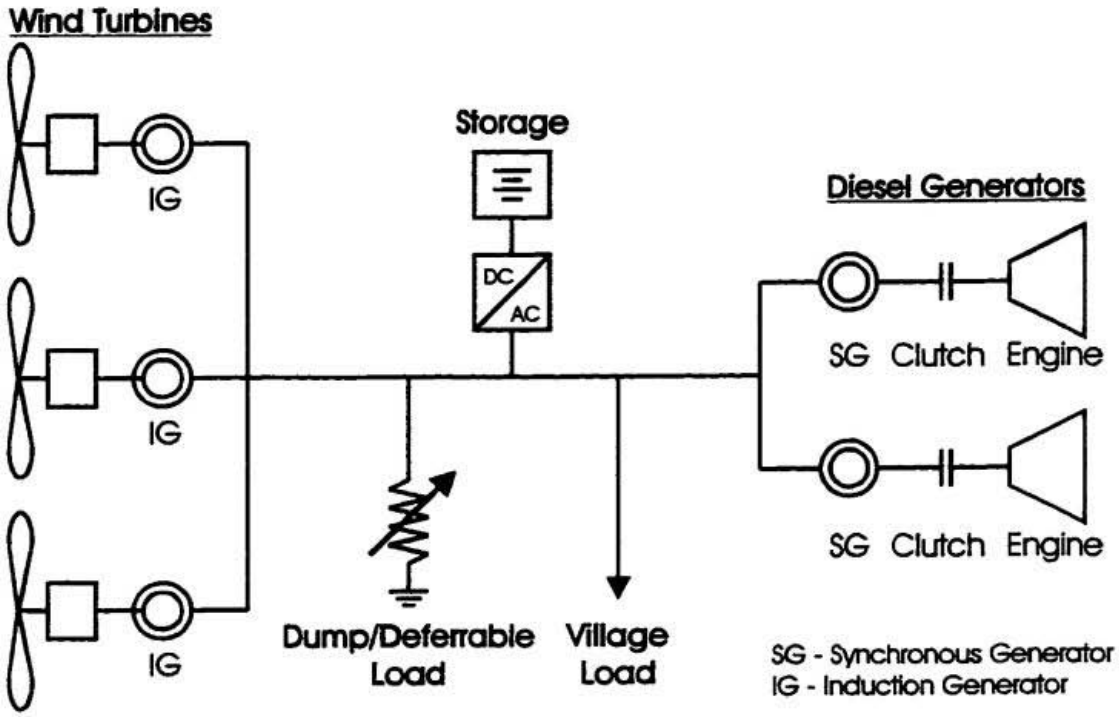

Figure 1.1 General wind-diesel system.

energy while the wind power penetration[2] remains low. With higher levels of penetration, additional controls will be needed to maintain the stability and power quality of the system.

A general wind-diesel system is shown in Figure 1.1. The initial diesel system comprises the diesel generators supplying the village load. With the addition of the wind turbines, a dump load will most likely be needed to absorb the excess energy whenever the generated wind power exceeds the demand. A clutch may be added between the engines and the generators of some, or all, of the diesel generator sets to allow the synchronous generators to operate as synchronous condensers when it is desirable to run exclusively from wind power. In this system the synchronous generators regulate the grid voltage and provide

---

[2] For the purposes of this thesis, penetration is defined as the ratio of the installed wind power capacity to the local peak demand.

the reactive power needed to excite the wind turbines' induction generators. Some form of energy storage in the system may also be justified. The advantages and disadvantages of storage will be discussed later in this section.

A low penetration wind-diesel system (up to 10 to 15%) will not likely use any storage. As long as the instantaneous wind power remains below the demand load, the wind generation will be seen only as a negative load. With the use of a dump load controlled only to absorb excess wind energy, the penetration level for the *negative load scenario* can be increased to a limit of 30 - 40% [8]. The responsibility of system frequency control remains with the diesel generator(s), with the dump load only responding to ensure that the net generation does not exceed the demand. The system can remain within the control range of the diesel generator even though the response time of the dump load controller may be relatively slow compared to that of the diesel generator, since the diesel generator can be momentarily back-driven up to 30% of rated output [10]. Technically, the most significant problem with low penetration is that the diesel will operate more frequently below its minimum load level [11], which, as mentioned earlier, can lead to increased wear and maintenance of the diesel engine .

The economic advantage of low penetration wind-diesel is substantially reduced by the poor fuel efficiency of diesel generators. To demonstrate this, a typical diesel generator fuel consumption curve is shown in Figure 1.2 [12]. The no-load fuel consumption is generally 25 to 30% of the consumption at rated load. If a minimum load of 40% is imposed as a good running practice, only a theoretical maximum of approximately 50% of the fuel can be saved while the diesel is running. For continuous diesel operation, a more realistic

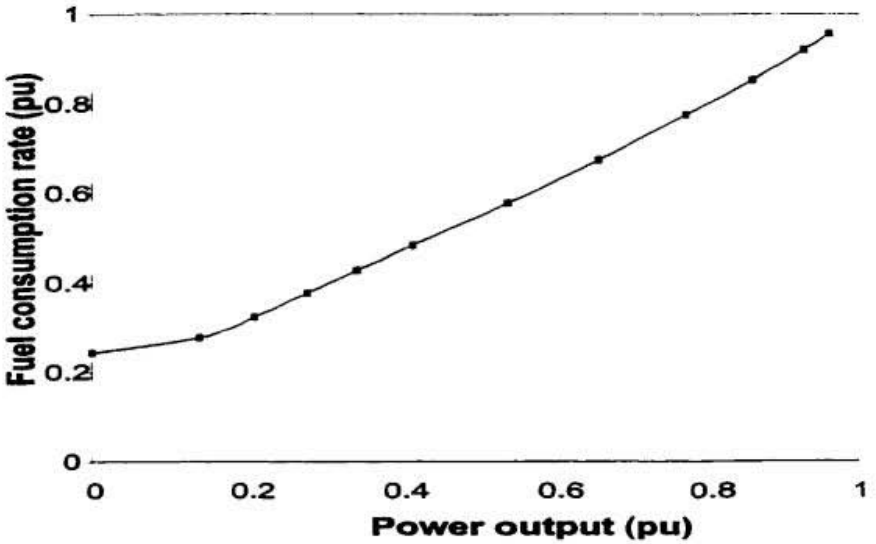

Figure 1.2 Typical diesel generator fuel consumption.

fuel savings would be in the order of 10% [11]. Even with much higher wind energy penetration levels, the fuel savings are only in the range of 15 - 20% for continuous diesel operation [11,13].

Due to the high no-load fuel consumption and the recommended minimum loading of diesel generators, generator fuel consumption can only be greatly decreased by shutting down the diesel engines and running solely from wind power whenever possible. But, because of the stochastic nature of the wind, either some form of storage or very high wind energy penetration is required to avoid frequent start-stops cycles of the diesel generators. Frequent diesel start-stop cycling can cause an unacceptable increase in engine and starter wear, and increased fuel consumption. In addition, intermittent diesel generator operation can also lead to a collapse in system frequency if there is insufficient buffering to allow for the diesel's finite start-up time - which can be in excess of 8 seconds.

Figure 1.3 represents the wind power spectral density measured at Brookhaven, New

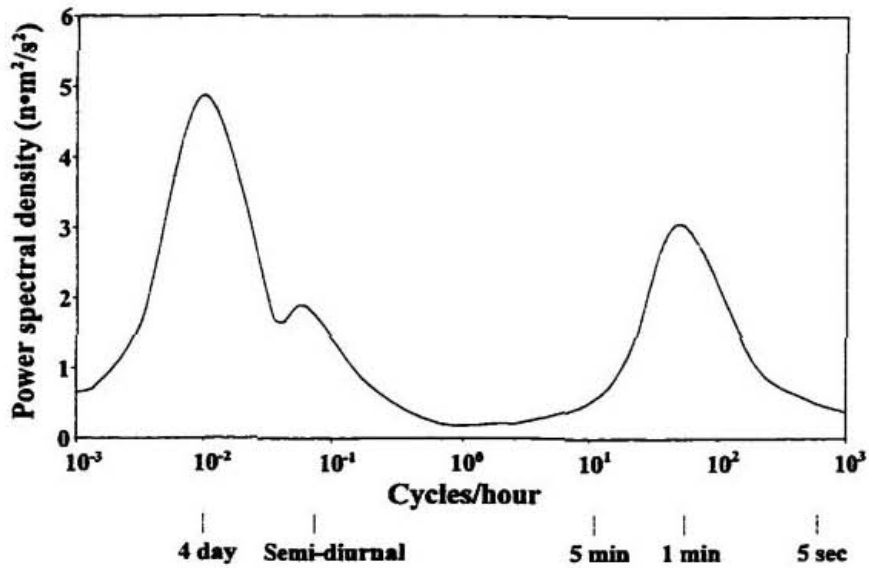

Figure 1.3 Spectrum of horizontal windspeed at Brookhaven, NY.

York [14]. Note the spectral peaks around 1 minute and 4 days, and the spectral gap between approximately 10 minutes and 2 hours. Although this wind spectrum is applicable only to the location where it was measured, it is widely considered to be representative of the general shape and positions of the peaks for the wind spectra of other locations.

Short-term storage is intended to smooth the wind power fluctuations associated with the spectral peak centred at 1 minute. Short-term storage devices such as flywheel storage, can be used to bridge sudden wind power short-falls, with periods of excess wind power being used to recharge the storage medium. Depending on the duration of the short-fall and the state of charge of the storage medium, a diesel generator may be brought on line to make up for longer term wind power short-falls, and, if desired, to recharge the storage medium. *Short-term storage allows practical intermittent diesel operation by greatly reducing the* number of required start-stop cycles. For example, one study on flywheel storage indicated

that the addition of 5 minutes of storage could reduce the number of diesel starts from over 30 starts per hour to nearly 1 start per hour [3]. And in agreement with the spectrum of Figure 1.3, little incremental improvement was found past 5 minutes of storage capacity. In addition, the main effect of the fuel savings were achieved with the first 30 seconds of storage.

Long-term storage is intended to serve as a reservoir for surplus wind energy. This stored energy can then be used during periods of low wind to offset diesel operation. Long-term storage devices such as battery storage, generally have slow energy transfer rates (in the range of 1 to 10 hrs for a complete charge or discharge cycle), whereas much of the energy of concern in wind turbulence lies in the 1 second to 5 minute range. This means that large amounts of long-term storage are needed to meet the short-term energy transfer rates required by the wind-diesel system. Thus, the capital costs of long-term storage become very high. The economic advantage of long-term storage quickly falls with increasing storage times, because the cost of buffering wind energy which is not immediately used quickly exceeds the value of the 'stored energy' in the diesel fuel. Even with very high fuel costs, storage capacity of more than a few hours cannot be economically justified [13].

1.3 High-Penetration, No-Storage Wind-Diesel

The improvements in the operating characteristics of a wind-diesel system made by storage devices tend to be more than offset by their cost and complexity Therefore it is preferable to avoid their use when possible. An alternative to storage for intermittent diesel

operation in a wind-diesel system is very high wind penetration. This is referred to here as *high-penetration, no-storage wind-diesel* (HPNSWD). Economic and technical feasibility studies by Hydro-Québec have determined HPNSWD to be the most favourable approach to implement wind-diesel in Northern Québec [8]. The philosophy behind HPNSWD is that it is more economic to increase the wind energy capacity than it is to add storage to the system. In addition, the excess energy produced by the wind can be sold, at a reduced cost, to low priority loads such as supplementary heating to offset heating fuel. The HPNSWD systems considered by Hydro-Québec have wind energy penetration levels of 50 to 300%, with penetration levels of 100 to 200% being the most economic [4,5,8].

A basic HPNSWD system is the system shown in Figure 1.1 with a clutch installed on at least one diesel generator, a fast acting, highly variable dump load, and no storage devices. Due to the high wind energy penetration, the system will frequently have surplus wind energy generation. This surplus wind power being absorbed by the dump load acts as a spinning reserve to buffer downward fluctuations in wind power and sudden increases in demand.

It is desirable to install a number of smaller wind turbines instead of one large wind turbine. The combination of a high number of wind turbines results in lower short-term wind power fluctuation because localized wind turbulence is smoothed by the spatial dispersion of the wind turbines. For well dispersed wind turbines, the standard deviation of short-term power fluctuations can be reduced by a factor of up to $\sqrt{N_T}$, where N_T is the number of turbines [15]. Hydro-Québec has suggested that a minimum of four turbines be used [5].

In order to maintain the stability of the system, the dump load and dump load

controller must be able to follow rapid fluctuations in the wind turbines' output power. The HPNSWD system will operate in three distinct modes depending on the relative level of wind power to the demand load:

1. The wind power is less than the demand load (negative load scenario). The diesel generator(s) regulates the system frequency.
2. The wind power exceeds the demand load, but the diesel engine(s) is still operating. The diesel(s) and the dump load work in parallel to regulate the system frequency and to maintain a minimum load on the diesel(s).
3. The wind power sufficiently exceeds the demand load to allow all of the diesel engines to be shut down. The dump load is now solely responsible for regulating the system frequency.

The HPNSWD system must be able to smoothly transfer between consecutive modes and maintain a power quality that is as least as good as the original diesel-only system. Power quality is usually determined by the degree of deviation of the frequency and the voltage from their ideal (nominal) values. An additional fast-acting dynamic dump load controller is required to maintain good system frequency stability under all load and wind conditions. With the addition of wind energy, the voltage control of the diesel generator(s) may not be sufficient to maintain the voltage quality in the system. In this case additional voltage control may be needed.

The supervisory controller determines which diesel generators and wind turbines operate according to the demand load and available wind power. The operation of the

supervisory controller is not covered in this thesis.

1.4 Statement of the Problem

The great potential for wind-diesel has been indicated in this chapter, however, as yet, very little of this potential has been realized. The power industry continues to be reluctant to add wind energy to their diesel-electric systems. This is due in part to the fact that the projected economic benefits do not outweigh the risks and uncertainty in implementing a new, unestablished technology. It is anticipated that further study into the technical and practical implementation of wind-diesel will reduce the risks and uncertainty, and thereby encourage the industrial implementation of wind-diesel.

The technical implementation of a low-penetration wind-diesel system is relatively simple, but the return on investment on the wind turbines is low. The return on investment becomes significantly higher with the implementation of high-penetration wind-diesel, especially if no energy storage system is used. However, the technical implementation of a HPNSWD system is considerably more complex.

Low-penetration wind-diesel systems are able to buffer large fluctuations in wind power due to their small size relative to the rest of the system. With high-penetration, the wind power becomes dominant. HPNSWD systems must rely heavily on their frequency and voltage controllers to mask these wind power fluctuations.

The technical problems identified for study in this thesis are more a combination of smaller issues rather than one large one.

Few wind-diesel studies have examined the practical implementation of dump load frequency control in a HPNSWD system. In practice, the dump load may actually be a deferrable load located remotely from the diesel generator. Thus, the dump load controller will have to operate independently of the diesel generator's governor and speed signals.

Fast frequency detection remote from the diesel generator, and its implementation in dump load frequency control in a HPNSWD system, has not been well addressed.

No studies have been found that address the response of a HPNSWD system to large, but normal disturbances such as a wind turbine shut down at full power. The frequency and voltage controllers of the HPNSWD system must be able to maintain satisfactory power quality during these large disturbances.

The voltage control of the synchronous generator may not be able to adequately cope with these large disturbances and the rapid fluctuations in wind power due to wind turbulence. A static VAR compensator (SVC) can be used to improve the voltage stability. This has been suggested [16], but no studies have been found on the implementation of an SVC in a wind-diesel system.

Dynamic wind-diesel models tend to concentrate on detailed mechanical modelling or detailed electrical modelling, but not both. In addition, the justification for choosing particular component models and the modelling parameters are often not given. A more comprehensive study of wind-diesel modelling with a complete set of parameters is needed.

As an extension of this, a wide variety of electric machine models are used in wind-diesel modelling. It has been a general practice to apply reduced-order electric machine models commonly used to represent large machines in interconnected power grids. These

simplifications include the omission of the stator transients and the effects of rotor speed variation, neglecting the damper windings, and, often, neglecting magnetic saturation. Because of the highly stable grid frequency and the large size of the electric machines in large power systems, these simplified models are normally valid. In the case of small electric machines (20 kVA to 2 MVA) connected to small autonomous grids, these simplifications are not always valid.

An extensive study of the different aspects of full-order and reduced-order electric machine models for application in a dynamic wind-diesel model should prove useful for future studies.

1.5 Objectives

Much effort is expended in this research to develop a comprehensive nonlinear dynamic model of a HPNSWD system that includes both a detailed mechanical and a detailed electrical system. It is an objective to clearly identify, and justify, which factors of each system component to include or neglect. All modelling parameters are also clearly indicated for future reference.

Most existing detailed dynamic wind-diesel models are proprietary and/or are developed in simulation packages that are not widely used. Another objective of this study is to develop the model in a simulation package which is broadly used in academia and industry, and in this way, facilitate further studies.

Since one of the main purposes of the model is the development of dynamic control

systems, the simulation package chosen should have a wide variety of tools aimed at controller design. With these points in mind, the numeric computation and visualization software package MATLAB[3] [17] and its associated graphics based dynamic system simulation software, SIMULINK[3] [18], were chosen.

The dynamic model developed in this thesis is based on an actual HPNSWD system in order to simplify the validation of the model, and to ensure that the modelled system reflects a realistic application.

Different electric machine modelling simplifications are implemented in this study and compared with actual results to determine what their effects are on the performance of the overall system model.

With the validity of the HPNSWD dynamic model established, the power quality of the system is studied and research into frequency and voltage control is carried out. The frequency control focusses on the control of the system frequency using a remote dump/deferrable load. This involves modelling various fast electrical frequency transducers.

The voltage control studies include the existing voltage control system and the unique application of a static VAR compensator to improve the voltage stability.

Rapid windspeed fluctuations and wind turbine disconnections under full and no power are used to simulate the large disturbances a HPNSWD system would normally encounter.

---

[3] MATLAB and SIMULINK are registered trademarks of The Math Works, Inc.

1.6 Thesis Outline

This section provides an outline of the remaining chapters of this thesis. Chapter 2 comprises a review of the existing wind-diesel models. It begins by distinguishing between logistic and dynamic wind-diesel modelling. Then a brief overview of logistic modelling is presented along with references to some of the significant work in this area. Next, categories for dynamic wind-diesel models are defined, followed by an in-depth review of the current dynamic wind-diesel models.

Chapter 3 presents the comprehensive nonlinear dynamic HPNSWD model developed for this thesis. The model is based on the wind-diesel test-bed at the Atlantic Wind Test Site (AWTS) in PEI, Canada. The mechanical and the electrical systems are defined and then modelled in detail. A model for each component is introduced and the justification for choosing that model is given. Where applicable, alternative models are considered. In addition, the normalization of the component models are defined. The full-order electric machine models are first determined, and then reduced to a 3rd, 2nd and 1st-order system for the synchronous generator, and a 2nd-order system for the induction generator. The modelling of magnetic saturation is also presented.

A summary of the model validation is found in Chapter 4. The speed and voltage response of the diesel generator model is validated with characterization measurements made by Hydro-Québec. This includes validation of the engine, governor, synchronous generator and voltage regulator models. Only the power curve of the mechanical portion of the wind turbine is validated since no other characterization measurements were available. For this

same reason, the validation of the induction generator models is limited to verifying their steady-state response with a validated model from another study. Validation of the electric machine models also includes comparisons between the full-order and the reduced-order models. Furthermore, the 3rd and 1st-order synchronous generator models are validated with a commercial power system simulation package. The effects of magnetic saturation and fluctuation in rotor speed are also investigated.

Chapter 5 covers the frequency and voltage control of the HPNSWD system. The frequency control section begins by describing the operating modes of the wind-diesel system. The frequency control strategy is then defined, followed by a review of the applicable frequency variation specifications. Models for three fast frequency transducer are presented (one phase detector and two frequency-to-voltage converters). A PID dump load controller is then designed for each of these transducers. The performance of the dump load controllers to load steps and wind turbine disconnections at full output power is illustrated.

The voltage control section of Chapter 5 begins with a review of the applicable voltage variation specifications. The voltage transients due to wind turbine disconnections at full and no output power, and the flicker due to wind turbulence are presented with the synchronous generator as the only source of voltage control. The effects of adding a capacitor bank to the wind turbine is then illustrated. Finally, a dynamic model of a static VAR compensator (SVC) is presented, and its effectiveness in reducing the voltage transients and flicker is demonstrated. This is a unique application of an SVC which has a novel voltage control system. Finally, Chapter 6 summarizes the conclusions of the previous chapters and presents recommendations for further study in the wind-diesel field.

Chapter

2 Review of Wind-Diesel Modelling

Wind-diesel models can be categorized into logistic and dynamic models. Logistic models are generally concerned with the long-term operation of the system and assume that the short-term system dynamics are stable. Dynamic models, on the other hand, mainly address the short-term dynamics of the system. Although this thesis focuses on the dynamic modelling of a HPNSWD system, the logistic modelling of the system is equally important and is briefly reviewed here for completeness and in anticipation of future studies.

The textbook *Wind-Diesel Systems* [10] provides a good overview of wind-diesel modelling techniques. Logistic modelling is well covered, but the dynamic modelling of the small time constants that are required for power quality is not covered in any detail. Infield et al. [19] also provide a good review of the state of significant European logistic and dynamic wind-diesel models as of 1990.

2.1 Wind-Diesel Logistics

In order to determine the viability of a wind-diesel system, the logistics of the system must be evaluated. A logistic model can be used to predict fuel savings and wind energy utilization for an economic assessment, and for the purposes of determining the optimum wind energy penetration and supervisory control. In addition, logistic models can be used to predict the frequency of diesel start-stop cycling and the effects of added storage.

Logistic models of wind-diesel systems can be divided into two main categories: probabilistic models; and time-series models. Probabilistic modelling makes use of the stochastic properties of the wind and the demand load to describe the system in a statistical sense. Chapter 6 of *Wind-Diesel Systems* [10] gives detailed descriptions of the statistical techniques involved in probabilistic wind-diesel modelling. Probabilistic modelling is best suited for analysis of long-term performance ($\geq$ 1 yr.), and as a basis for economic assessment. As an advantage, they do not require detailed physical knowledge of the system components and their interaction, nor do they require long time-series records of the applicable windspeed and demand load. Instead, the model utilizes simplified models that describe the most significant properties of the system components, and the probability distributions of the wind and the load for that particular location.

Time-series logistic models simulate the behaviour of wind-diesel systems to time dependant disturbances. The time-steps are relatively long (ranging from 1 minute to 1 hour). Energy storage of at least one time-step is usually included so that a power balance over each time-step can be assumed. Similar to probabilistic models, time-series logistic models are

commonly used for economic assessments and for long-term performance evaluation of wind-diesel configurations in terms of fuel savings, number of diesel start-stop cycles, dumped energy, etc.

Models with long time-steps require little in terms of system dynamics and can be categorized as quasi steady-state models. Quasi steady-state models are usually based on a simple central power balance equation such as:

$$\frac{dW_{Storage}}{dt} = P_{Diesel} + P_{WTG} - P_{Demand} - P_{Dump} - P_{Loss} \tag{2.1}$$

where, $W_{Storage}$ - energy content of the storage system

P_{Diesel} - diesel generator power

P_{WTG} - wind turbine generator power

P_{Demand} - demand load power

P_{Dump} - dump load power

P_{Loss} - power lost in storage system.

The VINDEC [20] model developed by the Norwegian Research Institute of Energy Supply uses (2.1) as the basis of their long-term performance time-series model. As in similar models, storage must be included in the system, and in this case, the storage must be long-term storage since the time-step chosen for the model is 10 minutes. The 10 minute time-step corresponds to a standard averaging period used for wind data logging.

Quasi steady-state models are useful for estimating long-term power flow. Long-term power flow results can be used to determine the optimal wind turbine size, the optimal size and number of diesel generators, the optimal storage size, and the best supervisory control

strategy. Diesel start-stop frequency can also be predicted, but only if at least one time-step of storage is included. Shorter time-steps are required if systems with short-term storage or no storage are to be analysed.

To make short time-step simulations using long time-step data, the recorded time-series of the windspeed (or demand load) can be subdivided into shorter time-steps. The wind's (or demand load's) statistical data is then used to generate random variation of the intervening time-steps in a realistic manner [10]. The University of Massachusetts' UMLTM quasi steady-state wind-diesel model [21] uses a Markov chain to estimate weekly wind data from the site's seasonal data.

Simulations of wind-diesel systems with short-term storage or no-storage require short time-steps in order to include the effects of local turbulence on the diesel's start-stop frequency and the system's control strategy. McFarlane, Veers and Schluter [22] demonstrated that a noise source with the appropriate wind spectral density, such as the von Karman spectrum, can be used to simulate the high-frequency components of the wind (>2 cycles/hr), which correspond to local turbulence. The simulated turbulence can then be superimposed on the recorded (or estimated) mean windspeed for that interval. This results in a short time-step wind series with the same mean, variance, and power spectral density as the long time-step wind data.

In logistic models, an alternative to subdividing the recorded data time-steps is to perform a time-series simulation for each long time-step (5 min. to 2 hr. steps) and then apply a probabilistic analysis of the variability within each time-step. This is the approach taken by the University of Massachusetts in their Hybrid1 [23] and Hybrid2 [24] hybrid

power systems (wind-diesel-photovoltaic) logistic simulation software. The use of probabilistic analysis within each time step allows the model to be applied to short-term storage and no-storage applications since the expected variations within each time step can be accounted for.

2.2 Wind-Diesel Dynamics

For shorter time steps (in the order of seconds) the dynamic effects of the wind-diesel system become significant. When assessing the stability, power quality, and component sizing of a wind-diesel system, the appropriate system dynamics must be included in the model. Dynamic models for wind-diesel systems can be categorized into three levels:

1. *General Dynamic Mechanical Model* - includes the mechanical equations of motion (diesel and wind turbine accelerations) based on power balances, and may include the rate of power exchange to and from storage . This is an extension of the quasi steady-state logistic model, and is used to study the power match between the wind turbines, the diesel generators, and the demand load. The slower dynamics of speed governing devices may also be included for a first indication of the system's frequency stability and quality. The dynamic mechanical model forms the basis for short-term performance evaluation.

2. *Detailed Dynamic Mechanical, Steady-State Electrical Model* - in addition to the mechanical dynamics, the steady-state electrical equations are also included in the

model. Normally the model includes a more detailed analysis of the diesel engine and wind turbine mechanical dynamics, and the speed governing devices. Gearbox and shaft dynamics may also be included in order to identify any mechanical oscillatory modes. Induction generator slip and/or synchronous generator rotor angles should also be included in the model when looking for mechanical oscillations related to generator interaction. RISØ developed a mechanical wind-diesel model that includes the fundamental generator interaction by connecting two elastic bodies with a damper [25]. The elastic bodies represent the generator rotors and the damper represents the wind turbine's induction generator slip.

The *detailed dynamic mechanical, steady-state electrical model* does not consider the electrical transients of the system. However, since the mechanical transients are generally slower than the electrical transients, this type of model can treat the electrical portion as a quasi steady-state system and still provide an accurate analysis of the system frequency stability and quality. The quasi steady-state electrical model can provide a rough approximation of the voltage quality of the system.

3. *Detailed Dynamic Mechanical and Electrical Model* - both the mechanical and the electrical dynamics are modelled in detail. Electrical dynamic models can be subcategorized into full-order models, and transient and subtransient reduced-order models:

   a. *Transient Electrical Model* - only the transient response of the generators and

other electrical dynamics of that order (50 to 100 milliseconds and greater) are modelled. This level of modelling is only adequate for simulating slow electrical voltage transients, i.e., >100 ms. This level of modelling can identify mechanical oscillations that result from the interaction of the fast mechanical transients (e.g. shaft and gearbox dynamics) and the slow electrical dynamics (e.g. voltage regulation). However, fast transients associated with the connection and disconnection of electrical equipment, and the response of power electronics, such as power converters and fast acting dump loads, cannot be represented at this level.

b. *Subtransient Electrical Model* - this model includes the subtransient (damper winding) response of the generators, but neglects the generators' stator transient responses and the effects of system frequency fluctuation. Generally, time constants are represented down to approximately 10 ms. Transients up to the system frequency can be well represented by this model. However, the voltage transients associated with the rapid fluctuations in system frequency that may occur in an autonomous wind-diesel system are neglected. Also, for small generators, neglecting stator transients may cause significant errors in the model's response to fast transients.

c. *Full-Order Electrical Model* - full-order generator models are employed. The generator models include the subtransients, the stator transients and the effects of frequency variation. Network transients are normally included, but may be neglected for small networks with short transmission lines and for

situations where the frequencies of interest are not very high. Time constants can range down to a few microseconds if high speed switching transients and/or high frequency harmonics due to power electronics are to be analysed.

Detailed dynamic mechanical and electrical models are of interest in this study since the voltage and frequency transients associated with wind turbine disconnections and high frequency wind turbulence are included in the power quality analysis. All three subcategories of the electrical model are analysed to identify which levels of modelling give satisfactory results.

2.2.1 Current Dynamic Wind-Diesel Models

Several dynamic wind-diesel models with varying degrees of detail have been developed to assist in the design and evaluation of both real and hypothetical wind-diesel systems. The most extensive and modular dynamic modelling package to date is the JOule DYnamic MODular MODel (JODYMOD^2) [26,27] developed under the Commission of the European Communities Joint Opportunities for Unconventional or Long-term Energy (CEC JOULE) programme. The JODYMOD^2 model is part of the "Engineering Design Tools for Wind-Diesel Systems" project, which is a cooperative effort between RISØ National Laboratory, Denmark; Rutherford Appleton Laboratories (RAL), UK; Netherlands's Energy Research Foundation (ECN); Norwegian Electric Power Research Institute (EFI); TKK, Finland; and ENEA CRE CASSACIA, Italy.

Their approach in developing JODYMOD^2 was to apply existing models when available. Thus JODYMOD^2 comprises a merger of the participants' existing models. A dynamic model of the user specified wind-diesel system is constructed using model elements from the component library in a manner similar to a finite element technique. The model's component library includes a variety of electrical, electromechanical, mechanical, sensor, controller, signal and input modules. Systems with multiple units of the same type can be modelled, but there are limitations on the numbers of each specific component. The operating environment chosen was the commercial product CYPROS/ESIM. CYPROS/ESIM is a time history simulation package with a number of time integration schemes for first order differential equations. The project negotiated a licensing agreement with the proprietors of CYPROS to cover users in the EC (European Community) and participating EFTA (European Free Trade Association) countries. Alternatively, JODYMOD^2 can be run outside of CYPROS if the user prefers to establish their own environment.

The mechanical components of JODYMOD^2 include rotating machinery such as: wind turbine aerodynamics; drive train, diesel engine and generator assemblies; and flywheel storage. Mechanical structural systems with a maximum of ten degrees of freedom per structure are also included. The mechanical modelling portion of JODYMOD^2 is based on the finite element wind-diesel model developed by RISØ. This dynamic model described by Lundsager et al. [25] includes extensive mechanical modelling, but omits any electrical models.

The electrical portion of the JODYMOD^2 package is based on the Norwegian (EFI) dynamic wind-diesel model named 'VINDI' [28]. The electric machines in VINDI, and thus

JODYMOD², are modelled as voltage behind transient reactance (i.e., *transient electrical model*). Magnetic saturation of the synchronous machine is included in the model. Thus, the JODYMOD² dynamic wind-diesel modelling package comprises extensive mechanical models, but only limited electrical models.

A later publication on electrical modelling at Norway's EFI describes the *transient electrical models* in detail [29]. In this case magnetic saturation of both the synchronous and the induction machines is modelled. The paper focuses on the voltage control of wind-diesel systems and includes models of a compound voltage regulator, an automatic voltage regulator (AVR), and the development of a nonlinear sliding voltage controller. It claims a "satisfactory" agreement between the model simulations and the measurements from the real system was found. The author notes that the magnitudes of the simulated and recorded responses are quite similar, but there appears to be significant differences in the time constants. Similar electric machine models discussed later in this thesis did not give satisfactory results, in the author's opinion, since the generator subtransients were neglected. It is unclear whether these further model developments have been incorporated into JODYMOD², but the research is supported by the same JOULE project.

Further modelling at RISØ with emphasis on the electrical machines is summarized by Infield et al. [19]. These models are referred to as "fully dynamic, based on Park's equations", this most likely means that they are *full-order electrical models*. The latest model was developed in CYPROS. Validation problems incurred with the CYPROS model were accredited to difficulties in modelling voltage regulation due to synchronous generator saturation and incomplete (and difficulty in measuring) electric machine parameters. No

additional information on the models was obtained since the only related publications uncovered in the literature search were two theses written in Danish.

The Netherlands Energy Research Foundation (ECN) has also developed their own dynamic wind-diesel modelling software named 'AWIDIMOD' (Autonomous Wind-Diesel Systems Modelling). Brief descriptions of AWIDIMOD can be found in References 30 and 31. Two separate types of wind-diesel electrical systems can be modelled in AWIDIMOD. One type has a direct electrical connection between the wind turbine's induction generator and the diesel generator's synchronous generator. The other type uses an electrical DC-link to interconnect the wind turbine and the diesel generator, where both of which in this case are equipped with synchronous generators. AWIDIMOD also includes the three modelling levels categorized in Section 2.2.

The mechanical modelling in AWIDIMOD consists of the C_p curves of the wind turbine's rotor; the rotational inertia of the wind turbine's rotor and generator, and of the diesel engine and generator; a freewheel clutch (unidirectional coupling) between the diesel engine and the synchronous generator; a time delay in the fuel control of the diesel; a PID diesel speed controller; equations for the wind turbine's pitch controller and pitching mechanism; and a dynamic model of the flywheel and the flywheel's PI controller. Although the model includes the primary mechanical components, there is no mention in the literature of any torsional dynamics being included in the model. Torsion of the wind turbine's low speed shaft has been found to be an important factor in wind-diesel stability analysis as illustrated in the next chapter.

The third level of modelling in AWIDIMOD includes the *full-order electrical model.*

Elemental tests (constant speed and constant field voltage) were performed to validate the full-order electrical model [31]. With the exception of the fast switching transients, the simulation results were favourable. Although AWIDIMOD is capable of modelling fast electrical transients, Pierik [31] argued that it lacks the modularity and flexibility of JODYMOD^2.

Tsitsovits and Freris presented a comprehensive dynamic model of a high-penetration wind-diesel system in a IEE paper entitled "Dynamics of an isolated power system supplied from diesel and wind" [32]. Their model falls into the *Detailed Dynamic Mechanical and Electrical Model* category. Magnetic saturation of the synchronous generator is included, although they only applied a *transient model* to the electrical system since they were only concerned with slow electrical transients in their study. The detailed equations for both the steady-state and the dynamic model are listed in the appendix of their paper, but none of the model's parameters are given. The mechanical model is quite extensive, with the wind turbine and diesel generator represented by many rotational inertias connected by torsional shafts. The paper presents the development of a system frequency controller that acts jointly on the firing angle of a thyristor controlled resistive dump load and the pitch angle of the wind turbine. The results of the simulations are given, but since the model is based on a hypothetical system, the performance of the model was not validated.

Jeffries also developed a comprehensive wind-diesel system model in his PhD thesis entitled "Analysis and Modelling of Wind/Diesel Systems Without Storage" [33]. The model is intended to be a generic, non-dimensional model that can be used to examine both component and system sizing. The model was developed using the *Advanced Continuous*

Simulation Language (ACSL) simulation software package. ACSL is a text based (as opposed to graphic based) software package with a language similar to FORTRAN.

Jeffries' model can also be classified by the *Detailed Dynamic Mechanical and Electrical Model* category and the *Transient Electrical Model* subcategory. The mechanical dynamic modelling is fairly complete with a C_p curve of the rotor and a torsional low-speed shaft coupling two lumped rotational inertias to represent the wind turbine dynamics; moderate naturally aspirated and turbocharged diesel engine models; and mechanical-hydraulic and electronic diesel speed governor models. System frequency control is limited to the diesel's governor since no dump load or other power control mechanism is incorporated in the model.

Jeffries also sought to identify the typical range of normalized values of the dominant component parameters for a wind-diesel system. Thus, he has provided a good source for determining or estimating model parameters which otherwise may not be readily available.

Stavrakakis and Kariniotakis [34] presented a detailed model of a wind-diesel system capable of simulating multiple diesel generators and wind turbines. The model is a *Detailed Dynamic Mechanical and Electrical Model* with the electrical system modelled at the subtransient level. Magnetic saturation is omitted from the electric machine models. Mechanical models that are slightly more detailed than Jeffries' are proposed in the paper, but the actual models implemented are somewhat simplified — presumably due to a limited availability of component parameters. To reduce the number of differential equations, groups of wind turbines are represented by equivalent aggregate models. The model does not include any dump load or dump load controller. It also appears to be limited to a fixed load for the

duration of the simulation, which would exclude the use of a time varying demand and/or dump load. It is not known whether the modelling platform would allow this to be easily implemented.

Although it was reported to have a high degree of accuracy for "any wind turbine", the analytic C_p function presented proved to give very poor results when the author of this thesis attempted to apply it to the wind turbine used in this thesis. It is also noted that many typographical errors appear in their electric machine equations. These same equations appeared without the errors in an earlier paper in which Stavrakakis and Kariniotakis coauthored with Nogaret and Bordier [35]. Also the model parameters used to represent the same physical system vary dramatically between the two papers.

In the paper, the model is applied to the wind-diesel system on the French island of Desirade with a good agreement between the two measured and simulated responses (one frequency and one voltage). Wind power penetration levels are kept low (below approximately 40%) in the simulations since no dump load is included in the model. Various system perturbations are simulated including balanced faults, wind turbine disconnections, and wind turbulence. This is the only paper which addresses large wind power disturbances, but the penetration levels are low compared to a HPNSWD application.

Kamwa [36] reported on a detailed linear HPNSWD model developed by Hydro-Québec comprising a single diesel generator and a single wind turbine. Although the linear model is based on the flow of real power, it includes a voltage sensitivity term in the diesel generator's power equation; the sensitivity of the system's voltage to frequency; and transfer

functions to represent the AVR, the exciter and the synchronous generator's transient voltage response. The model was implemented in MATLAB and used to demonstrate the effectiveness of a PID dump load controller to regulate the system frequency in a HPNSWD system.

The applicability of the linear model is limited since it is only accurate in the neighbourhood of the nominal operating point (linearization point), and many of the model's parameters must be determined by special identification tests on the components.

Hydro-Québec has extended their HPNSWD modelling with a detailed nonlinear EMTP model [37] of the wind-diesel test-bed at the Atlantic Wind Test Site (AWTS). EMTP (ElectroMagnetic Transients Program) [38] is a powerful software tool widely used in the power system industry to simulate nonlinear electrical systems and electric machines down to the microsecond level. The parameters used in EMTP are values commonly provided by the component manufacturer. Mechanical components cannot be modelled directly and are often converted to their electrical analogues. By all accounts, EMTP is exceptionally time consuming to learn and not very user-friendly.

This is the only study which includes fast frequency detection remote from the diesel generator. Unfortunately, a detailed study of this aspect is not included.

Chapter

3 High-Penetration, No-Storage Wind-Diesel Modelling

3.1 Overview

When modelling a general High-Penetration, No-Storage Wind-Diesel (HPNSWD) system it is convenient to develop a model based on an actual system. A wind-diesel test-bed has been established at the Atlantic Wind Test Site (AWTS), in North Cape, PEI, Canada. This test site was designed, in part, for the evaluation of HPNSWD implementation and control. The AWTS wind-diesel test-bed is representative of the anticipated application of HPNSWD in Canada. Thus, it is a suitable system to model in this study. The AWTS system comprises two 50 kW diesel generators, five wind turbines (totalling 280 kW installed capacity), a 118 kW programmable village load, a 190 kW programmable dump load, and two 62.5 kVA synchronous condensers [39].

Provided the power capacity of the wind turbine is comparable to, or larger than, the diesel generator capacity, a single diesel, single wind turbine configuration of a HPNSWD can

be used to emulate most of the operational range of a HPNSWD system. The operation of a single diesel, single wind turbine configuration can range from: no wind power–with demand load supplied solely by the diesel, to a surplus of wind power (excess power dumped)–with the diesel operating as a synchronous condenser. In addition, a single wind turbine can present a harsher control environment than multiple wind turbines, since multiple wind turbines tend to smooth the effects of wind turbulence. Thus the model can be greatly simplified by reducing the number of generators to one diesel generator and one wind turbine without significantly reducing the model's applicability.

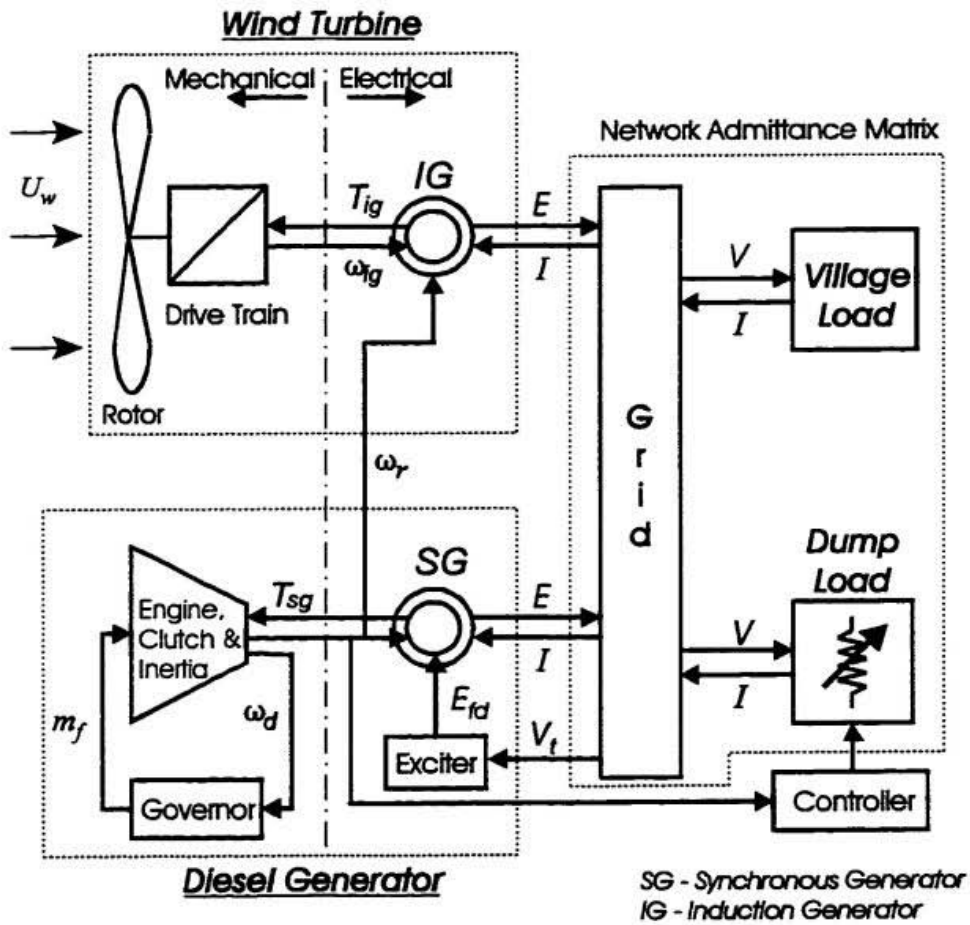

Figure 3.1 Block diagram of the HPNSWD model.

A block diagram of the HPNSWD dynamic model developed in this chapter is shown in Figure 3.1. The signal flow direction, and the division between the mechanical and electrical portions of the model are clearly indicated.

The model of the mechanical systems is intended only to represent the system frequency performance. Thus, most torsional dynamics within the mechanical units are neglected since it is assumed that each stand-alone unit (i.e., diesel generator and wind turbine) is internally stable. Full and reduced-order electric machine models are presented to evaluate the validity of reduced-order models commonly employed in the simulation of the electrical system.

A linear dynamic system can be readily implemented in SIMULINK as a linear state-space equation or a transfer function (Laplace transform). A nonlinear dynamic system can be implemented in SIMULINK by a combination of linear and nonlinear blocks. The full-order dynamic models of the synchronous and induction generators, presented later in this chapter, are good examples of the implementation of nonlinear systems in SIMULINK.

Due to the combination of fast and slow dynamics in the system ('stiff' system), *Gear's* predictor-corrector method [18] was found to be the superior integration algorithm. Although *Gear's method is generally considered* less efficient than the *Runge-Kutta* third and fifth-order methods [18], much larger integration step sizes were possible using *Gear's* method before encountering instability in the solutions.

3.1.1 Normalization

Electric machine parameters are normally quoted as a per unit, or percentage of their respective base quantities, where the base quantities are determined by the operational rating of the machine. Since per unit (pu) quantities are easy to interpret, and electric machine analysis in engineering units can be numerically awkward, it is more convenient to describe models using normalized equations.

For simplicity, the electric generator's base quantities have also been used to normalize the equations for the machinery associated with the generator. For example, the diesel engine model is normalized to the synchronous generator base, thus maintaining a consistency throughout the entire diesel generator set. Likewise, the wind turbine also has its own set of base quantities which are based on the induction generator's rating.

When dealing with the overall system and interconnecting components (i.e., grid, village and dump loads) a separate system base is used. This avoids confusion over which machine base to use when operating at the system level.

Per unit quantities of time and windspeed are more obscure , therefore these two quantities are expressed in their engineering units of seconds and metres per second, respectively. All other variables are normalized to a per unit basis, where the base quantities required for each component are included with the model description.

3.2 Diesel Generator Model - Mechanical

The main components of a diesel generator are the diesel engine, the speed governor,

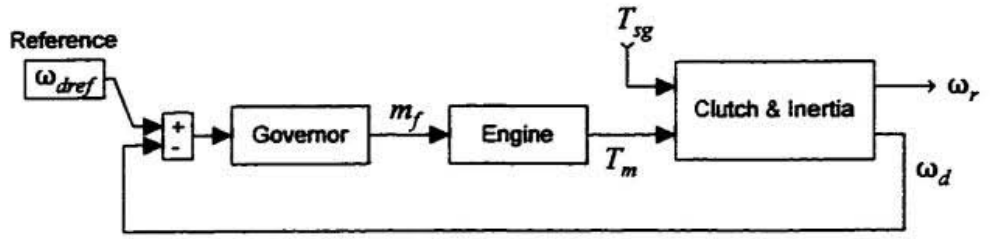

Figure 3.2 General mechanical model of the diesel generator.

the synchronous generator, and the excitation system. In the AWTS system each diesel generator is also fitted with a unidirectional coupling (overrunning clutch) to disengage the engine from the generator. This way, the synchronous generator can act as a synchronous condenser while the system runs solely from wind power.

The mechanical portions of the diesel generator include the engine, the governor, the clutch and the inertias. Figure 3.2 is a general block diagram of the mechanical portion of the diesel generator, where,

m_f - diesel engine's fuelling rate (pu)

T_{sg} - synchronous generator electromagnetic torque (pu)

T_m - engine mechanical torque (pu)

ω_d - engine angular velocity (pu)

ω_r - synchronous generator angular velocity (pu)

ω_{dref} - diesel governor's reference speed (pu).

The diesel generator mechanical model has been divided into three sections: the engine, the clutch and inertia, and the speed governor.

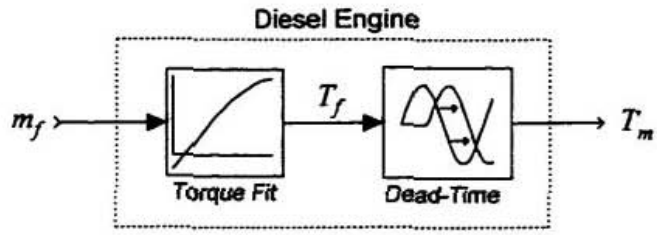

Figure 3.3 Diesel engine dynamic model.

3.2.1 Diesel Engine, Clutch and Inertia

The diesel engine is the prime mover of the synchronous generator. Diesel engines are complicated machines influenced by many factors. Thus models of diesel engines can reach high levels of complexity. Each diesel generator in the AWTS test-bed has a six cylinder, four stroke, naturally aspirated diesel engine. The engines are rated at 75 kW. at 1800 rpm.

More complex models of naturally aspirated diesel engines can be found in References 28, 34 and 35. These models include such factors as the air supply, the combustion efficiency, and the motor chamber pressure. For the purpose of modelling speed transients in a relatively constant environment, a more simplified engine model can be employed. Figure 3.3 represents the simplified diesel engine model used in this study. The engine is modelled by a torque-fit equation and a dead-time (firing delay).

Diesel engine dynamics are commonly represented by a dead-time which represents the delay between the time a change in fuelling is applied (fuel rack movement) and the time when enough cylinders fire to achieve the new torque setting [33,36,40,41,42]. Here, the torque is calculated on an average basis for the engine as a whole. Haddad and Watson [40]

stated that the effective dead-time has been found empirically to be the time between consecutive pistons arriving at the injection point, plus one quarter of the crankshaft revolution. Thus,

$$\tau_D = \frac{60 S_T}{2Nn} + \frac{60}{4N} \tag{3.1}$$

where, τ_D - dead-time in seconds

S_T - 2 or 4 for a two-stroke or a four-stroke engine, respectively

N - engine speed in rpm

n - number of cylinders.

This equation for engine dead-time is consistent with the delay of two power strokes determined by Jeffries [33] to be the average value used in diesel models. For the purposes of this study, the dead-time is considered constant since its speed dependance has negligible effect on the model over the expected speed variation.

Often a nonlinear torque to fuelling rate relationship is included in the model. This study uses a normalized third-order polynomial torque-fit equation (3.2), which was determined by Jeffries [33] to be typical of diesel generators of this rating (9.6 to 236 kW).

$$T_f(m_f) = d_3 m_f^3 + d_2 m_f^2 + d_1 m_f + d_0 \tag{3.2}$$

The coefficients of (3.2) can be found in Appendix B, where the values have been adjusted to correspond to differences in normalization methods. The speed dependancy of the torque is incorporated in the damping constant of the swing equation (3.4).

Mathematically, the transfer function of the diesel engine can be written as,

$$T_m = T_f(m_f)\, e^{-\tau_D s} \tag{3.3}$$

The engine dynamics also encompass the rotational inertias of the engine and the synchronous generator, as well as the dynamics of the clutch which couples the two inertias. Rotational inertia in power systems are commonly represented by the swing equation.

$$\omega_r = \frac{T_m - T_{sg}}{2Hs + D} \tag{3.4}$$

where, H - inertia constant (sec.)

D - damping constant representing windage and speed dependant friction (pu).

This equation is commonly referred to as the *swing equation* because in power systems it represents the swing in the synchronous generator rotor angle during disturbances. The inertia constant, H, is the normalized moment of inertia of the engine and/or generator, thus,

$$H = \frac{1}{2}\frac{J\omega_{m0}^2}{S_{B3}} \tag{3.5}$$

where, J - moment of inertia ($kg \cdot m^2$)

ω_{m0} - base mechanical angular velocity (mechanical rad/s)

S_{B3} - generator 3-phase volt-ampere base (VA).

In this application the engine and the synchronous generator are connected by a unidirectional coupling, or clutch, which only allows power to be transferred from the engine to the generator. The clutch is approximated by a high friction coupling, where the torque is

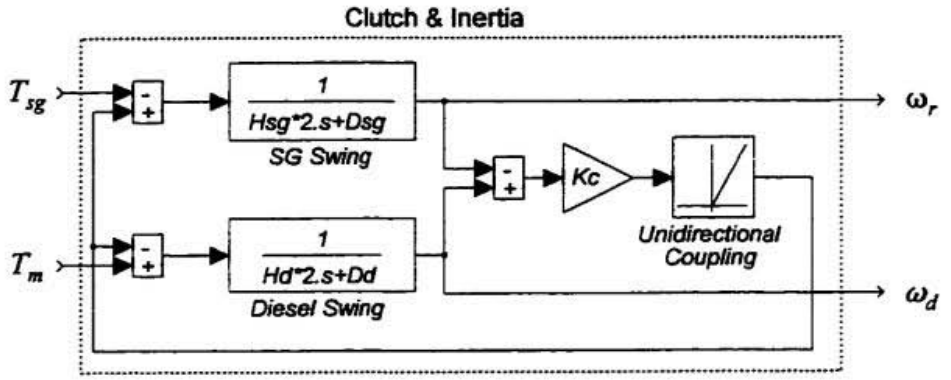

Figure 3.4 Model of the clutch and diesel generator inertias.

limited to zero or greater.

The inertias of the engine and the generator are modelled separately. It is assumed that the shafts coupling the engine and the generator are relatively stiff when compared to the electrical stiffness of the synchronous generator [43]. The torsional modes of the shafts will have frequencies above the range of interest, and, by the necessity of stable diesel generator operation, will be well damped. Therefore, the torsional dynamics of the shafts have been neglected in this study. The model of the diesel inertias and clutch is presented in Figure 3.4, where,

H_{sg} - synchronous generator inertia constant (sec.)

D_{sg} - synchronous generator damping constant (pu)

H_d - engine inertia constant (sec.)

D_d - engine damping constant (pu)

K_c - clutch friction coefficient = 10^3.

3.2.2 Diesel Speed Governor

The diesel speed governor regulates the speed of the diesel engine and, ultimately, the grid frequency since the electrical frequency of a synchronous generator is directly proportional to its speed. This, of course, is true only when the engine and the generator are coupled. If the clutch is decoupled, due to a negative generator torque (motoring), the generator speed will exceed the engine speed, and the grid frequency will no longer be controlled by the governor. The clutch is meant to decouple when the diesel engine is shut down (synchronous condenser mode). But, it is also feasible that the clutch can decouple during concurrent operation of the diesel generator and the wind turbine if the wind power exceeds the combined village load and dump load power. This aspect of the clutch has implications on the dump load controller design and therefore should not be neglected.

Generator speed governors can usually be configured to operate in either droop or isochronous mode. With droop regulation, the steady-state speed decreases in proportion to increased load. Droop is usually expressed in percentage drop in frequency from no-load to full-load. Full-load frequency droop is commonly set in the range of 3% to 6%.

The advantages of droop regulation are twofold: the system is inherently more stable, and multiple generators will intrinsically share the load. The disadvantage of droop regulation is that the grid frequency does not remain at the desired set point (50 or 60 Hz), but varies with the load. Conversely, isochronous regulation maintains the desired steady-state grid frequency irrespective of the load (zero frequency droop), but it is inherently less stable, and an external control is needed to force load sharing between multiple generators.

Speed governors can be any combination of mechanical, hydraulic and electrical

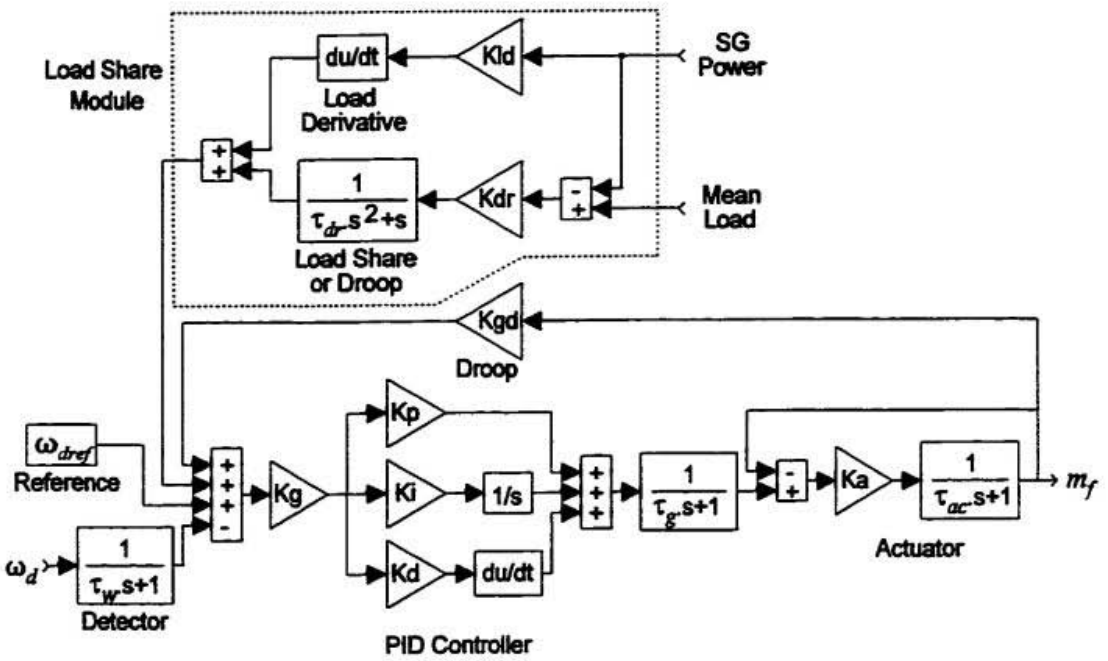

Figure 3.5 Functional diagram of the Barber-Colman governor system.

systems. The diesel generators at AWTS are equipped with electronic governors and electro-mechanically actuated fuel racks. In addition, they are equipped with isochronous load sharing modules. The governors are manufactured by the Barber-Colman Company. A study of the governor schematics and documentation yields the functional diagram in Figure 3.5. This is similar to the electronic governor system described by Haddad and Watson [40]. The main component of the governor is a PID controller, which also includes a proportional feedback loop, K_{gd}, to provide frequency droop according to the actuator position. With an isochronous load sharing module installed, this control loop is disabled ($K_{gd} = 0$), and the frequency droop, in droop mode, is enforced by the isochronous load sharing module.

Implementing this model was not possible because none of the governor's parameters or settings were available. Therefore the governor transfer function has been simplified to

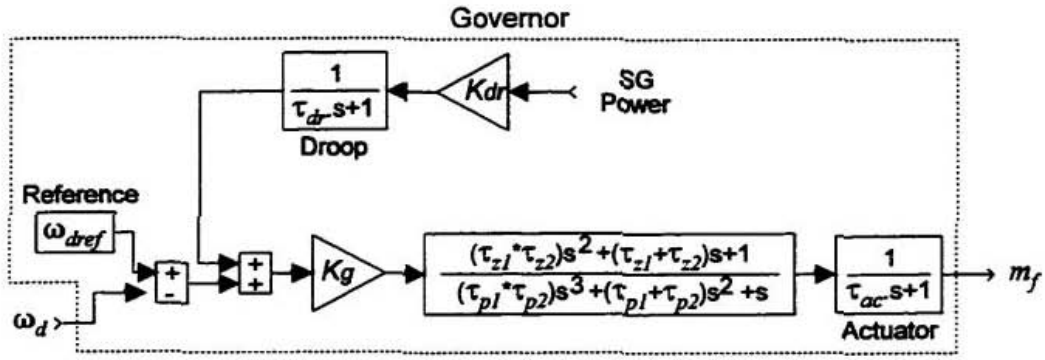

Figure 3.6 Speed governor model (droop mode).

the model represented in Figure 3.6 to facilitate parameter estimation. This model is similar to the model of a Woodward electronic governor used by Kamwa [36]. The isochronous load sharing module has been represented in droop mode for this application. The parameters for this simplified model have been estimated from transient response measurements, as described in Chapter 4, and can be found in Appendix B.

3.2.3 Diesel Generator Normalization

The per unit system of the diesel generator is based on the ratings of the synchronous generator. The base power is equal to the three-phase volt-ampere rating of the generator, and the base speed is the rated grid frequency divided by the number of generator pole pairs. From these two base quantities all the other base quantities can be determined. Thus, the relevant per unit bases are:

$P_{m0} = S_{B3sg}$ - diesel engine base power (W)

$\omega_{m0} = 2\omega_0/p_{sg}$ - diesel's base mechanical angular velocity (mechanical rad/s)

$T_{m0} = P_{m0}/\omega_{m0}$ - diesel engine base torque (N•m)

H_d and H_{sg} - engine and generator inertia constants, determined by (3.5),

where, S_{B3sg} - synchronous generator 3-phase volt-ampere rating

ω_0 - rated grid frequency (electrical rad/s)

p_{sg} - number of synchronous generator poles.

3.3 Wind Turbine Model - Mechanical

The wind turbine model developed here is based on Atlantic Orient Corporation's AOC 15/50 50kW turbine [44,33]. There is one AOC 15/50 wind turbine installed at the AWTS facilities. It is comparable in size to the diesel generator, and was the wind turbine used in a HPNSWD case study by Hydro-Québec [5]. The AOC 15/50 is a horizontal axis, constant speed, stall regulated (fixed-pitch) wind turbine. It contains a single 66 kW induction generator which connects directly to the grid.

The wind turbine is represented by three main components: the rotor aerodynamics; the drive train; and the induction generator. The rotor aerodynamics and the drive train comprise the mechanical portion of the wind turbine model.

3.3.1 Wind Turbine Rotor Aerodynamics

The rotor of the wind turbine converts the kinetic energy of the wind into mechanical energy to drive the induction generator. The wind creates aerodynamic lift and drag forces on the rotor blades which result in a net torque on the wind turbine rotor. The interaction of the wind with the rotor is complex, and is only represented in a simple form in this study.

The rotor's aerodynamics is subdivided into quasi-steady and unsteady aerodynamics.

3.3.1.1 Quasi-Steady Aerodynamics

The slow aerodynamic effects of the wind turbine rotor can be attributed to the performance of the blades to a series of succeeding steady airflow patterns. The airflow over the airfoil of the blade depends on the pitch and velocity of the blade and on the velocity of the wind. Thus the rotor's aerodynamic efficiency, depicted by its power coefficient C_p, can be approximated as a function of the rotor tip speed ratio (TSR), λ, and the blade pitch angle, β. Thus $C_p = f(\lambda,\beta)$, where,

$$\lambda \triangleq \frac{\text{TipVelocity}}{\text{WindVelocity}} = \frac{R_t \omega_t \omega_{t0}}{U_W} \tag{3.6}$$

and, R_t - radius of the turbine rotor (m)

ω_t - angular velocity of the turbine rotor (pu)

ω_{t0} - base angular velocity of the turbine rotor (mechanical rad/s)

U_W - effective windspeed over the turbine's swept area (m/s).

For a fixed-pitch wind turbine, such as the AOC 15/50, the power coefficient becomes a function of the tip speed ratio only.

The non-dimensional power coefficient, $C_p(\lambda)$, can be calculated theoretically [45] or determined experimentally. In this study, the turbine's C_p versus λ curve (Figure 3.7) has been determined from the wind turbine's quoted power curve (Figure 3.8) using the static formula for rotor power [45],

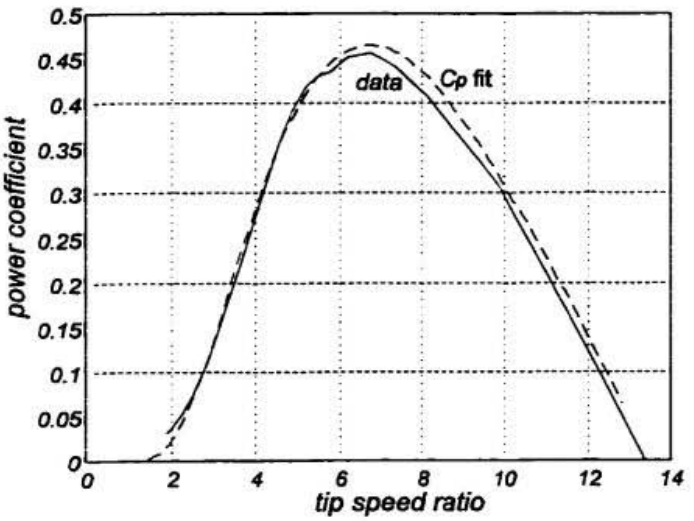

Figure 3.7 Power coefficient curve, $C_p(\lambda)$.

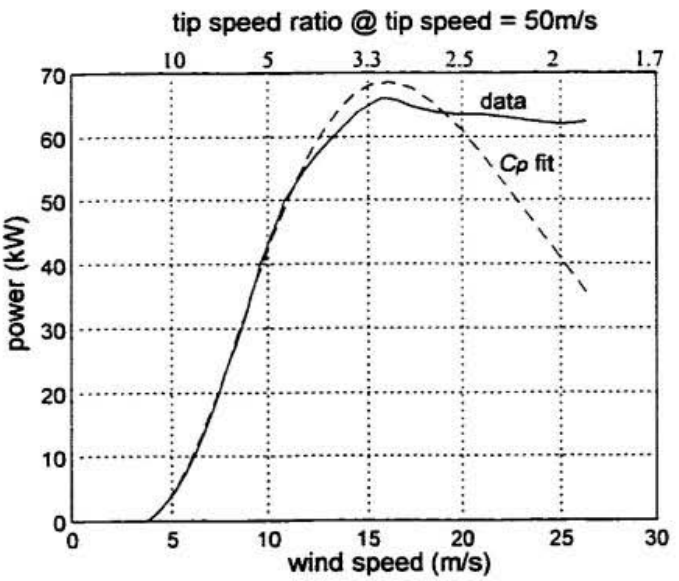

Figure 3.8 Wind turbine power curve.

$$P_R = \frac{1}{2}\rho\pi R_t^2 C_p(\lambda) U_W^3 \quad \text{(W)} \tag{3.7}$$

where, ρ is the air density in kg/m^3.

For the AOC 15/50 wind turbine connected to a strong grid (constant grid frequency), the tip speed increases only slightly (approximately 2%) as the output power increases from zero to maximum, therefore it can be assumed constant for the purpose of calculating the tip speed ratios on the power curve.

In Figure 3.7 and Figure 3.8 two curves are presented. The solid lines represent the curves determined directly from the manufacturer's data [44], and implemented as a look-up table in SIMULINK. The dashed lines represent the results of the C_p curve-fit equation (3.8) used by Jeffries [33]. This is essentially the same equation employed by Wasynczuk et al. [46], and Anderson and Bose [47] to represent the MOD-2 experimental wind turbine. A general version of this equation including blade pitch as a parameter is:

$$C_p(\lambda,\beta) = \frac{K_{cp}}{2}\left(\frac{1}{\lambda} - K_\beta\beta^2 - \frac{1}{\lambda_0}\right)\exp\left(\frac{-K_{ex}K_{cp}}{\lambda}\right) \tag{3.8}$$

where, β - blade pitch (deg.), where $\beta = 0^\circ$ for a fixed-pitch turbine

K_{cp}, K_{ex}, K_β - constants to be determined for best fit

λ_0 - determined from $C_p(\lambda_0, 0) = 0$.

The constants used in Figure 3.7 were: $K_{cp} = 91$, $K_{ex} = 0.147$ and $\lambda_0 = 13.5$. These constants were determined by trial and error with emphasis on low tip speed ratios where the wind power is the greatest. Yet, as Figure 3.8 illustrates, even small errors in $C_p(\lambda)$ at low

tip speed ratios can lead to large errors when determining the power and torque of the rotor. Considering the poor performance of Equation 3.8, a look-up table was determined to be the preferred method for representing $C_p(\lambda)$ in this wind turbine model.

From (3.6) and (3.7), the per unit quasi-steady rotor torque, T_W, is determined by

$$T_W = \frac{\rho \pi R_t^3 \omega_{t0}}{2 P_{Big}} \frac{C_p U_W^2}{\lambda} \quad \text{(pu)} \tag{3.9}$$

where, P_{Big} is the wind turbine's induction generator power rating.

In this study, the turbine is assumed to be pointed directly into the wind at all times. Thus the effects of yaw error, and the turbine's response to fluctuations in wind direction are not considered.

3.3.1.2 Unsteady Aerodynamics

Unsteady aerodynamics is attributed to near field and far field phenomena [48]. Near field phenomena are unsteady effects with lengths of scale in the order of the blade chord length. The most significant near field phenomenon is dynamic stall [45,48]. Analysis of dynamic stall is quite involved and beyond the scope of this study, therefore it is not considered here. Dynamic stall is also not included in any of the wind-diesel models found in the literature search.

Far field unsteady aerodynamic phenomena are effects with lengths of scale in the order of a rotor diameter. One far field phenomenon is referred to as dynamic inflow [48], or induction lag [49,50]. In effect, the wake of a turbine does not adjust instantaneously to

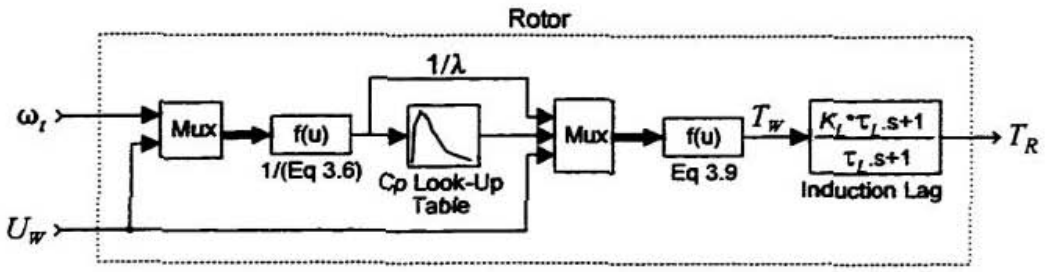

Figure 3.9 Complete aerodynamic model of the wind turbine.

sudden changes in blade pitch or windspeed. As a result, the *induction factors*[4] of the turbine rotor require time to reach a new equilibrium. Induction lag has been found experimentally by Øye [51], and further defined by Bierbooms [48]. Induction lag is represented by a lead transfer function on the rotor torque [49,50,52], thus the resultant rotor output torque, T_R, is:

$$T_R = \frac{1 + K_L \tau_L s}{1 + \tau_L s} T_W; \qquad K_L > 1 \tag{3.10}$$

The induction lag gain, K_L, was found experimentally to be 1.37 [49], and the time constant, τ_L, is estimated [48] by

$$\tau_L = \frac{4R_t}{\bar{U}_W} \tag{3.11}$$

where, $\bar{U}_W$ is the undisturbed (mean) windspeed in metres per second.

The complete aerodynamic model of the wind turbine is shown in Figure 3.9. In this model, division by zero at zero windspeed is avoided by calculating the inverse of the tip speed ratio (1/TSR). Thus the power coefficient look-up table is for $C_p(1/\lambda)$ instead of $C_p(\lambda)$.

---

[4] The *induction factors* refer to the relative magnitudes of the axial and tangential velocities induced in the air flow by the rotor [45,48].

3.3.1.3 Effective Windspeed

The effective windspeed is the equivalent windspeed over the entire rotor swept area (rotor disk). Different points on the rotor disk will see different instantaneous windspeeds due to localized turbulence. Measurements and simulations of instantaneous windspeed normally represent point windspeeds, and thus will differ from the effective windspeed seen by the turbine. The effective windspeed, U_w, is estimated from a point windspeed, U_{wpt}, by the spatial filter [49],

$$U_w = \frac{\sqrt{2} - s\,B_{ef}}{\left(\sqrt{2} - s\,B_{ef}\sqrt{a_{ef}}\right)\left(1 - s\,B_{ef}/\sqrt{a_{ef}}\right)} U_{wpt} \tag{3.12}$$

where, the nominal parameters are $a_{ef} = 0.55$, and

$$B_{ef} = \frac{1.3\,R_t}{\overline{U}_w} \tag{3.13}$$

This spatial filter represents the averaging effect the wind turbine rotor has on higher frequency (local) turbulence. For a 15 m diameter wind turbine, such as the AOC 15/50, the effective low-pass corner frequency ranges from 0.1 to 0.3 Hz, depending on the undisturbed windspeed.

3.3.2 Wind Turbine Drive Train

The wind turbine's drive train is comprised of a gearbox with a low speed shaft connected to the rotor hub, and a high speed shaft connected to the generator. The drive trains of wind turbines are relatively flexible, with the flexibility extending from the

generator, through the gearbox, and hub, and into the blades [43]. Structural models of wind turbines generally use a detailed finite element approach for modelling the drive train. Alternatively, power system studies commonly approximate turbine to generator torsional dynamics by a small number of lumped rotating mass-spring components [53]. Hinrichsen and Nolan [43] claimed that a minimum of two masses should be included in the wind turbine model in order to represent the first torsional and electrical mode. They also claimed that "Addition of the blade mode in horizontal axis turbines by separating hub and blade inertia does not generally change the results, due to high damping of this mode", and "Addition of the high-speed shaft mode by separating generator and transmission inertia is only required if there is need to evaluate torque levels during electrical faults". It is not an objective of this study to analyse fault induced torques, therefore the high-speed shaft torsion dynamics are not considered. This is consistent with the diesel generator model implemented in this study, where the (high-speed) shaft torsional dynamics are also neglected.

Smaller wind turbines, which are suitable for HPNSWD systems, are commonly modelled with two rotating masses in the drive train [33,49,54,55]. The idea of using two masses is further justified by Coonick [55], where his wind-diesel model correctly indicated system instabilities due to an oscillatory mode which included the torsion of the low-speed shaft.

In this study the drive train is represented by separate swing equations (3.5) for the rotor and generator inertia. The two masses are coupled by a flexible low speed shaft which is represented by a lightly damped spring. Thus the transfer function for the shaft torque is:

$$T_S=(\frac{K_S}{s}+D_S)(\omega_t-\omega_{ig}) \tag{3.14}$$

where, T_S - low-speed shaft torque (pu)

K_S - low-speed shaft torsional spring constant (sec^{-1})

D_S - low-speed shaft torsional damping constant (pu)

ω_{ig} - induction generator rotor angular velocity (pu).

Figure 3.10 illustrates the wind turbine drive train model, where,

H_t - wind turbine rotor inertia constant (sec)

H_{ig} - induction generator and gearbox inertia constant (sec)

D_{ig} - induction generator and gearbox damping constant (pu)

T_{ig} - induction generator electromagnetic torque (pu).

Since the drive train model has been normalized, the torque and velocity transformation in the gearbox is not apparent. However, the gearbox ratio must be considered

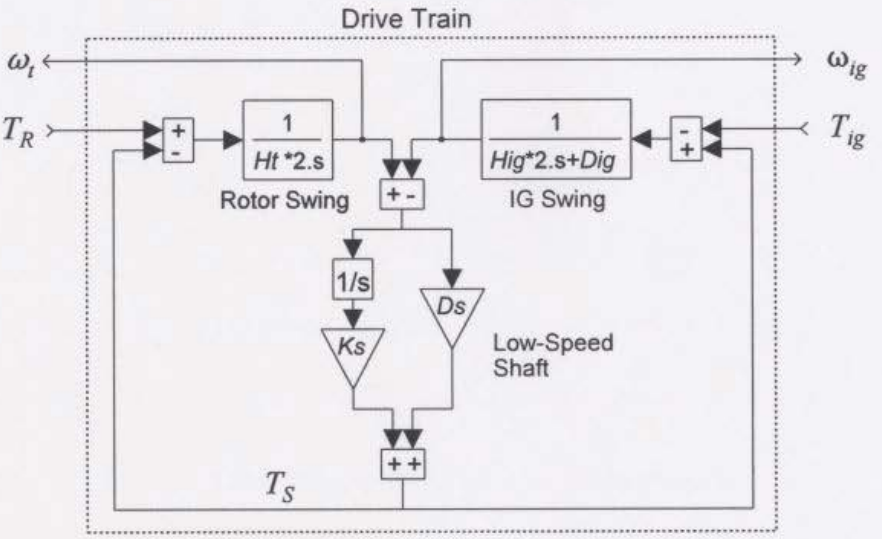

Figure 3.10 Wind turbine drive train model.

when determining the base quantities for normalization of the low-speed and high-speed sides of the gearbox (Section 3.3.3). Backlash in the gearbox has been neglected.

Another factor that is neglected in this model is the effect of tower movement. The dominant effect is the fore and aft movement of the turbine due to the turbine thrust bending the tower [49]. The turbine's fore-aft velocity thus modifies the effective windspeed. It is assumed that the effect of tower movement is small and will not contribute significantly to the wind-diesel dynamics

3.3.3 Wind Turbine Normalization

The per unit system for the wind turbine is based on the rating of its induction generator. The base power is equal to the power rating of the generator. The high-speed shaft base rotational velocity is the rated grid frequency divided by the number of generator pole pairs. The low-speed shaft base rotational velocity is the high-speed shaft base velocity times the gearbox ratio. From these three base quantities all the other base quantities can be determined. Thus the relevant per unit bases are:

$P_{t0} = P_{Big}$ - wind turbine base power (W)

$\omega_{ig0} = 2\,\omega_0/p_{ig}$ - high-speed shaft base angular velocity (mechanical rad/s)

$T_{ig0} = P_{t0}/\omega_{ig0}$ - high-speed shaft base torque (N•m)

$\omega_{t0} = \omega_{ig0}\,N_g$ - low-speed shaft base angular velocity (mechanical rad/s)

$T_{t0} = P_{t0}/\omega_{t0}$ - low-speed shaft base torque (N•m)

H_t and H_{ig} - rotor and generator inertia constants determined by (3.5),

where, P_{Big} - induction generator power rating (W)

p_{ig} - number of induction generator pole pairs

N_g - gearbox ratio.

3.4 Electric Machine Models

The two electric machines in this HPNSWD model are the synchronous generator in the diesel generator, and the induction (asynchronous) generator in the wind turbine. Electrical dynamic models of electric machines vary from linear first-order systems [28], to nonlinear systems of seven, or more, differential equations [56]. It is worth noting that the mechanical equations of the electric machines have already been included in the mechanical model, and thus are not counted in the order of the electric machine models.

In this study, the full-order electric machine models are considered to be the fifth-order synchronous generator model and the fourth-order induction generator model. The full-order models are also reduced to a third, second and first-order synchronous generator model, and a second-order induction generator model for comparison. In addition, the inclusion of magnetic saturation is also presented for comparison.

There are many good textbooks that contain detailed derivations of electric machine models [57,58,59], therefore there is no attempt made here to show the derivation of these models.

3.4.1 Synchronous Generator Models

3.4.1.1 Synchronous Generator Full-Order Model

Synchronous and induction machines are comprised of several magnetic circuits, which are electrically seen as inductances. Some of these machine inductances vary with the rotor position. Thus the coefficients of the differential equations describing the behaviour of the machine vary with time (except when the rotor is stalled). By transforming, or referring, the stator variables of the machine to a reference frame fixed in the rotor, Park [60] transformed the time varying coefficients into constants, thus greatly decreasing the complexity of the differential equations. This change of variables is commonly referred to as Park's transformation. The 3-phase variables of a stationary circuit, such as the stator, may be transformed into a reference frame rotating at an arbitrary speed, ω, by

$$\boldsymbol{f}_{dq0} = \boldsymbol{P}\boldsymbol{f}_{abc} \tag{3.15}$$

where,

$$\boldsymbol{f}_{dq0} \triangleq \left[f_d \;\; f_q \;\; f_0\right]^T \tag{3.16}$$

$$\boldsymbol{f}_{abc} \triangleq \left[f_a \;\; f_b \;\; f_c\right]^T \tag{3.17}$$

$$\boldsymbol{P} \triangleq \frac{2}{3}\begin{bmatrix} \sin\theta & \sin(\theta-\frac{2\pi}{3}) & \sin(\theta+\frac{2\pi}{3}) \\ \cos\theta & \cos(\theta-\frac{2\pi}{3}) & \cos(\theta+\frac{2\pi}{3}) \\ \frac{1}{2} & \frac{1}{2} & \frac{1}{2} \end{bmatrix} \tag{3.18}$$

$$\theta(t) = \int_0^t \omega(\tau)d\tau + \theta(0) \tag{3.19}$$

The *a*, *b* and *c* subscripts stand for the three phases of the stationary circuit, where each one is displaced by 120°. The *d* and *q* subscripts stand for the direct and quadrature axis components of the arbitrary reference frame, respectively. The *0* subscript stands for the zero-sequence component, which is independent of $\theta(t)$. The angular displacement between the two reference frames, $\theta(t)$, must be continuous. However, the angular velocity, $\omega(t)$, may be constant, varying, or zero (stationary). The inverse transform becomes,

$$\boldsymbol{P}^{-1} = \begin{bmatrix} \sin\theta & \cos\theta & 1 \\ \sin(\theta - \frac{2\pi}{3}) & \cos(\theta - \frac{2\pi}{3}) & 1 \\ \sin(\theta + \frac{2\pi}{3}) & \cos(\theta + \frac{2\pi}{3}) & 1 \end{bmatrix} \tag{3.20}$$

For the synchronous generator the *d* axis is defined positive in line with the field winding's north pole, and the *q* axis leads the *d* axis by 90° in the direction of rotation.

Using Park's transformation, the generator's stator windings can be transformed into a direct, a quadrature, and a zero-sequence winding in the rotor reference frame. The zero-sequence circuits are neglected in this study since the zero-sequence currents are assumed to be zero due to balanced three-phase operation. The resulting synchronous generator equivalent circuit, expressed in the rotor reference frame, comprises a stator, a field and a damper winding in the direct axis, and a stator and a damper winding in the quadrature axis. Note that this is a salient-pole synchronous generator model, a cylindrical rotor generator would have an additional rotor winding on the quadrature axis [57,58,59]. Following the derivations in Krause [57], the resulting per unit differential equations describing the generator are:

$$\frac{d\psi^{r}_{qs.sg}}{dt} = \omega_0\left[V^{r}_{qs.sg} - \omega_r\psi^{r}_{ds.sg} + \frac{R_{s.sg}}{X_{ls.sg}}\left(\psi^{r}_{mq.sg} - \psi^{r}_{qs.sg}\right)\right] \tag{3.21}$$

$$\frac{d\psi^{r}_{ds.sg}}{dt} = \omega_0\left[V^{r}_{ds.sg} + \omega_r\psi^{r}_{qs.sg} + \frac{R_{s.sg}}{X_{ls.sg}}\left(\psi^{r}_{md.sg} - \psi^{r}_{ds.sg}\right)\right] \tag{3.22}$$

$$\frac{d\psi^{r}_{kq.sg}}{dt} = \omega_0\left[\frac{R_{kq.sg}}{X_{lkq.sg}}\left(\psi^{r}_{mq.sg} - \psi^{r}_{kq.sg}\right)\right] \tag{3.23}$$

$$\frac{d\psi^{r}_{fd.sg}}{dt} = \omega_0\left[\frac{R_{fd.sg}}{X_{md.sg}}E^{r}_{fd} + \frac{R_{fd.sg}}{X_{lfd.sg}}\left(\psi^{r}_{md.sg} - \psi^{r}_{fd.sg}\right)\right] \tag{3.24}$$

$$\frac{d\psi^{r}_{kd.sg}}{dt} = \omega_0\left[\frac{R_{kd.sg}}{X_{lkd.sg}}\left(\psi^{r}_{md.sg} - \psi^{r}_{kd.sg}\right)\right] \tag{3.25}$$

and,

$$I^{r}_{qs.sg} = -\frac{1}{X_{ls.sg}}\left(\psi^{r}_{qs.sg} - \psi^{r}_{mq.sg}\right) \tag{3.26}$$

$$I^{r}_{ds.sg} = -\frac{1}{X_{ls.sg}}\left(\psi^{r}_{ds.sg} - \psi^{r}_{md.sg}\right) \tag{3.27}$$

$$I^{r}_{kq.sg} = \frac{1}{X_{lkq.sg}}\left(\psi^{r}_{kq.sg} - \psi^{r}_{mq.sg}\right) \tag{3.28}$$

$$I^{r}_{fd.sg} = \frac{1}{X_{lfd.sg}}\left(\psi^{r}_{fd.sg} - \psi^{r}_{md.sg}\right) \tag{3.29}$$

$$I^{r}_{kd.sg} = \frac{1}{X_{lkd.sg}}\left(\psi^{r}_{kd.sg} - \psi^{r}_{md.sg}\right) \tag{3.30}$$

$$\psi^{r}_{mq.sg} = X_{aq.sg}\left(\frac{\psi^{r}_{qs.sg}}{X_{ls.sg}} + \frac{\psi^{r}_{kq.sg}}{X_{lkq.sg}}\right) \tag{3.31}$$

$$\psi^{r}_{md.sg} = X_{ad.sg}\left(\frac{\psi^{r}_{ds.sg}}{X_{ls.sg}} + \frac{\psi^{r}_{fd.sg}}{X_{lfd.sg}} + \frac{\psi^{r}_{kd.sg}}{X_{lkd.sg}} \right) \tag{3.32}$$

$$X_{aq.sg} \triangleq \left(\frac{1}{X_{mq.sg}} + \frac{1}{X_{ls.sg}} + \frac{1}{X_{lkq.sg}} \right)^{-1} \tag{3.33}$$

$$X_{ad.sg} \triangleq \left(\frac{1}{X_{md.sg}} + \frac{1}{X_{ls.sg}} + \frac{1}{X_{lfd.sg}} + \frac{1}{X_{lkd.sg}} \right)^{-1} \tag{3.34}$$

$$T_{sg} = \psi^{r}_{ds.sg} I^{r}_{qs.sg} - \psi^{r}_{qs.sg} I^{r}_{ds.sg} \tag{3.35}$$

where, ψ - generator flux linkages per second (pu)

V - generator voltage (pu)

I - generator current (pu)

E - generator electromotive force (EMF) (pu)

R - winding resistance (pu)

X - winding reactance (pu)

superscript: ^{r} - variable expressed in rotor reference frame

subscripts: $_{ds, qs}$ - direct and quadrature axis stator windings, respectively

$_{fd}$ - field winding (direct axis)

$_{kd, kq}$ - direct and quadrature axis rotor damper windings, respectively

$_{l, m}$ - leakage and magnetizing components, respectively

$_{r, s}$ - rotor and stator quantities, respectively.

Equations (3.21) through (3.35) describe the full-order model (5th-order) of a salient-pole synchronous generator without magnetic saturation. The model has the flux linkages as

state variables, voltage and rotor speed as input variables, and current and electromagnetic torque as output variables.

It is assumed that only the magnetizing inductances saturate, since the leakage inductances include considerable air-gaps [57,58,59]. Further, in a salient-pole machine, magnetic saturation is considered only in the direct axis, again, due to the considerable air-gap in the quadrature axis. Saturation effects are implemented by adjusting the magnetizing flux linkage in the direct axis, $\psi_{md.sg}$ [57], thus (3.32) is replaced by

$$\psi^{r}_{md.sg} = X_{ad.sg}\left(\frac{\psi^{r}_{ds.sg}}{X_{ls.sg}} + \frac{\psi^{r}_{fd.sg}}{X_{lfd.sg}} + \frac{\psi^{r}_{kd.sg}}{X_{lkd.sg}} \right) - \frac{X_{ad.sg}}{X_{md.sg}} f_{sat}(\psi^{r}_{md.sg}) \tag{3.36}$$

where, $f_{sat}(\psi_{md.sg})$ is a saturation function that represents the difference between the unsaturated and the saturated flux linkage curves. These two curves are assumed to be the same, in per unit, as the air-gap line, and the open-circuit terminal voltage versus field current curve, $V_{oc}(I_{fd})$, respectively (Figure 3.11). Thus the saturation curve is given by

$$f_{sat}(\psi_{md}) = X_{md} I_{fd} - V_{oc}(I_{fd}); \quad \psi_{md} = V_{oc}(I_{fd}) \tag{3.37}$$

The synchronous generator saturation characteristics quoted by the manufacturer is shown in Figure 3.11. The resulting saturation function is shown in Figure 3.12. The saturation function is normally approximated by an exponential function [58,59], S_G, where,

$$S_G(\psi_{md}) = A_G e^{B_G(\psi_{md} - 0.8)} \cong f_{sat}(\psi_{md}) \tag{3.38}$$

The coefficients, A_G and B_G, are determined from two points on the saturation curve, usually at ψ_{md} = 1.0 pu and ψ_{md} = 1.2 pu.

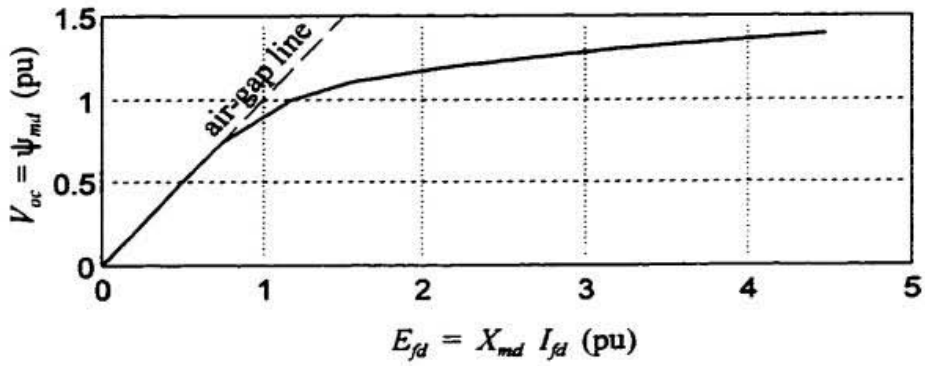

Figure 3.11 Generator open circuit voltage vs. field current.

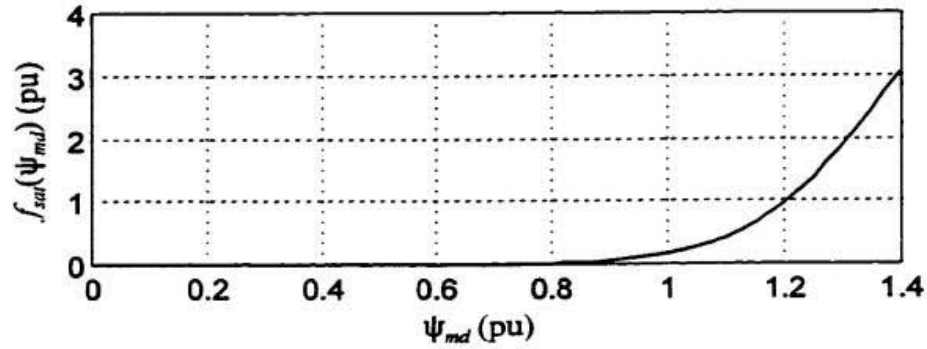

Figure 3.12 Generator saturation function.

The full-order synchronous generator model implementation in SIMULINK can be found in Appendix A.

3.4.1.2 Synchronous Generator Third-Order Reduced Model

Normally power system stability studies neglect the electric transients in the stator voltage equations of all the electric machines, and in the voltage equations of the power system network (transmission lines, transformers, etc.). This reduces the order of the power system model considerably, and since the stator and network transients contain high

frequencies, it also significantly increases the maximum integration step size. The theory of neglecting stator transients is covered in References 57, 58 and 61.

Power system stability studies are primarily interested in the electromechanical dynamics of the (large) electric machines. Whereas in this study, the machines are much smaller, and precise voltage dynamics are also of interest. Krause [57] cautions that "using the reduced-order models for induction and synchronous machines in low-power, small-system applications may not be advisable" and "if the machines are small in horsepower or if the machines are operated over a relatively wide frequency range, one should not use the reduced-order model without first comparing its predications of system response to that of the detailed model". With respect to this advice, the full-order and reduced-order electric machine models have been included in this study for comparison.

Stator transients are neglected by setting differential equations (3.21) and (3.22) to zero, as well as neglecting the stator speed terms by setting $\omega_r = 1$ pu in these two equations. Both Krause [61] and Kundur [58] determined that in order to neglect stator transients, both the derivative term and the speed term must be neglected in the stator voltage equations. The model is reduced to a third-order system by replacing (3.21) and (3.22) with the resulting algebraic stator equations,

$$V^r_{qs.sg} = -R_{s.sg} I^r_{qs.sg} + \Psi^r_{ds.sg} \tag{3.39}$$

$$V^r_{ds.sg} = -R_{s.sg} I^r_{ds.sg} - \Psi^r_{qs.sg} \tag{3.40}$$

A more common representation of this reduced-order model is the *voltage behind subtransient reactance* model, where EMF's are defined as the state variables. Normally,

manufacturers quote machine parameters in the form of the synchronous, transient and subtransient reactances and the transient and subtransient time constants. The conversion of this form to the machine winding impedances can be found in References 57, 58 and 59, and Appendix B.

The EMF's, which represent the voltage behind the subtransient reactance, lag behind the flux linkages by 90°, and are defined as:

$$E''^{r}_{q.sg} \triangleq X''_{d.sg} I^{r}_{ds.sg} + \psi^{r}_{ds.sg} \tag{3.41}$$

$$E''^{r}_{d.sg} \triangleq -X''_{q.sg} I^{r}_{qs.sg} - \psi^{r}_{qs.sg} \tag{3.42}$$

$$E'^{r}_{q.sg} \triangleq X'_{d.sg} I^{r}_{ds.sg} + \psi^{r}_{ds.sg} \tag{3.43}$$

where, $E''_{d.sg}$ - d-axis voltage behind subtransient reactance (pu)

$E''_{q.sg}$ - q-axis voltage behind subtransient reactance (pu)

$E'_{q.sg}$ - q-axis voltage behind transient reactance (pu)

$X''_{d.sg}$, $X''_{q.sg}$ - d and q-axis subtransient reactances (pu), respectively

$X'_{d.sg}$ - d-axis transient reactance (pu)

Substituting (3.41) into (3.39), and (3.42) into (3.40) yields the subtransient stator voltage equations,

$$V^{r}_{qs.sg} = E''^{r}_{q.sg} - R_{s.sg} I^{r}_{qs.sg} - X''_{d.sg} I^{r}_{ds.sg} \tag{3.44}$$

$$V^{r}_{ds.sg} = E''^{r}_{d.sg} - R_{s.sg} I^{r}_{ds.sg} + X''_{q.sg} I^{r}_{qs.sg} \tag{3.45}$$

The remaining equations for the third-order synchronous generator model, as determined by Anderson [59] (expressed in the d-q axes defined here), are:

$$E''^{r}_{d.sg} = \frac{(X_{q.sg} - X''_{q.sg})\, I^{r}_{qs.sg}}{1 + \tau''_{q0.sg}\, s} \tag{3.46}$$

$$\psi^{r}_{kd.sg} = \frac{E'^{r}_{q.sg} - (X'_{d.sg} - X_{ls.sg})\, I^{r}_{ds.sg}}{1 + \tau''_{d0.sg}\, s} \tag{3.47}$$

$$E'^{r}_{q.sg} = \frac{E^{r}_{fd} - X_{xd}\, I^{r}_{ds.sg} + K_{d.sg}\, \psi^{r}_{kd.sg}}{(1 + K_{d.sg}) + \tau'_{d0.sg}\, s} \tag{3.48}$$

$$E''^{r}_{qs.sg} = K_{1.sg}\, E'^{r}_{q.sg} + K_{2.sg}\, \psi^{r}_{kd.sg} \tag{3.49}$$

$$T_{sg} = E''^{r}_{ds.sg}\, I^{r}_{ds.sg} + E''^{r}_{qs.sg}\, I^{r}_{qs.sg} - (X''_{d.sg} - X'_{q.sg})\, I^{r}_{ds.sg}\, I^{r}_{qs.sg} \tag{3.50}$$

where,

$$K_{1.sg} \triangleq \frac{X''_{d.sg} - X_{ls.sg}}{X'_{d.sg} - X_{ls.sg}} \qquad K_{d.sg} \triangleq \frac{(X_{d.sg} - X'_{d.sg})(X_{d.sg} - X''_{d.sg})}{(X'_{d.sg} - X_{ls.sg})^2}$$

$$K_{2.sg} \triangleq 1 - K_{1.sg} \qquad X_{xd} \triangleq \frac{(X_{d.sg} - X'_{d.sg})(X''_{d.sg} - X_{ls.sg})}{(X'_{d.sg} - X_{ls.sg})} \tag{3.51}$$

and, $X_{d.sg}$, $X_{q.sg}$ - d and q-axis synchronous reactance (pu), respectively

$\tau''_{d0.sg}$, $\tau''_{q0.sg}$ - d and q-axis open circuit subtransient time constants (sec)

$\tau'_{d0.sg}$ - d-axis open circuit transient time constant (sec).

Saturation of the d axis is approximated by including the saturation function, (3.38), in (3.48), thus,

$$E'^{r}_{q.sg} = \frac{E^{r}_{fd} - X_{xd}\, I^{r}_{ds.sg} + K_{d.sg}\, \psi^{r}_{kd.sg} - S_G(\psi^{r}_{md.sg})}{(1 + K_{d.sg}) + \tau'_{d0.sg}\, s} \tag{3.52}$$

where, from (3.41) and (3.27),

$$\psi^{r}_{md.sg} = E^{''r}_{q.sg} - I^{r}_{ds.sg}(X^{''}_{d.sg} - X_{ls.sg}) \tag{3.53}$$

The third-order reduced synchronous generator model implementation in SIMULINK can be found in Appendix A.

3.4.1.3 Synchronous Generator First-Order Reduced Model

Generator subtransients are fast transients associated with the rotor damper windings. Neglecting these *amortisseur* effects leads to a *voltage behind transient reactance* model [59], which, in the case of a salient pole machine, is a *one-axis* model. The model therefore reduces to one differential equation,

$$E^{'r}_{q.sg} = \frac{E^{r}_{fd} - (X_{d.sg} - X^{'}_{d.sg})\, I^{r}_{ds.sg} - S_G(\psi^{r}_{md.sg})}{1 + \tau^{'}_{d0.sg}\, s} \tag{3.54}$$

where,

$$\psi^{r}_{md.sg} \equiv E^{'r}_{q.sg} - I^{r}_{ds.sg}(X^{'}_{d.sg} - X_{ls.sg}) \tag{3.55}$$

and, the S_G term is omitted to neglect saturation.

The q-axis stator voltage and electromagnetic torque equations become:

$$V^{r}_{q.sg} = E^{'r}_{q.sg} - R_{s.sg}\, I^{r}_{qs.sg} - X^{'}_{d.sg}\, I^{r}_{ds.sg} \tag{3.56}$$

$$T_{sg} = E^{'r}_{qs.sg}\, I^{r}_{qs.sg} - (X^{'}_{d.sg} - X_{q.sg})\, I^{r}_{ds.sg}\, I^{r}_{qs.sg} \tag{3.57}$$

Since there is no rotor winding represented in the q axis, the d-axis stator voltage

must satisfy the quasi-steady equation,

$$V_{d.sg}^{r} + R_{s.sg} I_{ds.sg}^{r} - X_{q.sg} I_{qs.sg}^{r} = 0 \tag{3.58}$$

which is determined by the generator quasi-steady phasor diagram (Figure 3.13).

The first-order reduced synchronous generator model implementation in SIMULINK can be found in Appendix A.

3.4.1.4 Synchronous Generator Second-Order Reduced Model

Dynamic models of cylindrical rotor machines are simplified by neglecting subtransients, and assuming that the transient effects are dominated by the rotor circuits (stator transients neglected). The dominant rotor circuits in a cylindrical machine are the field circuit in the *d* axis, and an equivalent circuit in the *q* axis formed by the solid rotor. These

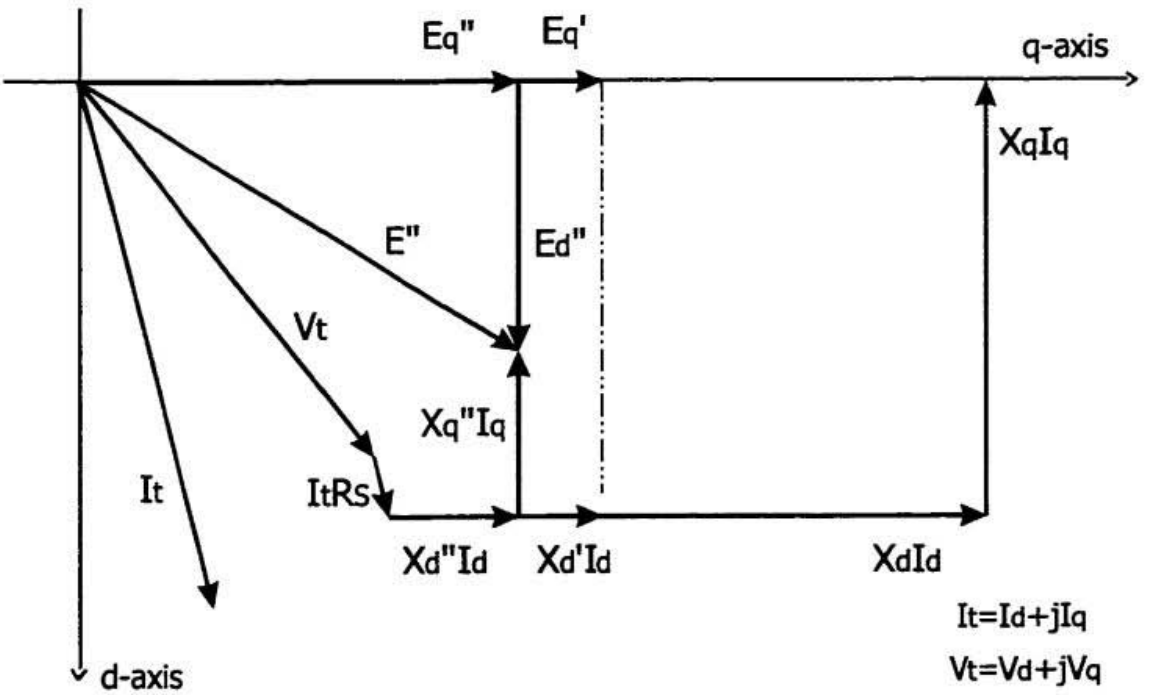

Figure 3.13 Synchronous generator phasor diagram.

assumptions yield a *two-axis, voltage behind transient reactance* model [59].

Salient-pole machines are normally classified as not having a q-axis transient reactance circuit, since the q-axis damper winding is normally classified as a subtransient circuit [58, 59]. In the previous section a 1-axis model was obtained by neglecting the damper windings in both axes, but according to salient-pole machine parameters in Anderson and Fouad [59], the q-axis subtransient time constant can be up to six times larger than the respective d-axis subtransient time constant. In this case, the q-axis damper winding behaves more like a transient circuit than a subtransient circuit. Thus neglecting the q-axis damper winding can give erroneous results, as demonstrated in Chapter 4.

Neglecting the d-axis damper winding and the stator voltage equation transients, but including the q-axis damper winding results in a two-axis, second-order synchronous generator model. Modifying the two-axis model developed in Anderson and Fouad [59], yields the two differential equations,

$$E''^{r}_{d.sg} = \frac{(X_{q.sg} - X''_{q.sg})\, I^{r}_{qs.sg}}{1 + \tau''_{q0.sg}\, s} \tag{3.59}$$

$$E'^{r}_{q.sg} = \frac{E^{r}_{fd} - (X_{d.sg} - X'_{d.sg})\, I^{r}_{ds.sg} - S_G(\psi^{r}_{md.sg})}{1 + \tau'_{d0.sg}\, s} \tag{3.60}$$

the two stator voltage equations,

$$V^{r}_{d.sg} = E''^{r}_{d.sg} - R_{s.sg}\, I^{r}_{ds.sg} + X''_{q.sg}\, I^{r}_{qs.sg} \tag{3.61}$$

$$V_{q.sg}^{r} = E_{q.sg}^{'r} - R_{s.sg} I_{qs.sg}^{r} - X_{d.sg}^{'} I_{ds.sg}^{r} \tag{3.62}$$

and the electromagnetic torque equation,

$$T_{sg} = E_{ds.sg}^{''r} I_{ds.sg}^{r} + E_{qs.sg}^{'r} I_{qs.sg}^{r} - (X_{d.sg}^{'} - X_{q.sg}^{''}) I_{ds.sg}^{r} I_{qs.sg}^{r} \tag{3.63}$$

The second-order reduced synchronous generator model implementation in SIMULINK can be found in Appendix A.

3.4.1.5 Synchronous Generator Normalization

The synchronous generator per unit base quantities are determined by selecting the base power, base voltage and base frequency. Normally these are selected to match the machine ratings. Using these three base quantities, the remaining base quantities can be derived. Thus,

S_{B3sg} = synchronous generator 3-phase volt-ampere rating (W)

V_{Bsg} = peak value of rated phase voltage (V)

ω_{Bsg} = rated frequency = ω_0 (electrical rad/s)

and,

$$I_{Bsg} = \left(\frac{2}{3}\right)\frac{S_{B3sg}}{V_{Bsg}} \quad \text{- peak value of rated phase current (V)}$$

$$Z_{Bsg} = \frac{V_{Bsg}}{I_{Bsg}} \quad \text{- base impedance } (\Omega)$$

$$\omega_{m0} = \frac{2\omega_0}{p_{sg}} \quad \text{- base shaft speed (mechanical rad/s)}$$

$$T_{Bsg} = \frac{S_{B3sg}}{\omega_{m0}} \quad \text{- synchronous generator base torque (N·m)}$$

$$\psi_{Bsg} = V_{Bsg} \quad \text{- base flux linkage per second (V)}$$

3.4.2 Induction Generator Models

3.4.2.1 Induction Generator Full-Order Model

The stator of an induction machine is constructed in much the same manner as the stator of a synchronous machine, but the rotor design is considerably different. The majority of induction machines have cylindrical rotors with conductors imbedded in the ferromagnetic material in the fashion of a squirrel cage. Squirrel-cage rotor windings can be represented by two identical windings, one in the *d* axis and one in the *q* axis. Since both the stator and the rotor are symmetrical, the machine equations are consistent in any arbitrary rotating reference frame. Again, the zero-sequence circuit is neglected in this model, since the zero-sequence current is assumed to be zero due to balanced 3-phase operation. Following the derivations in Krause [57], the resulting per unit differential equations describing the induction generator are:

$$\frac{d\psi_{qs.ig}}{dt} = \omega_0 \left[V_{qs.ig} - \omega\, \psi_{ds.ig} + \frac{R_{s.ig}}{X_{ls.ig}} \left(\psi_{mq.ig} - \psi_{qs.ig} \right) \right] \tag{3.64}$$

$$\frac{d\psi_{ds.ig}}{dt} = \omega_0 \left[V_{ds.ig} + \omega\, \psi_{qs.ig} + \frac{R_{s.ig}}{X_{ls.ig}} \left(\psi_{md.ig} - \psi_{ds.ig} \right) \right] \tag{3.65}$$

$$\frac{d\psi_{qr.ig}}{dt} = \omega_0 \left[-(\omega - \omega_{ig})\, \psi_{dr.ig} + \frac{R_{r.ig}}{X_{lr.ig}} \left(\psi_{mq.ig} - \psi_{qr.ig} \right) \right] \tag{3.66}$$

$$\frac{d\psi_{dr.ig}}{dt} = \omega_0 \left[(\omega - \omega_{ig})\, \psi_{qr.ig} + \frac{R_{r.ig}}{X_{lr.ig}} \left(\psi_{md.ig} - \psi_{dr.ig} \right) \right] \tag{3.67}$$

and,

$$I_{qs.ig} = -\frac{1}{X_{ls.ig}} \left(\psi_{qs.ig} - \psi_{mq.ig} \right) \tag{3.68}$$

$$I_{ds.ig} = -\frac{1}{X_{ls.ig}} \left(\psi_{ds.ig} - \psi_{md.ig} \right) \tag{3.69}$$

$$I_{qr.ig} = \frac{1}{X_{lr.ig}} \left(\psi_{qr.ig} - \psi_{mq.ig} \right) \tag{3.70}$$

$$I_{dr.ig} = \frac{1}{X_{lr.sg}} \left(\psi_{dr.ig} - \psi_{md.ig} \right) \tag{3.71}$$

$$\psi_{mq.ig} = X_{aq.ig} \left(\frac{\psi_{qs.ig}}{X_{ls.ig}} + \frac{\psi_{qr.ig}}{X_{lr.ig}} \right) \tag{3.72}$$

$$\psi_{md.ig} = X_{ad.ig} \left(\frac{\psi_{ds.ig}}{X_{ls.ig}} + \frac{\psi_{dr.ig}}{X_{lr.ig}} \right) \tag{3.73}$$

$$X_{aq.ig} = X_{ad.ig} \triangleq \left(\frac{1}{X_{M.ig}} + \frac{1}{X_{ls.ig}} + \frac{1}{X_{lr.ig}} \right)^{-1} \tag{3.74}$$

$$T_{ig} = \psi_{ds.ig}\, I_{qs.ig} - \psi_{qs.ig}\, I_{ds.ig} \tag{3.75}$$

where, ψ - generator flux linkages per second (pu)

V - generator voltage (pu)

I - generator current (pu)

R - winding resistance (pu)

X - winding reactance (pu)

subscripts: $_{dr,\ qr}$ - d and q-axis rotor windings, respectively

$_{ds,\ qs}$ - d and q-axis stator windings, respectively

$_{l,\ m}$ - leakage and magnetizing components, respectively

$_{r,\ s}$ - rotor and stator quantities, respectively.

Equations (3.64) through (3.75) describe the full-order (4th-order) model of an induction generator without magnetic saturation. The model uses the flux linkages as state variables, has voltage, and rotor and reference frame velocities as input variables, and current and electromagnetic torque as output variables. Generally the model is described in an arbitrary reference frame. For most applications, it is convenient to model the induction generator in the same reference frame as the synchronous generator, thus the synchronous generator's rotor reference frame is used throughout the system model. This is accomplished by setting $\omega = \omega_r$ in the above equations.

It is assumed that the magnetizing inductance, $X_{M.ig}$, saturates in both the d and q axes, and that the leakage inductances do not saturate since they include considerable air-gaps [57]. Saturation effects are implemented by adjusting the magnetizing flux linkages in the d and q axes, $\psi_{md.ig}$ and $\psi_{mq.ig}$ [57], thus (3.72) and (3.73) are replaced by

$$\psi_{mq.ig} = X_{aq.ig}\left(\frac{\psi_{qs.ig}}{X_{ls.ig}} + \frac{\psi_{qr.ig}}{X_{lr.ig}}\right) - \frac{X_{aq.ig}}{X_{M.ig}}\frac{\psi_{mq.ig}}{\psi_{m.ig}} S_G(\psi_{m.ig}) \tag{3.76}$$

$$\psi_{md.ig} = X_{ad.ig}\left(\frac{\psi_{ds.ig}}{X_{ls.ig}} + \frac{\psi_{dr.ig}}{X_{lr.ig}}\right) - \frac{X_{ad.ig}}{X_{M.ig}}\frac{\psi_{md.ig}}{\psi_{m.ig}} S_G(\psi_{m.ig}) \tag{3.77}$$

where,

$$\psi_{m.ig} = \sqrt{\left(\psi_{mq.ig}\right)^2 + \left(\psi_{md.ig}\right)^2} \tag{3.78}$$

and, S_G is a saturation function that represents the difference between the unsaturated flux linkage curve and the saturated flux linkage curve. The saturation curve can be determined from the terminal voltage versus no-load stator current. Thus the saturation function is determined in the same manner as the saturation function for the synchronous generator (Section 3.4.1.1).

The full-order induction generator model implementation in SIMULINK can be found in Appendix A.

3.4.2.2 Induction Generator Second-Order Reduced Model

As mentioned in Section 3.4.1.2, it is standard practice in power system stability studies to neglect the electric transients in the stator voltage equations of all the electric machines, and in the voltage equations of the power system network (transmission lines, transformers, etc).

Stator transients are neglected by setting differential equations (3.64) and (3.65) to zero, as well as neglecting the stator speed terms by setting $\omega = 1$ pu in these two equations.

The second-order reduced model is obtained by replacing (3.64) and (3.65) with the resulting algebraic stator equations,

$$V_{qs.ig} = -R_{s.ig} I_{qs.ig} + \psi_{ds.ig} \tag{3.79}$$

$$V_{ds.ig} = -R_{s.ig} I_{ds.ig} - \psi_{qs.ig} \tag{3.80}$$

A more common representation of this reduced-order model is the *voltage behind transient reactance* model, where EMF's are defined as the state variables. Normally, manufacturers quote induction machine parameters in terms of the stator, rotor and magnetizing winding impedances. The conversion of the machine impedances to the synchronous and transient reactance and the transient time constant can be found in Kundur [58], and Appendix B.

The EMF's, which represent the voltage behind transient reactance, lag behind the flux linkages by 90°, and are defined as:

$$E'_{q.ig} \triangleq X'_{ig} I_{ds.ig} + \psi_{ds.ig} \tag{3.81}$$

$$E'_{d.ig} \triangleq -X'_{ig} I_{qs.ig} - \psi_{qs.ig} \tag{3.82}$$

where, X'_{ig} is the induction generator open circuit transient reactance in per unit.

Substituting (3.81) into (3.79), and (3.82) into (3.80) yields the transient stator voltage equations,

$$V_{qs.ig} = E'_{q.ig} - R_{s.ig} I_{qs.ig} - X'_{ig} I_{ds.ig} \tag{3.83}$$

$$V_{ds.ig} = E'_{d.ig} - R_{s.ig} I_{ds.ig} + X'_{ig} I_{qs.ig} \tag{3.84}$$

The remaining equations for the second-order per unit induction generator model, as determined by Kundur [58], are:

$$E_{q.ig} = \frac{-(X_{ig} - X_{ig}) I_{ds.ig} - \tau_{0.ig}\omega_0(\omega - \omega_{ig}) E_{d.ig}}{1 + \tau_{0.ig} s} \tag{3.85}$$

$$E_{d.ig} = \frac{(X_{ig} - X_{ig}) I_{qs.ig} + \tau_{0.ig}\omega_0(\omega - \omega_{ig}) E_{q.ig}}{1 + \tau_{0.ig} s} \tag{3.86}$$

$$T_{ig} = E_{ds.ig} I_{ds.ig} + E_{qs.ig} I_{qs.ig} \tag{3.87}$$

where. X_{ig} - induction generator open circuit reactance (pu)

$\tau'_{0.ig}$ - induction generator open circuit transient time constant (sec).

Magnetic saturation is approximated by including the saturation function. S_G. in (3.85) and (3.86), thus.

$$E_{q.ig} = \frac{-(X_{ig} - X_{ig}) I_{ds.ig} - \tau_{0.ig}\omega_0(\omega - \omega_{ig}) E_{d.ig} - \dfrac{\psi_{md.ig}}{\psi_{m.ig}} S_G(\psi_{m.ig})}{1 + \tau_{0.ig} s} \tag{3.88}$$

$$E_{d.ig} = \frac{(X_{ig} - X_{ig}) I_{qs.ig} - \tau_{0.ig}\omega_0(\omega - \omega_{ig}) E_{q.ig} - \dfrac{\psi_{mq.ig}}{\psi_{m.ig}} S_G(\psi_{m.ig})}{1 + \tau_{0.ig} s} \tag{3.89}$$

where.

$$\psi_{md.ig} = E_{q.ig} - I_{ds.ig}(X_{ig} - X_{ls.ig}) \tag{3.90}$$

$$\psi_{mq.ig} = -E_{d.ig} - I_{qs.ig}(X_{ig} - X_{ls.ig}) \tag{3.91}$$

$$\psi_{m.ig} = \sqrt{(\psi_{mq.ig})^2 + (\psi_{md.ig})^2} \tag{3.92}$$

The second-order reduced induction generator model implementation in SIMULINK can be found in Appendix A.

3.4.2.3 Induction Generator Normalization

As with the synchronous generator, the base power, base voltage and base frequency are determined by the machine rating. The induction generator differs from the synchronous generator in that the base power is chosen to be the rated shaft power (W), rather than the rated volt-amperes (VA). Thus,

P_{Big} = induction generator rated shaft power (W)

V_{Big} = peak value of rated phase voltage (V)

ω_{Big} = rated frequency = ω_0 (electrical rad/s)

and,

$$I_{Big} = \left(\frac{2}{3}\right)\frac{P_{Big}}{V_{Big}}$$ - peak value of rated phase current (V)

$$Z_{Big} = \frac{V_{Big}}{I_{Big}}$$ - base impedance (Ω)

$$\omega_{ig0} = \frac{2\omega_0}{p_{ig}}$$ - base shaft speed (mechanical rad/s)

$$T_{Big} = \frac{P_{Big}}{\omega_{ig0}}$$ - induction generator base torque (N·m)

$$\psi_{Big} = V_{Big}$$ - base flux linkage per second (V)

3.5 Synchronous Generator Excitation System

The excitation system of the synchronous generator regulates the voltage of the HPNSWD system. The excitation system is comprised of an electronic automatic voltage regulator (AVR) and a brushless exciter. The AVR regulates the terminal voltage of the synchronous generator by adjusting the synchronous generator's excitation level. The brushless exciter is a small 'inside out' synchronous generator on the shaft of the synchronous generator. The field of the exciter is in the stator, and the armature is the rotor. The exciter's armature current is rectified and fed through the synchronous generator's field winding. Thus, the exciter transfers the output of the AVR to the synchronous generator's field winding without the use of brushes.

The AVR's installed on the diesel generators at AWTS are Kato Engineering KCR-360 regulators. The manufacturer has indicated [62] that the KCR-360 can be modelled by the excitation system model type AC5A, of the IEEE Standard 421.5-1992 [63]. Refer to Figure 3.14 for the model representation of the excitation system. The model includes an input filter, a stabilization loop (which feeds back from the AVR output, V_R), and magnetic saturation of the exciter. The exciter is modelled by

$$E_{fd} = \frac{V_R - S_E E_{fd}}{K_E + \tau_E s} \tag{3.93}$$

where, S_E is the exciter saturation function,

$$S_E = f(E_{fd}) = A_{EX} e^{B_{EX} E_{fd}} \tag{3.94}$$

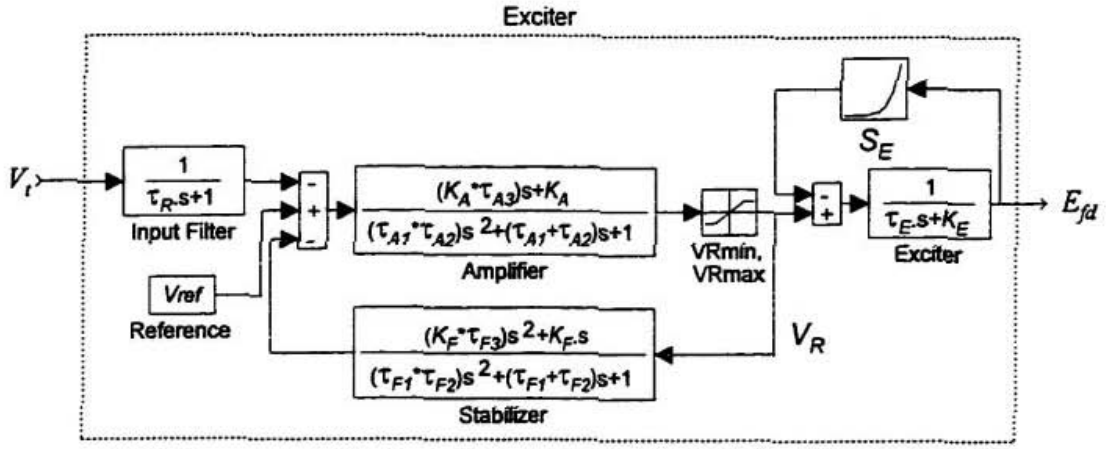

Figure 3.14 IEEE Type AC5A excitation system model.

The coefficients, A_{EX} and B_{EX}, are either given, or can be determined by the method described in Anderson and Fouad [59].

3.5.1 Excitation System Normalization

The excitation system model is normalized to the synchronous generator, such that an output of $E_{fd} = 1$ pu results in a generator open circuit terminal voltage of $V_{oc} = 1$ pu when the generator magnetic saturation is neglected (i.e., one per unit on the air-gap line).

3.6 Wind-Diesel Electrical Network

A wind-diesel electrical network in its simplest form comprises a single electrical bus, or node, to which all the generators and loads are connected. A more complex wind-diesel electrical network comprises a grid of several buses interconnected by finite impedance transmission lines or transformers.

For the purposes of this study the village and dump loads have been represented as passive components. Thus, the loads can be incorporated into one algebraic model to represent the entire electrical network. The algebraic network equations can be solved directly, thus an iterative solution to the network voltages and currents, commonly found in other wind-diesel models, is avoided.

3.6.1 Village Load

In classical power system analysis, the demand load is represented by a constant, passive impedance, hence the village load power is

$$S_L = P_L + jQ_L = Y_L |V_L|^2 \tag{3.95}$$

where,

$$Y_L = G_L + jB_L = Z_L^{-1} = (R_L + jX_L)^{-1} \tag{3.96}$$

The impedance of the village load, Z_L, is assumed constant with respect to voltage and frequency, thus $P_L \propto V^2$ and $Q_L \propto V^2$, and both P_L and Q_L are independent of frequency. This assumption is often on the pessimistic side [59].

3.6.2 Dump Load

At low levels of *instantaneous wind power penetration*[5] the wind turbine is seen as a negative load. At this level the diesel generator maintains the network frequency under

---

[5] *Instantaneous wind power penetration* refers to the ratio of the instantaneous wind power to the instantaneous demand load.

fluctuating wind power and demand load. As the instantaneous wind power penetration increases, the diesel generator loading will be reduced down to its minimum loading. Ideally, beyond this point the dump load, controlled by the dump load controller, begins to dump excess power from the system to maintain the system frequency and minimum diesel loading. Hence, the dump load must be variable and able to absorb the maximum potential surplus power.

The AWTS system contains a controllable resistive dump load comprised of seven, 3-phase heating elements arranged in a binary progression of 1.5, 3, 6,...,48 and 96 kW. Thus the dump load can be varied from 0 to 190.5 kW, in 1.5 kW steps. The model representation of this is a variable resistive load with discrete values at 1.5 kW intervals.

Each 3-phase heating element is connected in a delta configuration with a zero-crossing relay in each branch. The zero-crossing relays introduce a delay of one third to one half of the period of the system frequency. This can be approximated by a time constant, τ_{DL}, equal to one half the period in the dump load.

3.6.3 One-Bus Network Impedance Model

In the AWTS system, the diesel generators, wind turbines, village load and dump load are all within close proximity of each other. The transmission lines of the grid are short, and therefore can be neglected. The resulting network comprises one voltage bus to which all the generators and loads connect directly.

The full-order generator models are equivalent to voltage controlled current sources.

Thus the network is more suitably represented in an impedance form. The one-bus network impedance can be represented by an equivalent single-phase impedance to ground, Z_{Le}, where,

$$Z_{Le} = R_{Le} + jX_{Le} = R_{DL} \| (R_L + jX_L) \tag{3.97}$$

This stationary impedance remains unchanged (speed terms neglected) when referred to an arbitrary reference frame [57], Thus,

$$V = V_d + jV_q \qquad I = I_d + jI_q \tag{3.98}$$

The one-bus impedance network equations, expressed in the synchronous generator's rotor reference frame, are,

$$\begin{bmatrix} V^r_{d.sg} \\ V^r_{q.sg} \end{bmatrix} = \begin{bmatrix} V^r_{d.ig} \\ V^r_{q.ig} \end{bmatrix} = \begin{bmatrix} R_{Le} & -X_{Le} \\ X_{Le} & R_{Le} \end{bmatrix} \begin{bmatrix} I^r_{d.Le} \\ I^r_{q.Le} \end{bmatrix} \tag{3.99}$$

$$\begin{bmatrix} I^r_{d.Le} \\ I^r_{q.Le} \end{bmatrix} = \frac{I_{Bsg}}{I_B} \begin{bmatrix} I^r_{d.sg} \\ I^r_{q.sg} \end{bmatrix} + \frac{I_{Big}}{I_B} \begin{bmatrix} I^r_{d.ig} \\ I^r_{q.ig} \end{bmatrix} \tag{3.100}$$

where, I_B, I_{Bsg} and I_{Big} are the system, synchronous generator and induction generator base currents, respectively, and the load impedance, Z_{Le}, is normalized to the system base.

3.6.4 Multi-Bus Network Admittance Model

Unlike the AWTS system, where all the components are situated in close proximity to one another, a practical application of HPNSWD may have the diesel generators, wind turbines, and village and dump loads located several kilometres apart. In this case the effects

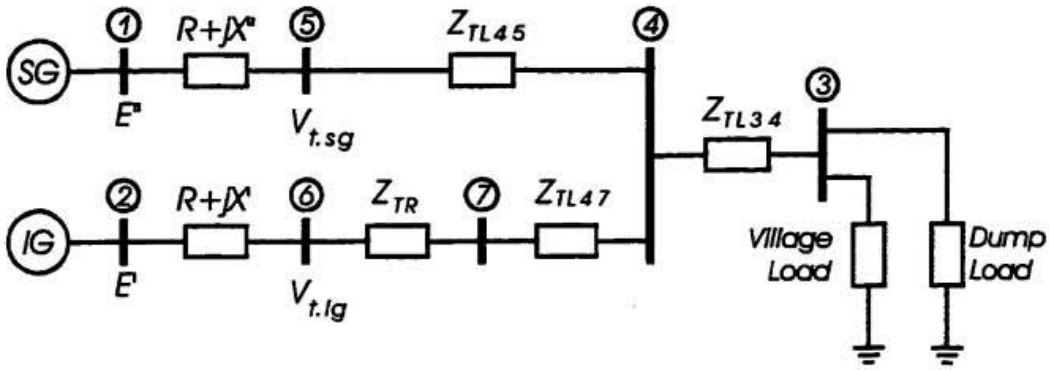

Figure 3.15 AWTS electrical network.

of the transmission lines may be significant. To make the model more general and more easily adapted to other systems, the transmission grid of the AWTS system, shown in Figure 3.15, has also been modelled. The terms Z_{TL} and Z_{TR} refer to the transmission line and transformer impedances, respectively.

The reduced-order, *voltage behind (sub)transient reactance* generator models are equivalent to current controlled voltage sources. Thus the network is more suitably represented in an admittance form. In power flow analysis, a network admittance matrix is the common form for network equations [58,59]. In addition, the admittance matrix lends itself readily to node reduction, which greatly simplifies the network equations, as illustrated in the following analysis.

The network admittance model includes a fictitious bus internal to each generator to represent the EMF behind the (sub)transient reactance (nodes 1 and 2, Figure 3.15). The (sub)transient impedance then becomes part of the network model. In general, for an n-bus network, the node equation is,

$$\mathbf{I} = \mathbf{Y}\,\mathbf{V} \tag{3.101}$$

where

$$\mathbf{I} = \begin{bmatrix} \mathbf{I}_1 & \mathbf{I}_2 & \mathbf{I}_3 & \cdots & \mathbf{I}_n \end{bmatrix}^T \tag{3.102}$$

$$\mathbf{V} = \begin{bmatrix} \mathbf{V}_1 & \mathbf{V}_2 & \mathbf{V}_3 & \cdots & \mathbf{V}_n \end{bmatrix}^T \tag{3.103}$$

$$\mathbf{Y} = \begin{bmatrix} \mathbf{Y}_{11} & \mathbf{Y}_{12} & \mathbf{Y}_{13} & \cdots & \mathbf{Y}_{1n} \\ \mathbf{Y}_{12} & \mathbf{Y}_{22} & \mathbf{Y}_{23} & \cdots & \mathbf{Y}_{2n} \\ \mathbf{Y}_{13} & \mathbf{Y}_{23} & \mathbf{Y}_{33} & \cdots & \mathbf{Y}_{3n} \\ \vdots & \vdots & \vdots & \ddots & \vdots \\ \mathbf{Y}_{1n} & \mathbf{Y}_{2n} & \mathbf{Y}_{3n} & \cdots & \mathbf{Y}_{nn} \end{bmatrix} \tag{3.104}$$

and,

$$\mathbf{I}_i = \begin{bmatrix} I_{di} \\ I_{qi} \end{bmatrix} \qquad \mathbf{V}_i = \begin{bmatrix} V_{di} \\ V_{qi} \end{bmatrix} \tag{3.105}$$

$$\mathbf{Y}_{ij} = \begin{bmatrix} G_{ij} & -B_{qij} \\ B_{dij} & G_{ij} \end{bmatrix} \tag{3.106}$$

where, $\mathbf{I}_i$ - current flowing into the network at node I

$\mathbf{V}_i$ - voltage to ground at node I

$\mathbf{Y}_{ii}$ - driving point admittance for node I

$\mathbf{Y}_{ij}$ - negative of transfer admittance between nodes I and j

G - conductance

B_d, B_q - d and q-axis susceptance, respectively

^{T} - matrix transpose operation.

For the AWTS network, the currents entering nodes 3 through 7 are zero. These nodes can be algebraically eliminated to produce a 2-node, 2-port equivalent admittance matrix.

$$\mathbf{Y}_{eq} = \mathbf{K} - \mathbf{L}\,\mathbf{M}^{-1}\,\mathbf{L}^{T} \tag{3.107}$$

where,

$$\mathbf{K} = \begin{bmatrix} \mathbf{Y}_{11} & \mathbf{Y}_{12} \\ \mathbf{Y}_{12} & \mathbf{Y}_{22} \end{bmatrix} \tag{3.108}$$

$$\mathbf{L} = \begin{bmatrix} \mathbf{Y}_{13} & \mathbf{Y}_{14} & \cdots & \mathbf{Y}_{17} \\ \mathbf{Y}_{23} & \mathbf{Y}_{24} & \cdots & \mathbf{Y}_{27} \end{bmatrix} \tag{3.109}$$

$$\mathbf{L}^{T} = \begin{bmatrix} \mathbf{Y}_{13} & \mathbf{Y}_{23} \\ \mathbf{Y}_{14} & \mathbf{Y}_{24} \\ \vdots & \vdots \\ \mathbf{Y}_{17} & \mathbf{Y}_{27} \end{bmatrix} \tag{3.110}$$

$$\mathbf{M} = \begin{bmatrix} \mathbf{Y}_{33} & \mathbf{Y}_{34} & \cdots & \mathbf{Y}_{37} \\ \mathbf{Y}_{34} & \mathbf{Y}_{44} & \cdots & \mathbf{Y}_{47} \\ \vdots & \vdots & \ddots & \vdots \\ \mathbf{Y}_{37} & \mathbf{Y}_{47} & \cdots & \mathbf{Y}_{77} \end{bmatrix} \tag{3.111}$$

The network equations for the AWTS system using the *voltage behind subtransient reactance* (3rd-order) synchronous generator and the *voltage behind transient reactance* (2nd-order) induction generator models can be expressed as.

$$\begin{bmatrix} I_{d1}^{r} \\ I_{q1}^{r} \\ I_{d2}^{r} \\ I_{q2}^{r} \end{bmatrix} = \mathbf{Y}_{eq} \begin{bmatrix} E_{ds.sg}^{'r} \\ E_{qs.sg}^{''r} \\ E_{ds.ig}^{'r} \\ E_{qs.ig}^{'r} \end{bmatrix} \tag{3.112}$$

where,

$$\begin{bmatrix} I^r_{ds.sg} \\ I^r_{qs.sg} \end{bmatrix} = \frac{I_B}{I_{Bsg}} \begin{bmatrix} I^r_{d1} \\ I^r_{q1} \end{bmatrix} \qquad \begin{bmatrix} I^r_{ds.ig} \\ I^r_{qs.ig} \end{bmatrix} = \frac{I_B}{I_{Big}} \begin{bmatrix} I^r_{d2} \\ I^r_{q2} \end{bmatrix} \tag{3.113}$$

$$\mathbf{Y_{11}} = \frac{S_{B3sg}}{S_{B3}} \begin{bmatrix} R_{s.sg} & -X''_{q.sg} \\ X''_{d.sg} & R_{s.sg} \end{bmatrix}^{-1} \tag{3.114}$$

$$\mathbf{Y_{22}} = \frac{P_{Big}}{S_{B3}} \begin{bmatrix} R_{s.ig} & -X'_{ig} \\ X'_{ig} & R_{s.ig} \end{bmatrix}^{-1} \tag{3.115}$$

When the *2-axis voltage behind transient reactance* (2nd-order) synchronous generator model is used, (3.112) and (3.114) become,

$$\begin{bmatrix} I^r_{d1} \\ I^r_{q1} \\ I^r_{d2} \\ I^r_{q2} \end{bmatrix} = \mathbf{Y_{eq}} \begin{bmatrix} E'^r_{ds.sg} \\ E'^r_{qs.sg} \\ E'^r_{ds.ig} \\ E'^r_{qs.ig} \end{bmatrix} \tag{3.116}$$

$$\mathbf{Y_{11}} = \frac{S_{B3.sg}}{S_{B3}} \begin{bmatrix} R_{s.sg} & -X''_{q.sg} \\ X'_{d.sg} & R_{s.sg} \end{bmatrix}^{-1} \tag{3.117}$$

When the *1-axis voltage behind transient reactance* (1st-order) synchronous generator model is used, (3.112) and (3.114) become,

$$\begin{bmatrix} I_{d1}^{r} \\ I_{q1}^{r} \\ I_{d2}^{r} \\ I_{q2}^{r} \end{bmatrix} = \mathbf{Y}_{eq} \begin{bmatrix} 0 \\ E_{qs.sg}^{'r} \\ E_{ds.ig}^{'r} \\ E_{qs.ig}^{'r} \end{bmatrix} \tag{3.118}$$

$$\mathbf{Y}_{11} = \frac{S_{B3.sg}}{S_{B3}} \begin{bmatrix} R_{s.sg} & -X_{q.sg} \\ X_{d.sg}^{'} & R_{s.sg} \end{bmatrix}^{-1} \tag{3.119}$$

3.6.4.1 Three-Bus Network Admittance Model

The three-bus network admittance model is the admittance equivalent of the one-bus network impedance model. It has three buses, but two of these buses are fictitious buses internal to the generators. The three-bus network admittance model is used in this study for direct comparisons between the reduced-order and the full-order generator models. The three-bus network admittance model is obtained by neglecting the transformer and transmission line impedances in the multi-bus network admittance model (Figure 3.15).

3.6.5 System Normalization

There are three sets of electrical per unit bases: the synchronous generator base, the induction generator base, and the system base. The generator bases were defined in their respective sections. The system per unit base can either be one of the generator bases, or a third separate base. In this study a system base which reflects the system capacity was chosen. The installed diesel generator capacity is 100 kW , and the village load capacity is

118 kW, hence the system base power was selected to be 100 kVA. The system base applies to the interconnecting grid, and the village and dump loads. The system per unit base quantities are determined in the same manner as the generator base quantities, thus.

S_{B3} = system 3-phase volt-ampere base (VA)

V_B = grid's rated peak phase voltage (V)

ω_0 = rated grid frequency (electrical rad/s)

and,

$$I_B = \left(\frac{2}{3}\right)\frac{S_{B3}}{V_B}$$ - peak value of rated grid phase current (V)

$$Z_B = \frac{V_B}{I_B}$$ - system base impedance (Ω)

Chapter

4 Model Validation

To ensure confidence in the AWTS HPNSWD model developed in the previous chapter. the performance of the model is compared with the actual performance of the physical system.

The model parameters were obtained from various sources, including values quoted by the component manufacturers, measurements made by Hydro-Québec [44.39], and parameters cited by Jeffries [33] for the AOC 15/50 wind turbine. Where parameters were not available, estimates were made from parameters for similar equipment. A complete list of the model parameters used in this study can be found in Appendix B.

It was not practical for the author to make measurements on the AWTS system. Therefore characterization and comparative measurements reported by Hydro-Québec [44,39] have been used. A certain amount of uncertainty is introduced this way since configurations for the tests are sometimes vague and must be assumed. In addition, at least one year had passed between the first [44] and the last [39] tests, during which time

adjustments to the system may have been made. Thus comparisons between the two sets of tests may not be valid.

4.1 Diesel Generator Mechanical Model Validation

The speed response of the diesel generator(s) to steps in generator load were reported by Saulnier et al. [39]. These were the only tests available for verifying the diesel generator mechanical model. No intermediate variables were recorded in these tests to verify the individual components, such as the governor, therefore, only the performance of the lumped components can be validated. Characterization of the governor response to a step change in the frequency setting was performed by Jean et al. [44], but it was not specified to which module of the governor system this signal was applied. In addition, the circuit information available for the governor is not detailed enough for this test to be useful in this study.

Parameters for the governor were estimated from the results of the +40 kW (0.64 pu - SG base) and -20 kW (0.32 pu - SG base) load steps applied to Diesel A [39], where the two diesel generators were labelled Diesel A and Diesel B. The parameters for Diesel A (Table 4.1) provide a good match between the simulated and measured responses to a positive load step (Figure 4.1). Conversely, the simulated response to a negative load step (Figure 4.2) was less promising.

The measurements indicate a higher nonlinearity than is included in the model. Sources of the nonlinearity may be in the engine and/or the fuel system. Jeffries [33] noted

Table 4.1 Governor Parameters								
Diesel	τ_{ac}	K_g	τ_{Z1}	τ_{Z2}	τ_{P1}	τ_{P2}	K_{dr}	τ_{dr}
A	0.075	4.75	0.35	0.55	0.005	0.022	0.04	1.4
A&B	0.075	18.2	0.33	0.05	0.013	0.010	0.04	1.4

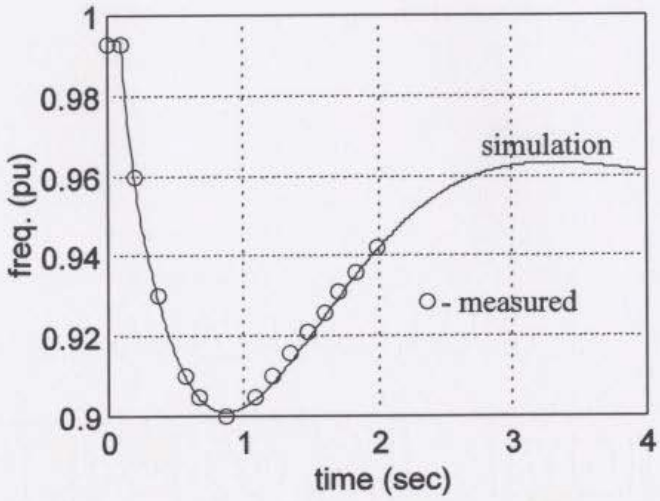

Figure 4.1 Speed of Diesel A for a +0.64 pu load step.

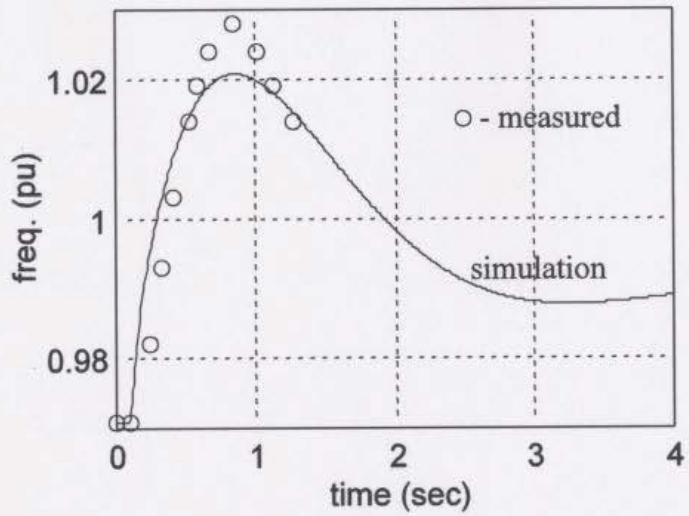

Figure 4.2 Speed of Diesel A for a -0.32 pu load step.

similar discrepancies, which he attributed to a nonlinear relationship between the fuel rack position and the actual amount of fuel injected

Assuming the diesel generators are identical, are tuned similarly, and share the load equally, the two diesel generators can be approximated by one diesel generator of twice the capacity. This is reflected in the model by using the same per unit parameter values, but twice the volt-ampere base.

Referring to Figures 4.3 and 4.4, it can be seen that the governor parameters found for Diesel A (curve *A*) do not match the performance measured for both diesels (A&B). The most likely explanation for this is that Diesel B is tuned much differently than Diesel A. New governor parameters were estimated for Diesels A&B, and are listed in Table 4.1. Using the A&B governor parameters, the simulated and measured response to a positive load step of +10 kW (0.08 pu - 2*SG base) match fairly well (Figure 4.3, curve: *A&B*), but again, for a negative load step of 40 kW (0.32 pu - 2*SG base), the match is poorer (Figure 4.4, curve:

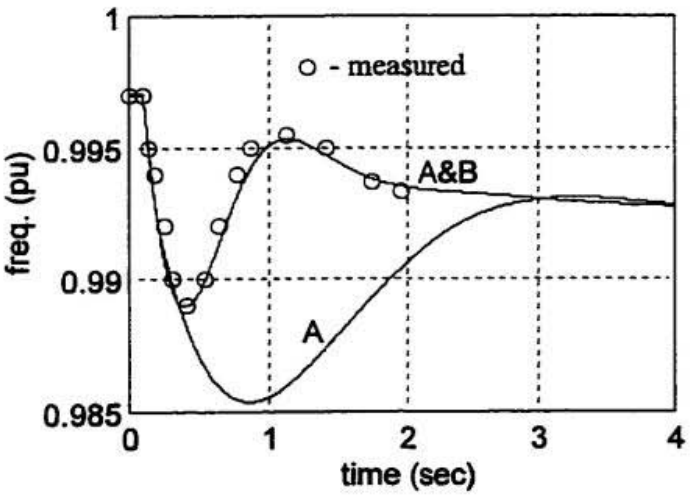

Figure 4.3 Diesels A&B speed for a +0.08 pu load step.

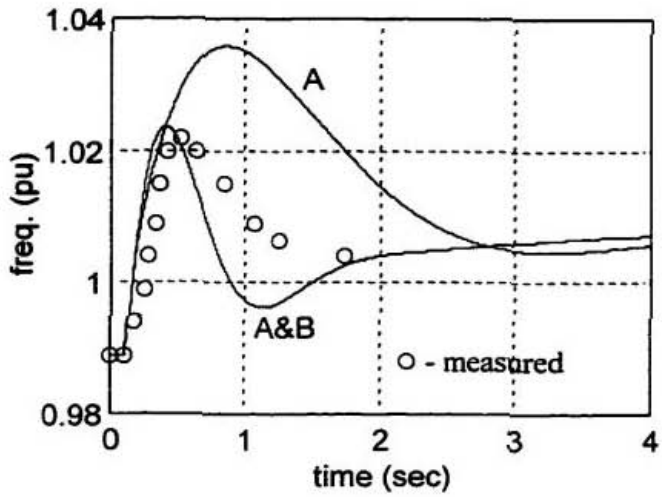

Figure 4.4 Diesels A&B speed for a -0.32 pu load step.

A&B).

The governor parameters for Diesels A&B were chosen for use with the design and analysis of the dump load controller (Chapter 5), since they represent a faster response than the Diesel A governor parameters. During parallel operation of the dump load and the diesel generator(s), the fast acting dump load controller will dominate. Therefore the dump load controller is more likely to have instability with a fast acting governor than a slow acting governor. In addition, the A&B governor parameters were assumed to better represent a typically tuned diesel generator, since they are nearly the same as the parameters given by Kamwa [36] for a Woodward EA1700 electronic governor.

4.2 Wind Turbine Mechanical Model Validation

Characterizing the dynamics of a wind turbine is a difficult task. Their large size

prevents the user from performing experiments in a controlled environment, such as a wind tunnel. Accurately measuring the instantaneous wind speed through the entire swept area of the turbine is also a large undertaking. Most aerodynamic models of wind turbines found during the literature review were quasi-steady models based on the turbine's published or statistically measured power curve. Øye [51] characterized unsteady aerodynamics by applying a step change in the blade pitch to determine the induction lag of the turbine. Wilkie, Leithead and Anderson [49] verified their wind turbine model, which included induction lag, by comparing measured and simulated power spectra. A spatial filter was used to estimate the effective windspeed from the measured point windspeed.

The steady-state performance of the AOC 15/50 wind turbine model matches the manufacturer's published power curve (Figure 3.8), since the model uses a look-up table derived from this curve. At the time of writing, there have been no measurements found which can be used to validate the dynamic performance of the wind turbine model presented here. The drive train parameters were obtained from Jeffries [33], but there were also no measurements available to verify this portion of the model.

4.3 Electrical Model Validation

Full-order electric machine models are seldom employed in wind-diesel studies. Instead various reduced-order models are utilized, thus omitting certain aspects of the machine's behaviour. In this section the performance of the full-order electrical model is validated. The performance of the reduced-order generator models are weighed against the

performance of the full-order generator models, and the effects of neglecting the stator speed terms and magnetic saturation are evaluated.

For the simulations in this chapter, the electrical network has been represented by the one-bus impedance model when using the full-order electric machine models, and the three-bus admittance model when using the reduced-order electric machine models.

4.3.1 Synchronous Generator Models

4.3.1.1 Load Step Change Response - Theoretical Validation

Two of the extremes that a diesel generator in a HPNSWD system would encounter during normal operation are the disconnection of the wind turbine (WT) while the turbine is at zero and full output power. This represents the low wind cut-out and the high wind shut-down of the wind turbine, respectively. Wind turbine connection (cut-in) was not included here, since a soft-start device has been installed on the turbine to limit inrush current. A third scenario has been included which represents the low wind cut-out of the wind turbine with a 30 kVAR capacitor bank connected to the turbine. This case is included because capacitor banks are often used with wind turbines. This scenario presents a case where the SG is underexcited instead of overexcited, which rounds out the SG testing . Note that the wind turbine and capacitor bank are disconnected at the same instant. The three cases of system loading immediately before the wind turbine disconnection are listed in Table 4.2.

In order to segregate the synchronous generator responses, the field voltage (E_{fd}) and rotor speed (ω_r) are held constant. The dump load is also held constant for the duration of

Table 4.2 Initial System Loading								
Case		SG		Wind Turbine		Village Load		Dump Load
#	U_w (m/s)	P (kW)	Q (kVAr)	P (kW)	Q (kVAr)	P (kW)	Q (kVAr)	P (kW)
1	25	9.9	30.6	58.1	-30.6	31.2	0	36.8
2	0	34.0	24.4	-2.7	-24.4	31.2	0	0
3	0	34.0	-5.6	-2.7	5.6	31.2	0	0

the simulation, since the dump load controller will not react instantaneously. The response to a high wind WT shut-down (Case #1) is shown in Figure 4.5. This simulation compares the response of the full-order (5th-order) SG model with the 3rd, 2nd and 1st-order reduced SG models. Magnetic saturation is neglected in this first simulation.

The large negative voltage spike (0.52 pu magnitude) of the full-order model response

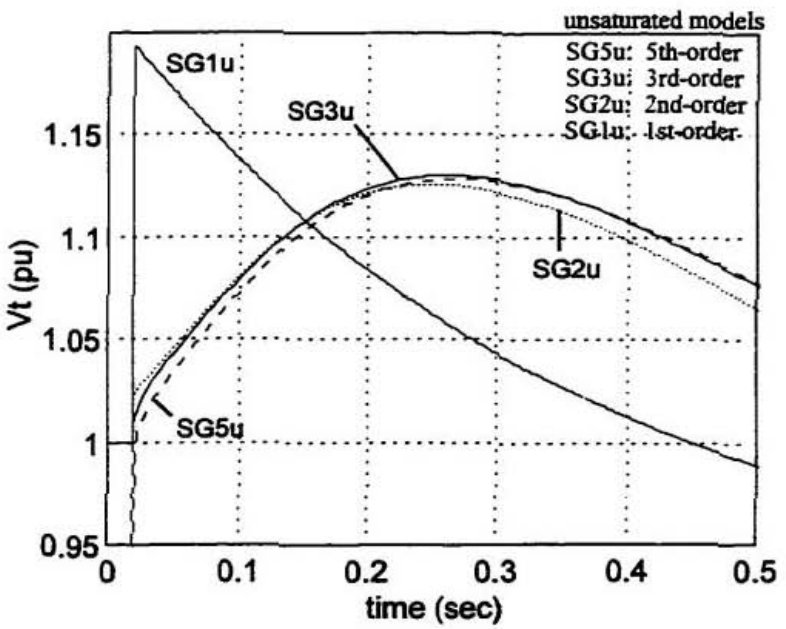

Figure 4.5 SG voltage response to WT disconnect, Case #1.

is the result of the switching transient of the SG stator when all three phases of the induction generator (IG) are disconnected simultaneously. In the actual system the IG is connected to the grid by a zero-crossing relay (ZCR) in each phase. The ZCR's operate independent of one another, and will only open when their respective phase current crosses zero.

To investigate the effects of the ZCR's on the simulation, the Case #1 WT disconnection was simulated on a per phase basis, using the ZCR's and the full-order synchronous and induction generator models. The simulation is somewhat more complex, and can be found in Appendix D. The results of the simulation with the ZCR's included are illustrated in Figure 4.6. In the simulation there are two voltage spikes since phase *a* disconnects at $t = 20$ ms, and both phases *b* and *c* disconnect 4 ms later. The last two phases will always disconnect simultaneously since the IG has a *three wire connection* (i.e., no ground return). With one phase open, the remaining two phase currents must be equal but opposite.

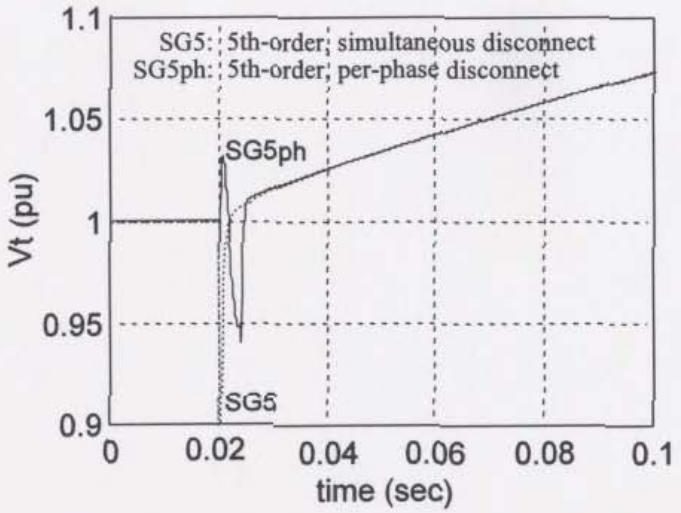

Figure 4.6 WT disconnect with ZCR's, Case #1.

From Figure 4.6, the magnitude of the switching transient is reduced to 0.05 pu, but with virtually no change to the SG response outside of the switching interval. These switching transients are quite fast and subject to the generator and system high frequency responses which have not been considered.

Returning to the comparisons of the reduced-order SG models in Figure 4.5, it can be noted that neglecting the stator transients, as in the 3rd order model, allows the stator current and the resultant terminal voltage (V_t), to increase instantaneously. Further, neglecting the *d*-axis damper winding, as in the 2nd-order model, allows a slightly larger instantaneous stator current increase. After one 60 Hz cycle (17ms) the terminal voltages of the 2nd and 3rd-order models are nearly equal, but approximately 0.01 pu higher than the full-order model. The response of the excitation system must be considered before any conclusions can be made about the dissimilarities in these responses past this point.

The 1st-order model, on the other hand, gives a completely different voltage response. This is because the *q*-axis damper winding has a large damping action which is neglected in the 1st-order model.

The electromagnetic torque transient due to the Case #1 WT disconnection (Figure 4.7) is nearly the same for the full, 3rd and 2nd-order models, but, again, the 1st-order model gives very different results.

These results show that the use of a 1st-order model to simulate a synchronous generator could lead to erroneous results in modelling the dynamics of both system frequency and voltage.

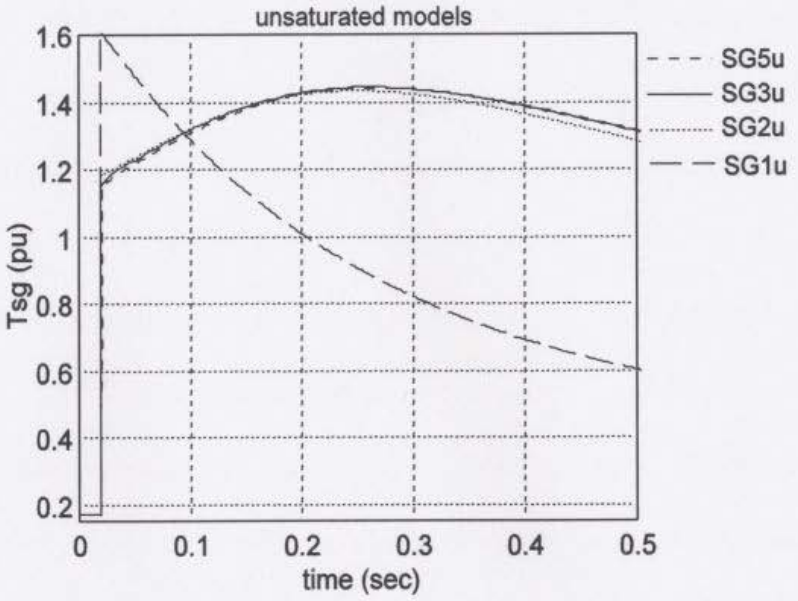

Figure 4.7 SG torque for WT disconnect, Case #1.

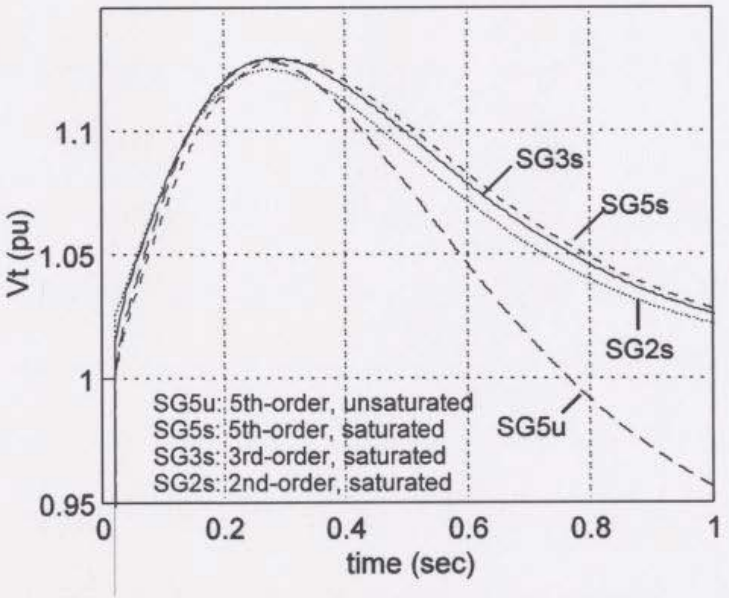

Figure 4.8 Effect of saturation on SG transients, Case #1

The effect of magnetic saturation on the SG models is illustrated in Figure 4.8. The high wind WT shut-down (Case #1) is repeated with magnetic saturation included in the models. The field voltage and the rotor speed are held constant. The initial response remains virtually unchanged, but the response tends towards a higher steady state. The higher steady state is the result of increased magnetic flux, for a constant field voltage, as the generator becomes less saturated. Saturation has only a slight influence during the generator's subtransient and transient periods. This is due to the fact that: the subtransient and transient reactances are the parallel combination of the magnetizing inductance and the rotor leakage reactances (Equations 4.1 and 4.2); only the *d*-axis magnetizing inductance, $X_{md.sg}$, saturates; and $X_{md.sg}$ is an order of magnitude larger than the leakage reactances.

$$X''_{d.sg} = X_{ls.sg} + (X_{md.sg} \| X_{lfd.sg} \| X_{lkd.sg}) \tag{4.1}$$

$$X'_{d.sg} = X_{ls.sg} + (X_{md.sg} \| X_{lfd.sg}) \tag{4.2}$$

Thus, saturation of $X_{md.sg}$ has only a small effect on the generator impedance during the subtransient and transient periods.

The SG terminal voltage response due a low wind WT cut-out, without a capacitor bank (Case #2) and with a capacitor bank connected to the WT (Case #3), are presented in Figures 4.9 and 4.10, respectively. In these simulations, saturation is included in the models, and the field voltage and rotor speed are held constant. The full-order, and 3rd and 2nd-order reduced SG models continue to give similar results. Also, since the *q*-axis damper winding action is much smaller in these cases, the 1st-order SG model gives results more consistent with the other models.

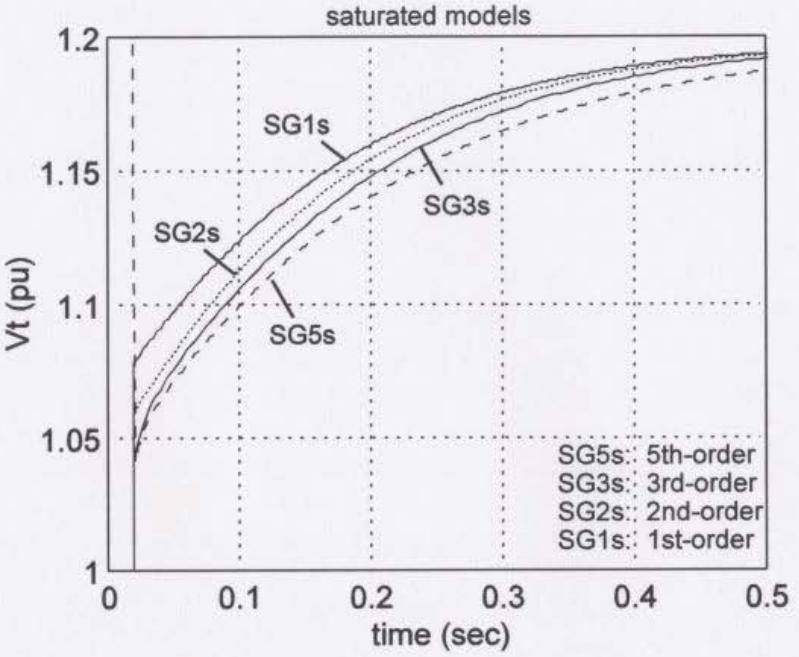

Figure 4.9 SG voltage response to WT disconnect, Case #2.

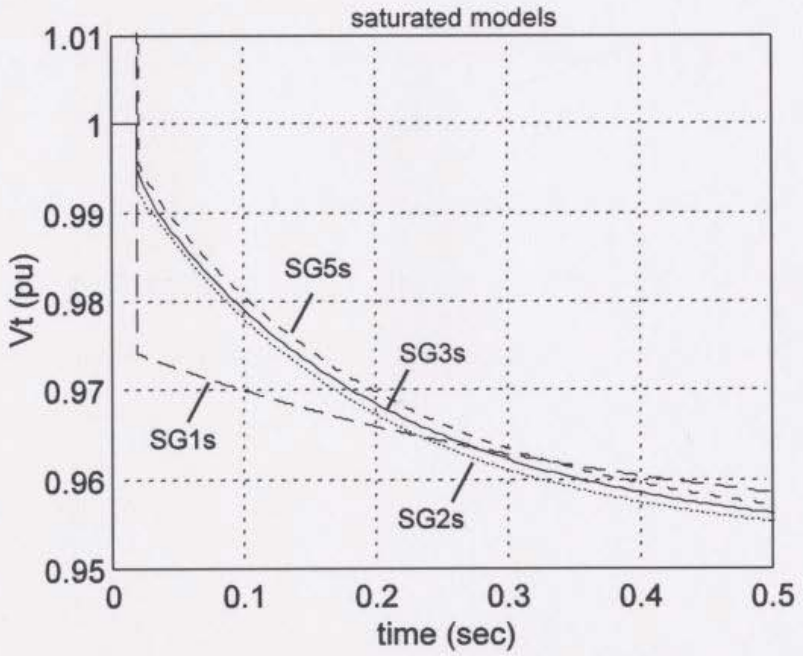

Figure 4.10 SG voltage response to WT disconnect, Case #3.

Dynamic models of synchronous generators are comprised of many interacting functions. To confirm that no errors were made while defining the synchronous generator models in SIMULINK, analogous simulations were run in SIMULINK and the Extended Transient-Midterm Stability Program (ETMSP)[6] [64]. The synchronous generator was subjected to a load step from 0.4+j0.3 pu to 0.96+j0.0 pu (SG base), under a condition of constant field voltage, and with saturation neglected. The terminal voltage and field current of the 3rd-order SIMULINK model (Figure 4.12) matched the corresponding ETMSP results exactly (Figure 4.11, curves: *2-ax. subtr.*).

Note that in ETMSP the field current is given in the exciter base - which has a conversion factor of X_{mdu}, where X_{mdu} is the unsaturated value of X_{md}. ETMSP is capable of simulating up to 3 rotor circuits in each axis, but stator transients and speed terms are neglected from the stator voltage equations. For the ETMSP 2-axis, subtransient (*2-ax. subtr.*) simulation, all the SG parameters were entered into ETMSP, i.e., one q-axis and two d-axis circuits. Thus, these ETMSP simulations are equivalent to the 3rd-order model defined in this study.

A model with only one rotor circuit was also implemented in ETMSP by neglecting the subtransient parameters. This one-rotor-circuit ETMSP model (Figure 4.11, curve: *1-axis model*) corroborated the performance of the 1st-order SG model (Figure 4.13) in SIMULINK.

---

[6] ETMSP is a commercial power system transient stability program developed for the Electric Power Research Institute (EPRI).

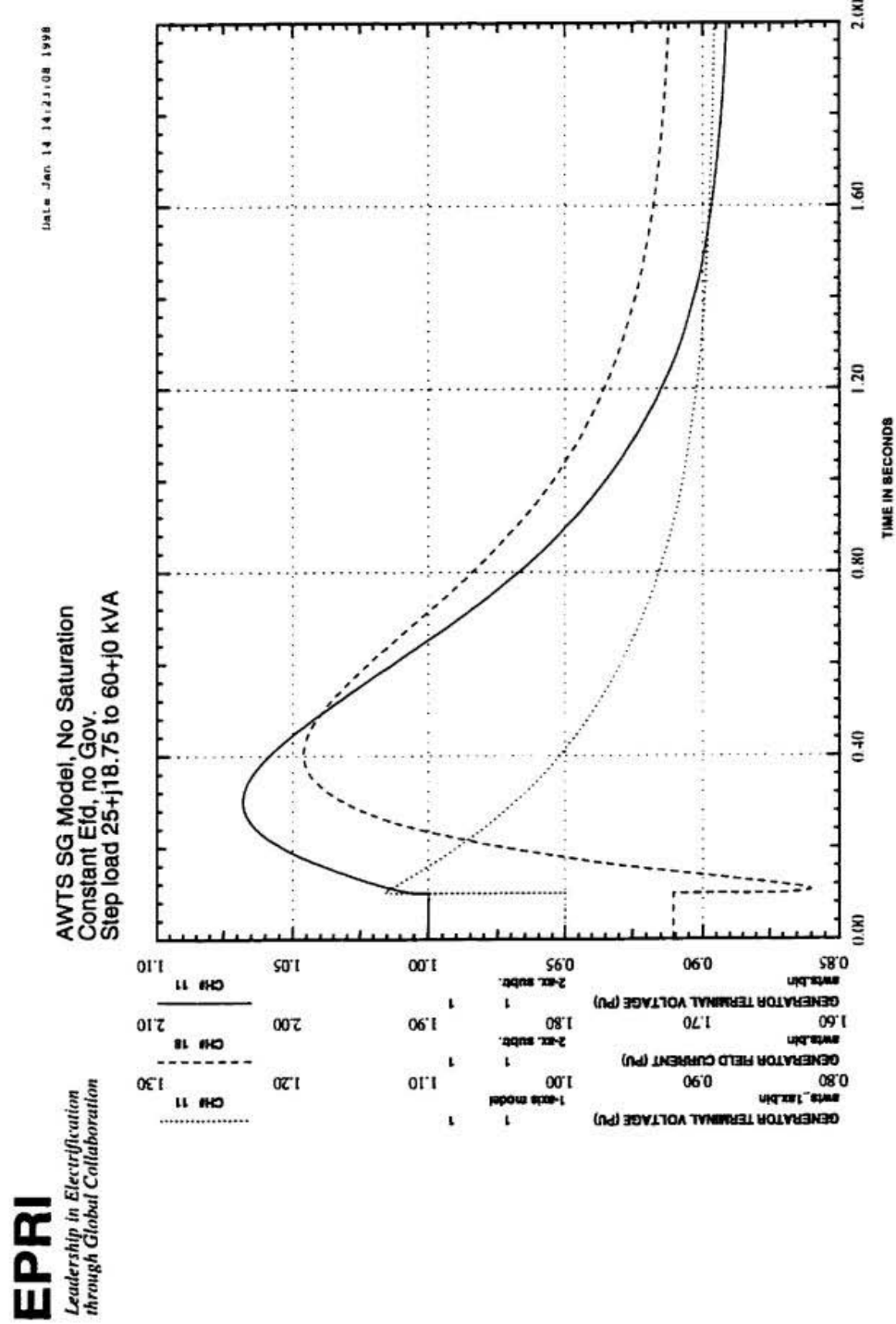

Figure 4.11 ETMSP 3rd & 1st-order unsaturated response to a 0.4+j0.3 pu to 0.96+j0.0 pu load step.

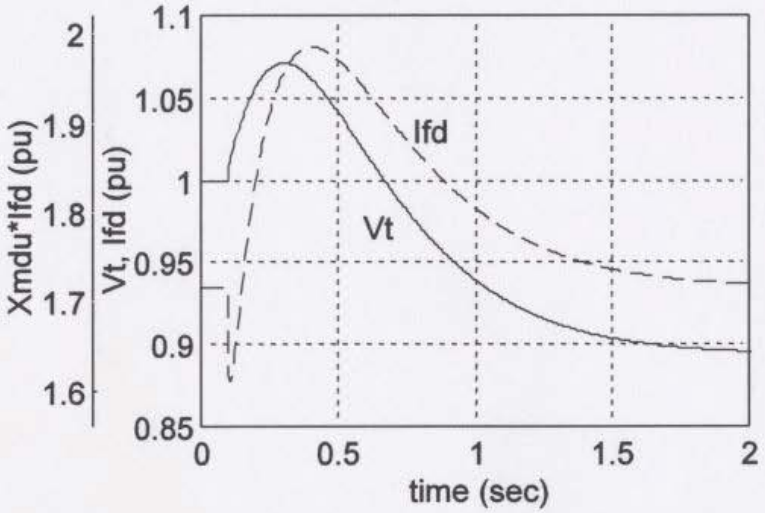

Figure 4.12 SG 3rd-order unsaturated, load: (.4+j.3)→(.96) pu.

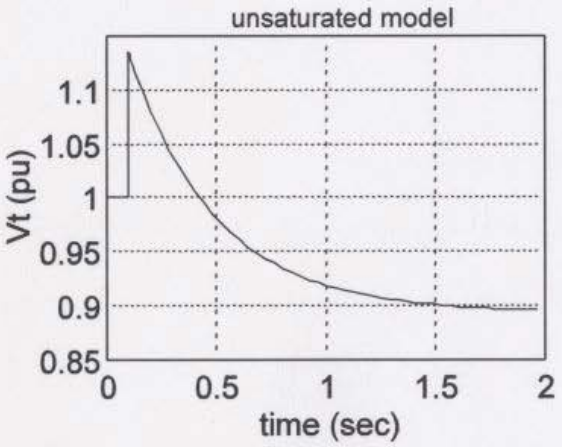

Figure 4.13 1st-order SG, load: (.4+j.3)→(.96) pu.

Saturation was then introduced into the models. Comparison of Figures 4.14 and 4.15 shows a discrepancy between the 3rd-order SIMULINK and ETMSP models when *d*-axis saturation is included. Solving for the steady-state conditions, where,

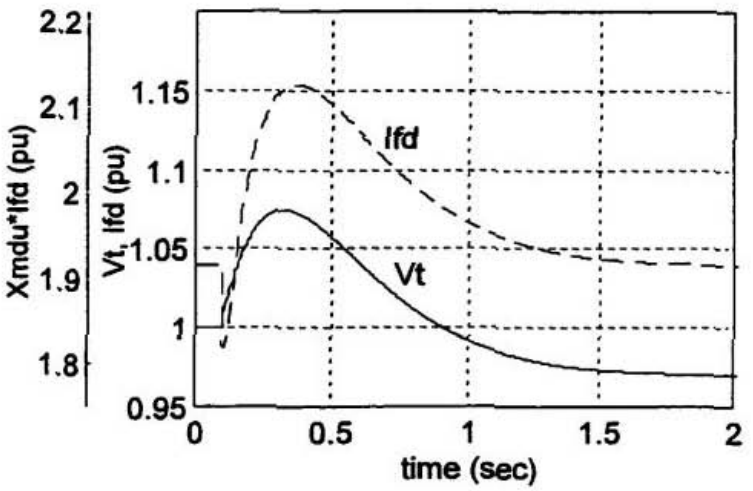

Figure 4.14 SG 3rd-order, saturated, load: (.4+j.3) → (.96) pu.

$$X_{md} = \frac{X_{mdu}}{1 + S_G} \tag{4.3}$$

yields a steady-state field current, I_{fd}, of 1.91 pu (exciter base). This agrees with the SIMULINK model implemented here, but is slightly less than the 1.95 pu steady-state field current determined by ETMSP. In addition, the initial response of the ETMSP model changes significantly with the addition of the *d*-axis saturation (compare Figures 4.11 and 4.15). This contradicts the theory illustrated on page 98 of this thesis which states that saturation has only a slight influence on the generator response during the subtransient and transient periods.

Speculation about the cause of this discrepancy has led the author to conclude that the ETMSP program computes the saturation factor, S_G, from the magnitude of the total magnetizing flux linkage, ψ_m, where,

EPRI

Leadership in Electrification through Global Collaboration

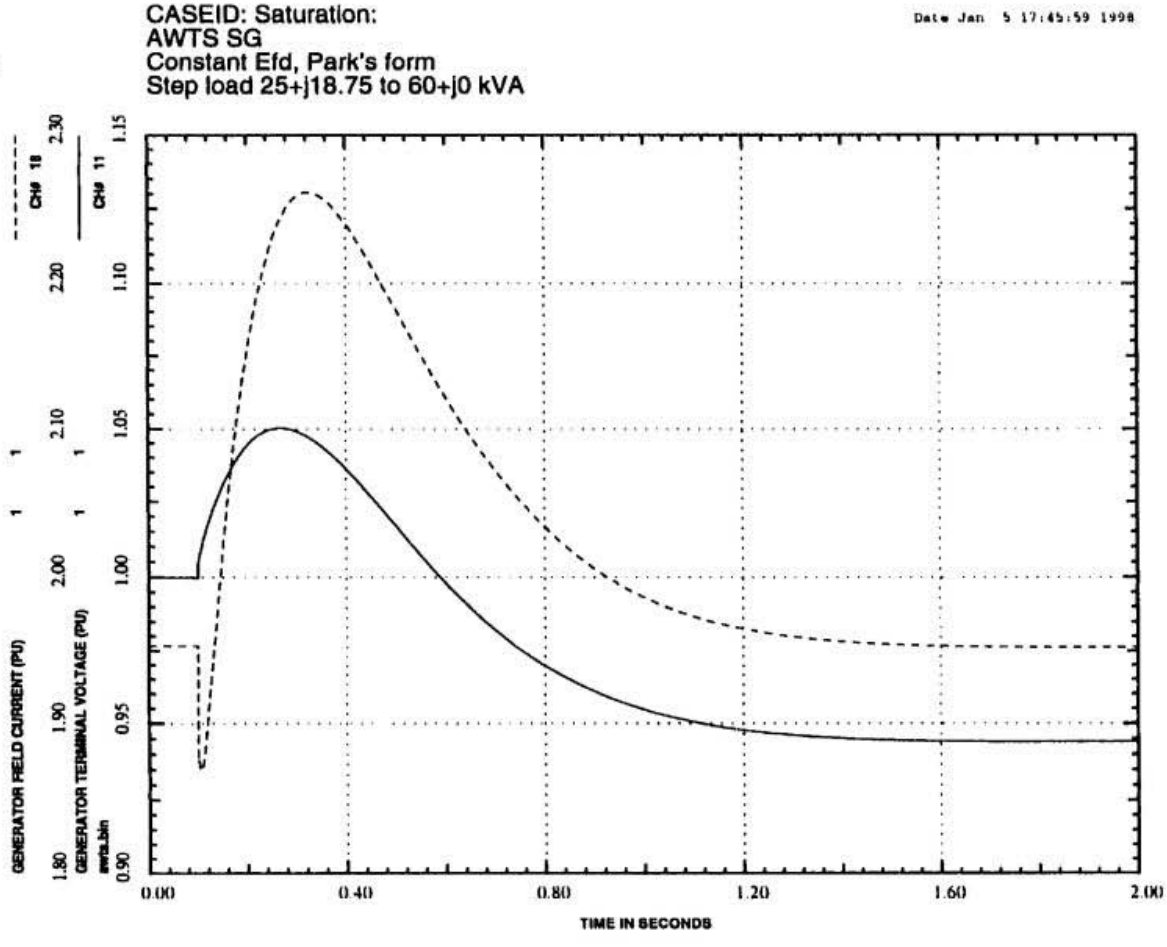

Figure 4.15 ETMSP 3rd-order saturated response to a (0.4+j0.3) → (0.96+j0.0) pu load step.

$$\psi_m = \sqrt{(\psi_{mq})^2 + (\psi_{md})^2} \tag{4.4}$$

instead of the *d*-axis magnetizing flux linkage, ψ_{md}, even though only *d*-axis saturation has been specified.

When modelling salient-pole machines, Krause [57], and Anderson and Fouad [59] regarded saturation to be solely in the *d* axis, with the saturation being a function of ψ_{md} only. Kundur [58], who was the project leader in the development of ETMSP, also stated that salient-pole machines saturate solely in the *d*-axis, but he gave no indication that saturation should therefore be determined by ψ_{md}, instead of ψ_m, in this case. The author is not certain whether this indicates a difference in theory, or whether Kundur implicitly meant that ψ_{md} should therefore be used. Logically, for a salient rotor, only the *d* component of the magnetizing flux should contribute to saturation, since the *q* component of the magnetizing flux should see no saturation in its path. Thus, saturation is assumed to be solely a function of ψ_{md} in this study.

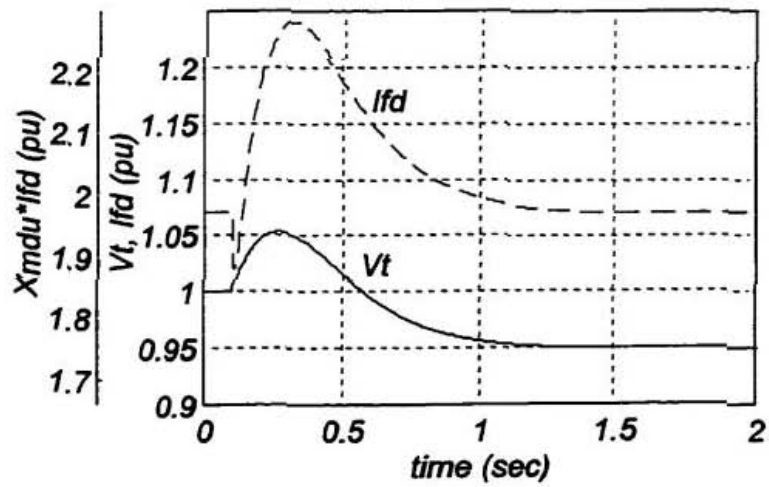

Figure 4.16 SG 3rd-order, $S_G = f_{sat}(\psi_m)$.

To confirm the theory that the ETMSP model calculates saturation from ψ_m, even though only *d*-axis saturation is specified, the 3rd-order SIMULINK model was altered to calculate saturation as a function of ψ_m, but with saturation solely in the *d* axis. The response of this model (Figure 4.16) was very close to that of the ETMSP model (Figures 4.15).

4.3.1.2 Excitation System Validation

Three different sets of parameters were suggested by the manufacturer for modelling the AVR [62]. Having chosen the set of parameters that best matched the characterization measurements reported in Jean et al. [44], the results in Figure 4.17 were obtained, where, the results of the full-order SG model with and without saturation are included. The test was made by applying a 0.1 pu step increase to the AVR reference voltage, with the synchronous generator unloaded and rotor speed held constant. As would be expected, generator saturation added slightly more damping to the transient. Neither simulation gave near the amount of overshoot measured, even though the stabilizer gain, K_F, was set very low ($K_F = 0.005$) in

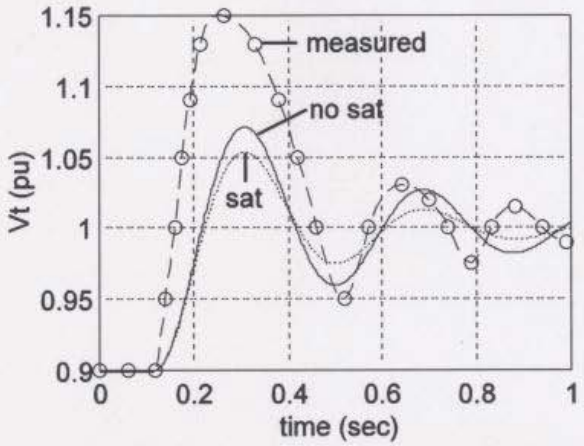

Figure 4.17 V_{ref} step, $K_F = 0.005$.

the simulations.

The measured results were highly nonlinear, with the terminal voltage waveform having a much faster attack than decay. The nonlinearity was more pronounced in the AVR's measured output current [44], which resembled a sawtooth waveform. The excitation system model does not replicate this nonlinearity. The sawtooth current waveform suggests that the source of the nonlinearity is the single-quadrant converter in the output of the AVR, which drives the exciter inductance. The converter could conceivably charge the inductance more quickly than the inductor would discharge into the exciter at light loads. With increased exciter loading the discharge time would decrease, thus decreasing the nonlinearity. Further tests are required to confirm this.

The complete diesel generator model, including the speed terms the in full-order SG model, was then verified against the resistive load step measurements reported by Saulnier et al. [39]. Figure 4.18 shows the voltage response to a resistive load step from 0.35 pu to 0.03 pu (SG base). A value of $K_F = 0.02$ was found to give the best fit. K_F is the stabilizer gain, which is the external operating adjustment of the AVR. This setting of K_F gives a more stable response than the setting used for the previous test (Figure 4.17). It is not known which diesel was used for the test in Figure 4.17, or if the AVR was adjusted during the time that passed between the two tests. A value of 0.02 is assumed to be the proper value for K_F, since it corresponds with the later measurements, and a better tuned voltage system.

The voltage response to a 0.05 to 0.64 pu (SG base) resistive load step are shown in Figure 4.19. The initial ringing of the simulation does not correlate well with the measurement, but the longer term match is better, and the magnitude of the transients are

comparable.

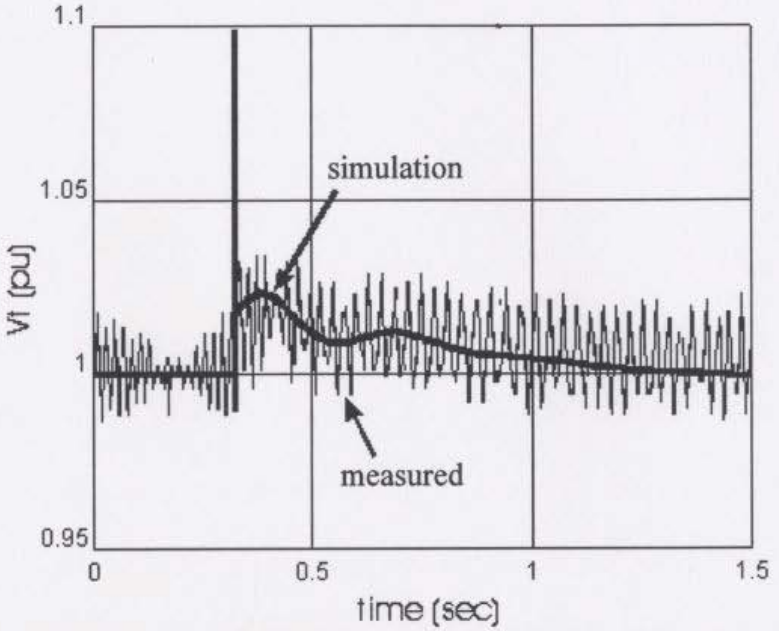

Figure 4.18 Voltage, Diesel A, load: 0.35 → 0.03 pu (K_F=0.02).

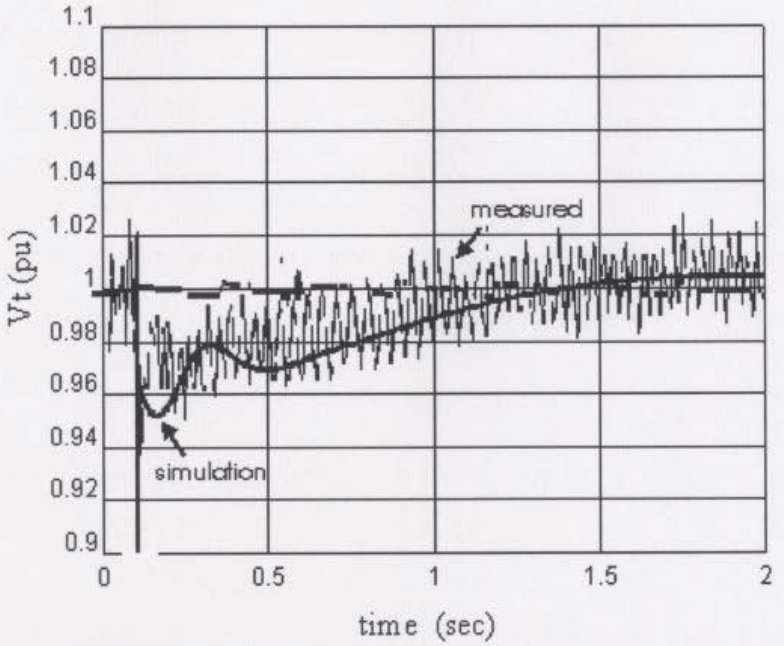

Figure 4.19 Voltage, Diesel A, load: 0.05 → 0.64 pu.

4.3.1.3 Electrical Effects of Rotor Speed on SG

The literature search revealed that most synchronous generator models used in wind-diesel modelling do not include the effects of rotor speed variation. This is a common simplification in power system studies, since the frequency variation is generally small in large power systems. In addition, the model is greatly simplified by neglecting the electrical transients of the stator voltage equations, which are fast, and are considered to have little effect on the stability of large power systems. In order to properly neglect the voltage transients of the stator voltage equations, both Krause [57] and Kundur [58] determined that the speed terms in the stator voltage equations must also be neglected by replacing ω_r with ω_0 in the stator voltage equations (3.21) and (3.22). Thus, the stator speed terms are neglected in the reduced-order electric machine models.

In wind-diesel systems, frequency variation is potentially much greater than in large power systems. Whether the effects of frequency variation on the system voltage in wind-diesel systems can be safely neglected has not been addressed in any of the literature uncovered by the literature search.

Jean et al. [44] applied a rotor speed transient to the open circuited synchronous generator while holding the input voltage to the brushless exciter constant. Similar results were obtained from the full-order SG model (Figure 4.20), by re-creating the speed transient, and approximating the exciter response by making the effective field voltage, $E_{fd.ef}$, proportional to the rotor speed. Thus,

$$E_{fd.ef} = \omega_r E_{fd} \tag{4.5}$$

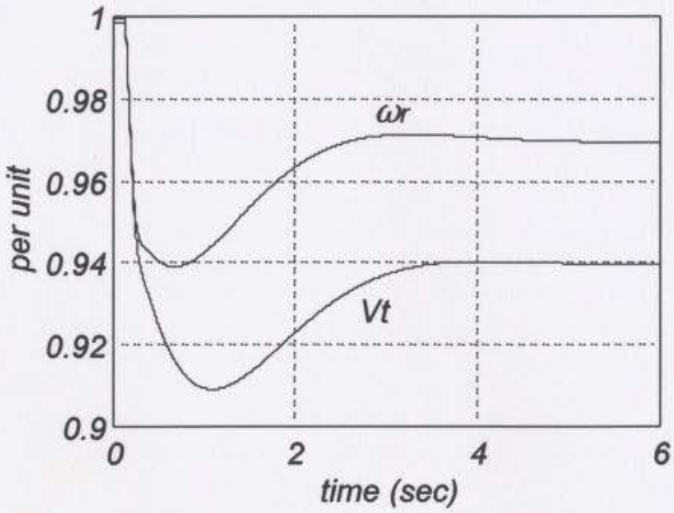

Figure 4.20 SG + exciter open circuit voltage, constant V_R.

The brushless exciter is essentially a synchronous generator, and (4.5) is an approximation of the exciter's response to speed changes. Jeffries [33] accounted for rotor speed effects in his electrical model by including a field voltage proportional to rotor speed. All other wind-diesel dynamic models found in the literature search neglected rotor speed from the electrical models.

Since the stator currents are zero, the synchronous generator's open circuit voltage, with a constant E_{fd}, is directly proportional to the rotor speed (Figure 4.21). The relationship becomes more complex when the SG is loaded, as demonstrated in Figure 4.21 for overexcited (Cases #2) and underexcited (Case #3) conditions.

The result of neglecting the speed terms for a large speed transient (+0.64 pu load step, Diesel A parameters) is illustrated in Figure 4.22, where the curves are labelled $Vt(\omega_r)$ and $Vt(w/o\ \omega_r)$ to indicate the response of the model with and without the speed terms, respectively. The AVR has been included in this simulation, and the results can be compared

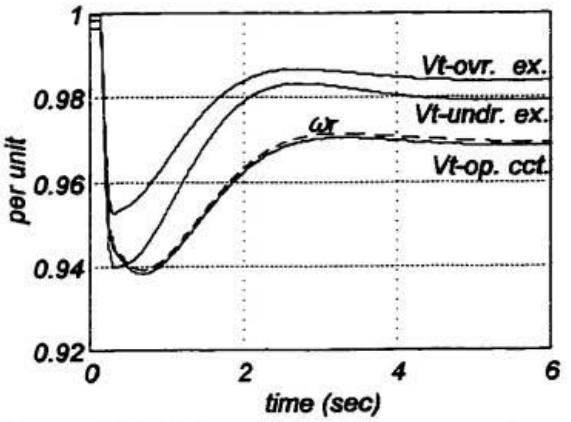

Figure 4.21 SG response to rotor speed variation.

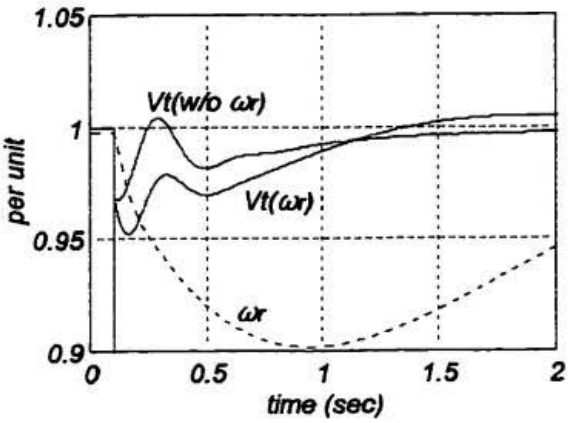

Figure 4.22 SG voltage, w/ & w/o speed terms.

with the actual system measurements in Figure 4.19. These results demonstrate that for this size speed transient (10%) the voltage transient is nearly doubled by incorporating the effects of rotor speed on the synchronous generator and exciter.

Including a field voltage which is proportional to rotor speed, while neglecting the stator speed terms in the SG model (Figure 4.23, curve: *SG3s: Efd*ω_r*), provides a slight improvement over the no speed-term case (Figure 4.23, curve: *SG3s: Efd)* . With the effects

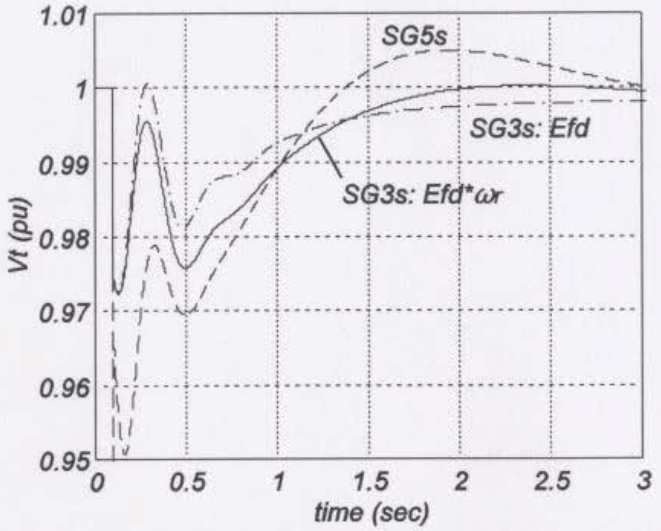

Figure 4.23 SG response to speed proportional field.

of rotor speed only included in the exciter, the response to the speed transient is slow due to the large generator field time constant. The response of the full-order model with speed terms (Figure 4.23, curve: *SG5s*) is also included for comparison.

4.3.1.4 Voltage Control System Performance

The excitation system and the synchronous generator make up the closed loop, voltage control system. The addition of the AVR to the synchronous generator creates a high gain feedback loop, thus reducing the effects of magnetic saturation and rotor speed.

Magnetic saturation of the synchronous generator is often neglected in wind-diesel models, but it is often included in power system stability studies. Since saturation has little impact on the initial, fast transients, it's principal effect will be on the slower voltage control loop. Figure 4.24 illustrates this for a high wind WT shut-down (Case #1), where the primary effect of saturation is increased damping. This is confirmed by the Bode plots (Figure 4.25)

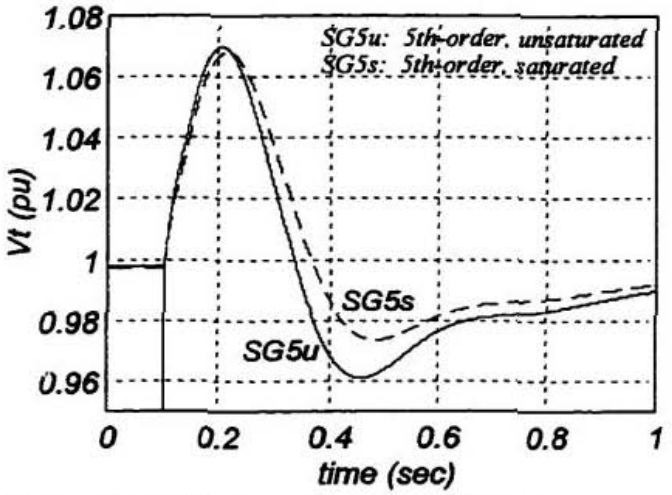

Figure 4.24 SG + exciter voltage, WT disconnect, Case #1.

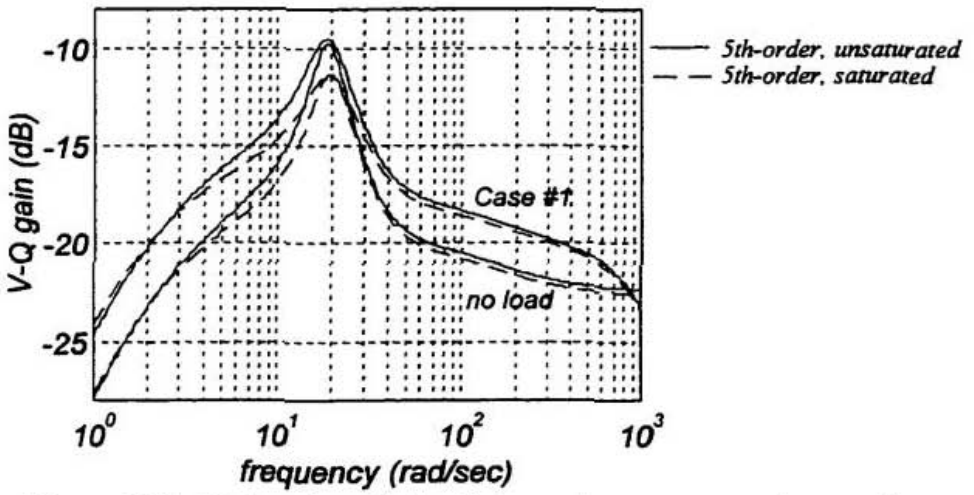

Figure 4.25 SG + exciter Bode plot, reactive power to voltage gain.

of the sensitivity of the terminal voltage to changes in reactive load. The Bode plots were determined by linearizing[7] the voltage control system at no-load, and Case #1 loading. Including saturation in the generator model reduces the gain of the resonance frequency at

[7] Models were linearized using the *linmod* function in SIMULINK [18].

3 Hz by approximately 3 dB, but has little impact at higher and lower frequencies.

Magnetic saturation largely affects the synchronous generator rotor angle, which is the primary focus of power system stability analysis. Hence saturation's importance in multiple, synchronous machine, power system stability studies. For a single synchronous generator wind-diesel system, rotor angle is not normally a concern.

The analyses in this study indicate that magnetic saturation can be neglected from the synchronous generator model without causing larger errors than those due to parameter uncertainties and other approximations in the model. Conversely, including generator saturation does not increase model complexity and simulation times substantially (solution times were not noticeably changed by saturation in this study), therefore there is little reason to neglect it.

The effects of rotor speed transients on the terminal voltage have already been identified in the previous section. Figure 4.26 illustrates the voltage control system response

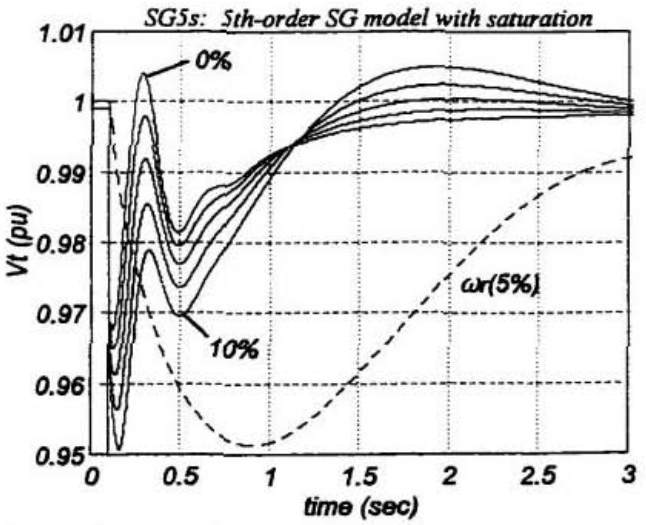

Figure 4.26 Voltage response: increasing ω_r transients.

to a 0.64 pu load step on the SG, where the magnitude of the speed transient is varied from 0% to 10%, in 2.5% increments (the 5% speed transient is included in the figure for reference). The results of Figure 4.26 indicate that for a sudden change in load, the magnitude of the voltage transient is increased by approximately one tenth of the magnitude of the speed transient. Unfortunately it would be imprudent to generalize from this observation. The relationship between the rotor speed and the terminal voltage is not simple. Both the magnitude and the shape of the rotor speed transient have an effect on the terminal voltage, with the generator load also being a factor. Due to this complex relationship, it is difficult to identify a point below which speed transients can be neglected or above which, they should be included.

On the one hand, neglecting the effects of rotor speed on the voltage produces more optimistic results, while, on the other hand, including speed transients significantly increases the complexity of the simulations. As a trade-off, a rule of thumb applied in this study is: if the simulations neglecting speed transients result in marginal voltage performance, and a significant speed transient (greater than 0.02 pu) coincides with the large voltage transient, then the simulation is repeated using the full-order models, in which the effects of speed transients are included.

4.3.1.5 Synchronous Generator Parameters

The reliability of quoted synchronous generator parameters must be considered, especially for small generators. Some studies have determined significant differences between the manufacturer's quoted parameters and those measured during the studies

[42,29]. Tindall et al. [65] have identified some problems with the reliability and utility of normally quoted parameters for small machines (20 kVA to 2 MVA), and, in particular, with the reliability of parameters determined by standard tests on small brushless salient-pole machines. One of the problems stated is: manufacturers seldom indicate if the quoted parameters were calculated or measured, and if they were measured, what tests were implemented under what conditions. Another problem is the accuracy of standard tests, which are suited for larger machines, when applied to small machines.

For this study, the reliability of the quoted synchronous generator parameters is unknown. One oddity in the quoted data is in the saturated reactances. The data indicates that all the reactances, except the stator leakage reactance, saturate by approximately 24%. The load conditions for this level of saturation are not indicated. How these saturated values were determined is also not indicated. Theory and common practice dictate that only the d-axis magnetizing inductance should saturate significantly in a salient-pole machine [59,57,58]. Even in cylindrical rotor machines, where the q-axis magnetizing inductance also saturates (usually to a different degree), the rotor leakage reactances do not saturate. The author has assumed that the saturated reactances were calculated instead of measured, and that they were calculated incorrectly.

All other quoted machine parameters appear to be within normal ranges, but the quoted data contains two parameters which could be interpreted as the q-axis subtransient time constant. Both a transient and a subtransient time constant are given for the q-axis, but, for a salient-pole machine, a q-axis transient time constant is not applicable [59,58]. A survey of salient-pole generator data indicates that typical values for τ''_{q0} range from one quarter to

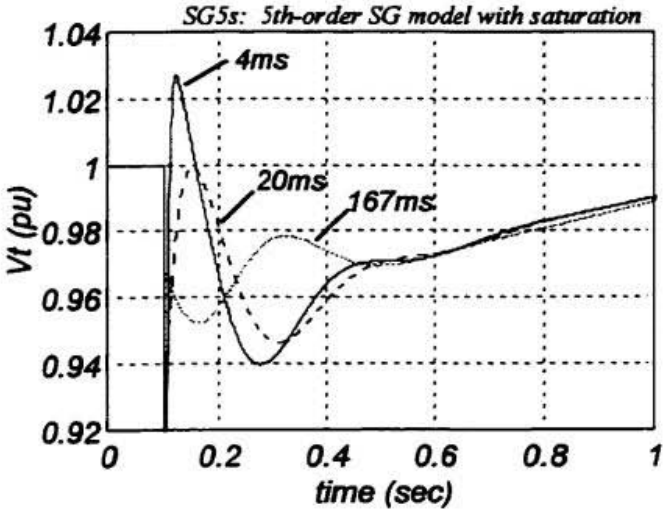

Figure 4.27 Voltage, Diesel A +0.64pu load step.

six times the value of τ''_{d0}. The applicability of this range to a small generator is unknown, since most of the data is based on large machines (e.g. 10 to 250 MVA [59,58], 1.2 to 3.1 MVA [42,46,66], and 388 kVA [67]). However, the limited data collected indicates that the τ''_{q0} of smaller machines tend to be near the upper end of the range.

Originally, the quoted τ''_{q0} of 4 ms was used since it is near the value of 8 ms given for τ''_{d0}. The limited effectiveness of the q-axis damper winding, corresponding to this very small time constant, results in a large positive voltage peak for a positive load step simulation (Figure 4.27, curve: *4ms*). This does not correspond well with the actual system, since there was no positive peak observed in the characterization measurements (Figure 4.19).

Using the quoted q-axis transient time constant of 167 ms for the model's τ''_{q0} gave simulation results more in line with the actual measurements (Figures 4.18 and 4.19). Stavrakakis et al. [34] and Kariniotakis et al. [35] appear also to have used the quoted q-axis transient time constant for τ''_{q0} in their models. The value of τ''_{q0} = 167 ms has been used in the simulations up to this point.

A q-axis subtransient time constant of 167 ms is well outside the expected range of 2 to 48 ms, assuming τ''_{d0} is approximately 8 ms. Estimating τ''_{q0} from the voltage transients of the measured load step responses in Figures 4.18 and 4.19, resulted in a value of 35 ms. Considering this τ''_{q0} value gives slightly more accurate results (Figures 4.28 and 4.29 versus Figures 4.18 and 4.19), and is within the expected range, it is assumed to be the correct value. It is difficult to determine whether the differences remaining between the measured and simulated responses are due to inaccuracies in the generator model or the excitation system model.

In the simulations for frequency and voltage control in Chapter 5 of this thesis, the adjusted value of 35 ms for the q-axis subtransient time constant, τ''_{q0}, has been used.

The comparative responses of the voltage control system with full-order, and reduced-order synchronous generator models using the adjusted SG parameters are shown in Figure 4.30. All rotor speed terms have been neglected for the purpose of direct comparison. The responses of the 3rd and 2nd-order SG models are nearly the same, but slightly less than the response of the full-order SG model. The larger transient of the full-order SG model is due to the added response of the stator to the fast load transient.

When applied to this synchronous generator, the commonly used 1st-order SG model gives erroneous, and nearly opposite, responses to fast load transients. For slow transients the 1st-order model may give satisfactory results, but care must be taken when dealing with fast transients. Unless very long time intervals are to be simulated, a 2nd-order SG model gives vastly improved results for the cost of only one additional differential equation, and a

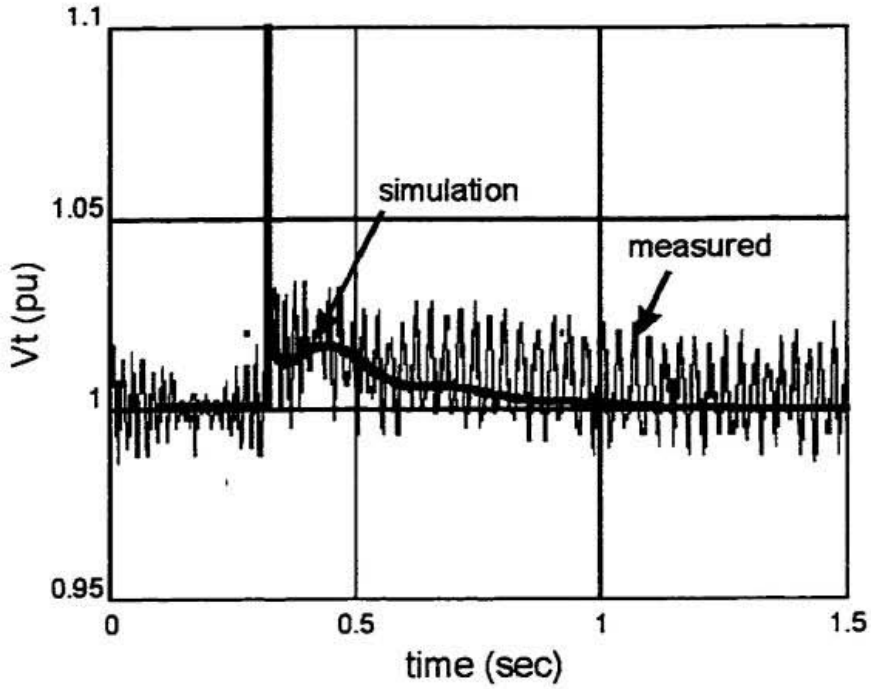

Figure 4.28 Voltage, Diesel A, load: 0.35 → 0.03pu, τ'_{q0} = 35ms.

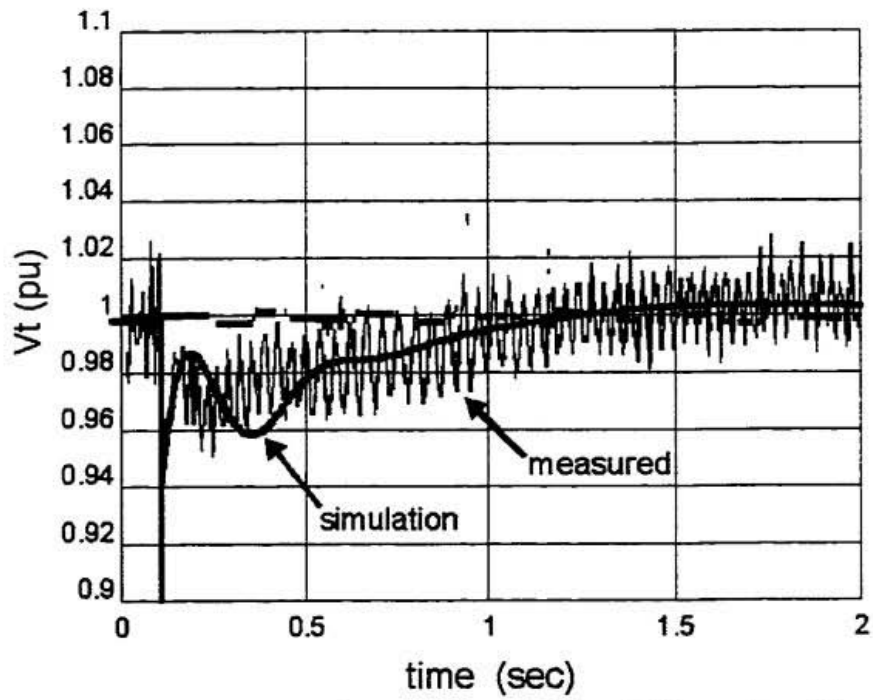

Figure 4.29 Voltage, Diesel A, load 0.05 → 0.64pu, τ'_{q0} = 35ms.

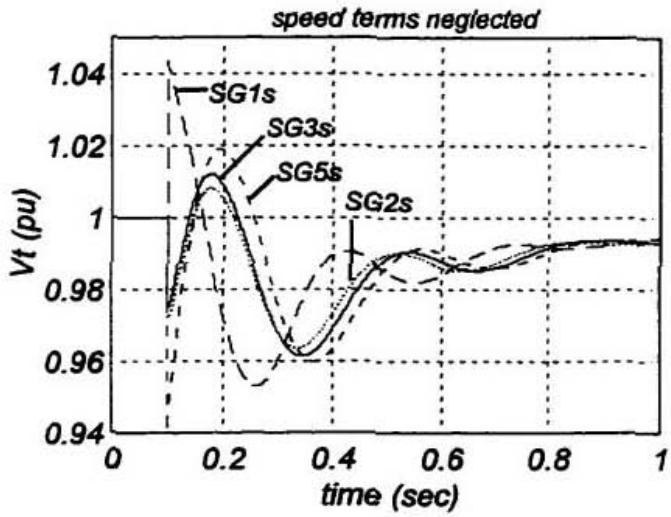

Figure 4.30 SG + exciter, τ''_{q0} = 35ms, +0.64pu load.

slightly smaller time step. For these reasons, the author suggests that a minimum of two orders be used to represent the synchronous generator in wind-diesel dynamic models.

The synchronous generator model validation has relied on the measurements of only two resistive load steps. Further tests are required to determine if the synchronous generator is accurately modelled over a broad range of active and reactive loads.

In practice, under the conditions of minimal rotor speed variation, the inaccuracies attributable to the reduction of the SG model to a 3rd or 2nd-order system are likely less than the inaccuracies due to imprecise model parameters. Anderson and Fouad [59] refer to a study on synchronous machine modelling in stability studies [68] that concluded it is more important to use accurate machine data than to use more elaborate machine models.

Considering that there remains some uncertainty in the model's parameters, the principal use of the full-order model is to determine the effects of rotor speed transients on the system voltage.

4.3.2 Induction Generator Models

The only parameters obtained for the induction generator (IG) used in the AOC 15/50 wind turbine, were the standard equivalent circuit parameters provided by the manufacturer [69]. No measurements were obtained to verify the correct operation of the induction generator models, therefore only the theoretical operation of the induction generator models can be verified.

From the literature search, validation of induction generator models used in wind-diesel dynamic models is seldom carried out. Where induction generator models are validated, the validation is limited to steady-state measurements of reactive versus active power [29], or active power versus slip [34]. To confirm that the IG models implemented in this study functioned properly in the steady state, the active versus reactive power (P-Q) characteristics were determined using the IG parameters presented by Uhlen et al. [29]. The P-Q characteristics using Uhlen's parameters were found to be the same as the P-Q characteristics of Uhlen's validated model [29].

The value of the IG's magnetizing inductance, X_M, quoted by the manufacturer is assumed to be the saturated value at nominal voltage and no load. This would be the case if its value was determined by the no-load test [57], which is a common practice. The amount of saturation, at nominal voltage, varies little over the power range, as illustrated in Figure 4.31. The solid curve was generated by using the quoted (saturated) value of X_M and omitting the saturation function, S_G, from the model (i.e., fixed saturation). The dashed curve was generated by determining the unsaturated value of X_M, and incorporating the saturation function, S_G, in the induction generator model (i.e., variable saturation). Since the saturation

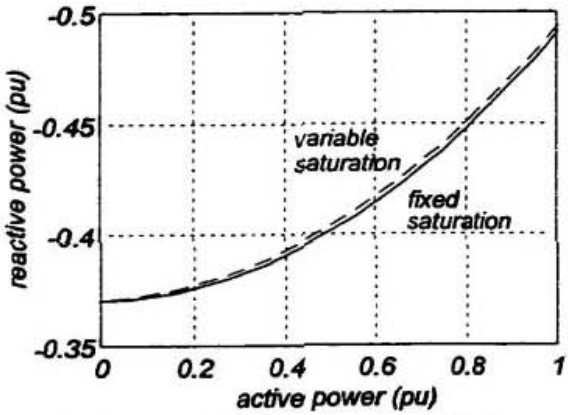

Figure 4.31 IG steady-state P-Q curve.

parameters were not available for this generator, they are assumed to be the same as those determined for a similarly constructed machine [66].

While loading has little effect on the saturation level, variation of the terminal voltage has a much larger impact. Figure 4.32 illustrates the effect voltage has on the reactive power demand of the induction generator at three active power levels (0, 0.5 and 1.0 pu). The slope of the reactive power versus voltage (V-Q) curves were approximately doubled by the

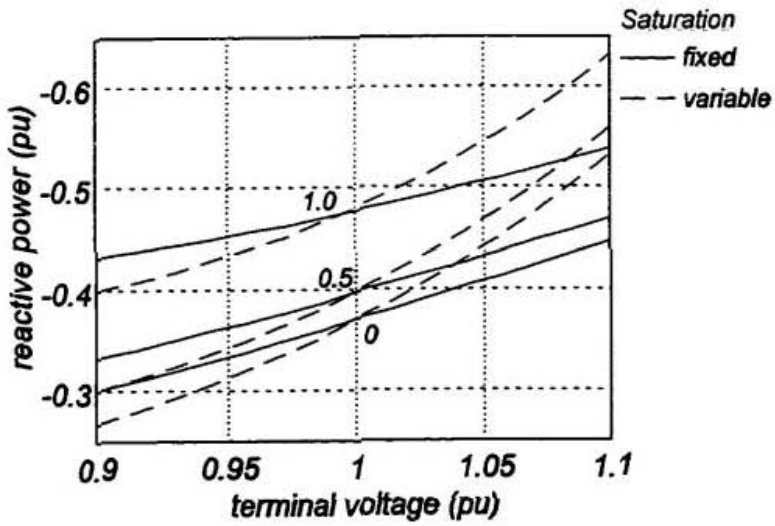

Figure 4.32 V-Q curves for 0, 0.5 & 1 pu active power.

inclusion of saturation.

As with the synchronous generator, saturation of the magnetizing inductance has little effect on the induction generator's transient reactance. Thus the initial transient remains nearly the same for a step voltage input, but the response tends towards a different steady state when variable saturation is included. Figure 4.33 shows the simulated active and reactive IG stator currents for a 5% step increase in terminal voltage. The responses of the full-order (4th-order) model, and the reduced-order (2nd-order) model, are included for both fixed and variable saturation.

The transient current of the full-order IG model includes a 60 Hz component in the synchronous reference frame (Figure 4.33). This translates into a direct current offset in the stationary reference frame. This direct current offset is the stator's transient response to switching all three phases simultaneously [57,58]. In this simulation, the induction generator

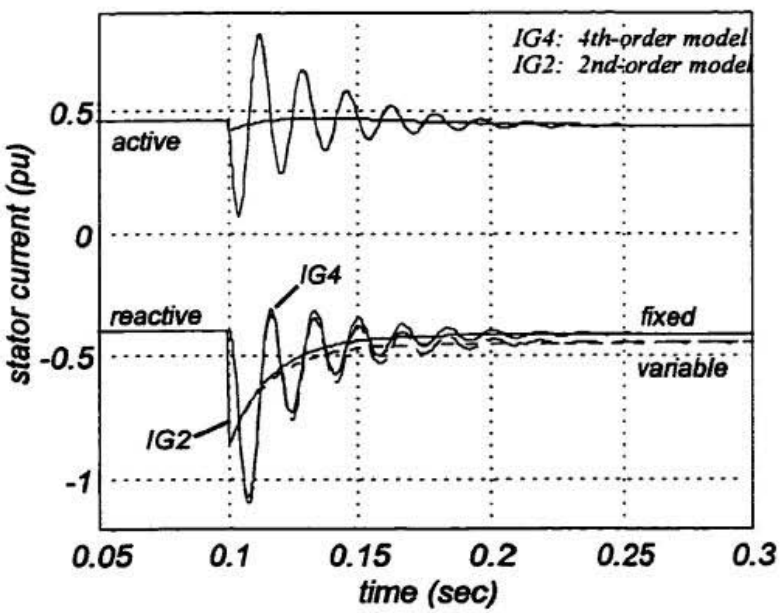

Figure 4.33 IG current response to a +5% voltage step.

was connected to an infinite bus, thus the response of the finite synchronous generator was neglected.

Simulating the induction and synchronous generators together as an autonomous (HPNSWD) system yielded the results in Figures 4.34 and 4.35. The system was initially allowed to reach steady state with no loads, and zero torque on the induction generator. Then a 0.4 pu (0.64 pu SG base) resistive load was applied to the grid. The synchronous generator's rotor speed was held constant for direct comparison to the models.

The induction generator's stator currents (full-order SG and IG models) in Figure 4.34 contain a much lower 60 Hz transient in the synchronous reference frame. The 60 Hz transient would be reduced further, or even eliminated, if the 3-phase load were switched at zero crossings.

The voltage response of the full and the reduced-order generator models, with both fixed and variable saturation in the IG models, differ by up to 10% at the lowest point of the

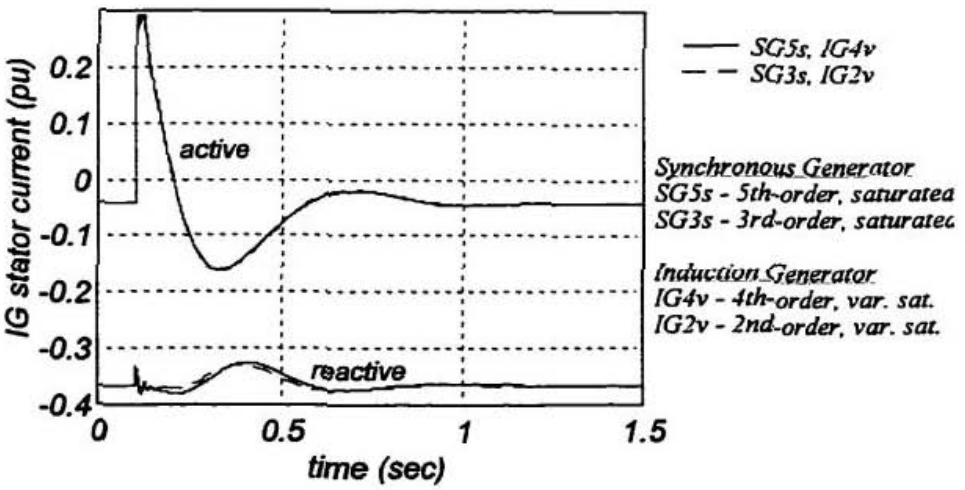

Figure 4.34 IG stator current, +0.4 pu load, HPNSWD.

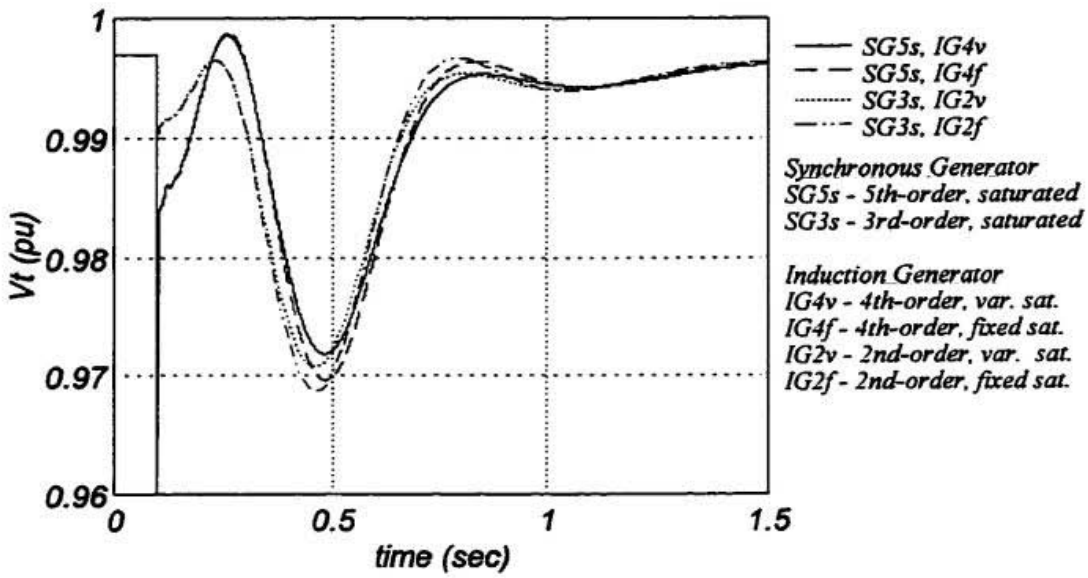

Figure 4.35 HPNSWD voltage response, +0.4 pu load step.

transient (Figures 4.35). With the transient resulting from neglecting variable saturation of the induction generator approximately 5% larger at this point. This is a result of reduced damping when variable saturation is neglected. As with the synchronous generator, variable saturation of the induction generator increases the damping in the voltage system.

The most significant difference between the response of the full and reduced-order models is the initial transient, which is twice as large for the full-order model. This is due to the reaction of the stator transients to the fast load transient.

The effects of a rotor speed transient would be reduced in this case, simply because the large inertia of the wind turbine would reduce the size of the speed transient.

As with the synchronous generator model, without more rigorous verification of the induction generator model, it is difficult to determine whether the differences between the full and the reduced-order models are significantly greater than the inherent errors of

modelling and the accuracies of the parameters.

Assuming that the component models and parameters are representative of a wind-diesel system of this size, the reduced-order generator models produce optimistic voltage responses to high speed transients, and neglecting generator saturation results in more pessimistic voltage responses.

Chapter

5 HPNSWD Frequency and Voltage Control

A fundamental requirement of a wind-diesel system is that the addition of wind power to the autonomous diesel generator system should not degrade the power quality (frequency and voltage performance) of the system from that of the diesel generator(s) operating alone. This is based on the premise that the system was originally an autonomous diesel generator system, and that the power quality of the diesel generator(s) is satisfactory.

The diesel generator(s) of the existing system will have been specified to meet the requirements of the village load. In a HPNSWD system, the addition of wind power to the system can greatly increase the active and reactive power fluctuations in the system. This increased variability may require that the frequency and voltage control systems of the diesel generator(s) be augmented. In addition, to maximize diesel fuel savings, the HPNSWD system must be able to operate solely from wind power with the diesel engine(s) shut down. This mode of operation requires a frequency control system independent of the diesel engine.

This chapter explores the frequency and voltage control of a HPNSWD system.

5.1 Frequency Control

The frequency of an autonomous power system remains constant as long as the power supplied and the power demanded remain balanced. A power imbalance will accelerate or decelerate the rotational velocities of the system, causing the system frequency to increase or decrease, respectively. The diesel generator regulates the system frequency by controlling the amount of power developed by the diesel engine. The AOC 15/50 wind turbine used in this study is a fixed pitch, constant speed, passive yaw turbine. Therefore there is no control mechanism to regulate the power output of the wind turbine. The only method to maintain a constant frequency in the system is to absorb the surplus power produced by the wind turbine. The diesel engine is capable of being back-driven to absorbing some excess power (up to 30% of rated power for short periods [10]). But the unidirectional coupling between the engine and the synchronous generator prevents the diesel engine from being used in this way. In addition, the significant capacity of the wind turbine, relative to the diesel generator, and the sluggish response of the diesel's speed governor make back-driving the diesel an undesirable method for dynamic frequency control.

A more desirable approach is to use a fast acting programmable dump load to absorb any surplus wind power in the system, thus maintaining the power balance and a constant system frequency. The controller which controls the dump load and regulates the frequency under conditions of surplus wind power is referred to here as the *dump load controller*.

As stated in Chapter 1, a HPNSWD system has three distinct modes of operation which are determined by the relative levels of the wind power and the demand (village) load. Refining the list from Chapter 1, these three operational modes are:

1. The instantaneous demand load minus the instantaneous wind power is greater than the diesel's minimum loading level (wind power seen as a negative load). The diesel generator regulates the system frequency.
2. The instantaneous demand load minus the instantaneous wind power is less than the diesel minimum loading level. The diesel engine continues to operate. The diesel generator and the dump load controller work in parallel to regulate the system frequency and to maintain a minimum load on the diesel.
3. The wind power exceeds the demand load and the wind conditions are sufficient to allow the diesel engine to be safely shut-down. The dump load is now solely responsible for regulating the system frequency.

The power quality must be maintained within each mode, as well as during the transfer between consecutive modes. This requires that the dump load controller be stable when operating with the turbine alone, with the diesel generator and the wind turbine operating in parallel, and with the diesel alone. The latter scenario is not a requirement if the dump load is automatically disabled in the diesel only configuration.

5.1.1 Frequency Control Strategy

The proposed control strategy is for the dump load controller to maintain a constant

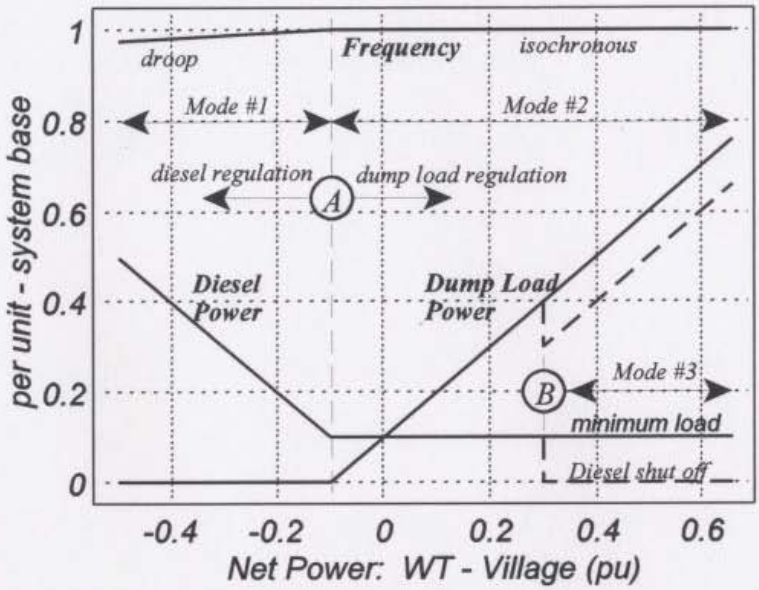

Figure 5.1 Frequency control strategy.

frequency (isochronous regulation) in modes #2 and #3, and to allow the frequency to droop in mode #1 when the diesel generator controls the frequency. Operating the diesel generator in droop mode simplifies the parallel operation of the dump load controller and the diesel generator. If the diesel generator were to operate in isochronous mode, an additional control loop would be required to ensure minimum loading of the diesel and to maintain stability between the two frequency controllers.

The proposed control strategy is illustrated in Figure 5.1. The horizontal axis of the graph represents the net power of the wind turbine and the village load, where the power of the village load is considered negative. The vertical axis of the graph represents per unit power and frequency.

To the left of point *A* in Figure 5.1 the diesel generator satisfies the net power shortage and the frequency is drooped according to the diesel generator's output level. In this

application the diesel's full-load frequency droop is set to 3%.

As the net WT/Village power increases and the diesel reaches its minimum loading level (point *A* in Figure 5.1) the dump load becomes active and the system inherently switches from diesel frequency regulation (droop) to dump load frequency regulation (isochronous). With the dump load controller's reference frequency set to the nominal system frequency (60Hz), and with the diesel governor's reference frequency set such that the diesel generates its minimum loading level at the nominal system frequency, both the smooth transition between diesel regulation and dump load regulation, and the maintenance of minimum diesel loading are intrinsic. Points to the left of *A* correspond with diesel frequency regulation and the HPNSWD's operational mode #1. Points to the right of *A* correspond with dump load frequency regulation and the HPNSWD's operational modes #2 and #3.

Under certain conditions, determined by the systems supervisory control, where the net WT/Village power is consistently large enough, the diesel engine may be shut down. This point is arbitrarily indicated by point *B* in Figure 5.1. The dashed lines for diesel and dump load powers represent the system's operation in mode #3 (diesel engine off).

While operating solely from wind power the supervisory controller, which is not covered in this thesis, must closely monitor the wind turbine and village powers to anticipate a power shortfall and start the diesel engine ahead of time to prevent a system frequency collapse. According to Mahon [70], diesel generators using conventional electric motor starters can be up to full speed in 6 to 8 seconds, provided the engine's coolant and lubricating oil are kept heated. Referring to the windspeed spectral density in Figure 1.3 it can be seen that the spectral density below 8 seconds is low. Therefore a supervisory control

algorithm that can identify an unacceptable risk of system frequency collapse, and bring the diesel back on-line to prevent the collapse, is conceivable. In addition to preventing frequency collapse, the supervisory controller should maximize the diesel's off time while minimizing the diesel's start-stop cycling. The diesel's off time and start-stop cycling are determined by the large spectral density in the 30 second to 5 minute range of Figure 1.3. Although the start-stop cycling versus storage capacity of a wind-diesel system with storage has been studied [3,10,20], the author recommends further research specifically on optimal HPNSWD supervisory control algorithms.

5.1.2 Allowable Frequency Variation

According to Hunter et al. [10] there are no limits for permissible power system frequency deviations stated in current (1994) international publications. In addition, they argued that electrical components and appliances should normally tolerate frequency deviations of at least ±3%. A survey of standards from the Canadian Standards Association (CSA) revealed no requirements for appliance operation at other than the rated supply frequency, unless a frequency range is specified by the manufacturer [71]. On the other hand, CSA specifies that medical equipment must operate over a supply frequency range of ±1 Hz from nominal [72]. This ±1 Hz limit presents a very tight tolerance for an autonomous system (diesel or wind-diesel) and is likely based on the high frequency stability of large power systems (<1% variation [10]). If medical equipment is to be used in a small power system, care should be taken to ensure that the equipment and the power system are compatible.

Another CSA standard specifies the accuracy of AC electrical power meters for a frequency variation of ±5% of the rated frequency [73]. This standard suggests that an autonomous power system should normally remain within ±5% of the rated frequency.

The Norwegian Wind Energy Programme's design criteria for a wind-diesel project specified that frequency fluctuations should be within the limits of ±4% [20]. No justification is given for these limits, so the author does not know if they are arbitrary or based on Norwegian practice.

An appropriate wind-diesel design criteria for Canada may be the CSA Standard CAN/CSA-C282-M89, *Emergency Electrical Power Supply for Buildings* [74] which specifies "The maximum frequency droop between no load and full load shall not exceed 5% of the rated frequency. The variation of frequency at any constant load shall remain within a bandwidth of ±1%. The frequency dip on the application of full load in one step at the corresponding power factor shall not exceed 10% and shall return to steady-state conditions within 5s." This is the standard adopted in this thesis. The model of the diesel generator

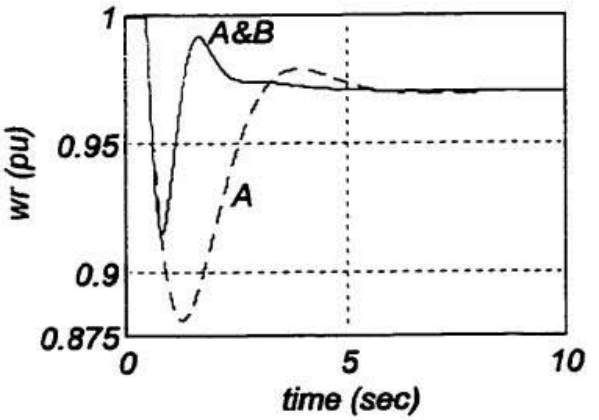

Figure 5.2 Diesel speed response to a full load step.

operating alone using the *Diesels A&B* governor parameters (Figure 5.2, curve: *A&B*) meets the CSA's frequency dip on full load application specification, but fails if the *Diesel A* parameters are used (Figure 5.2, curve: *A*).

5.1.3 Frequency Transducers

In order to regulate the system frequency, the instantaneous system frequency must be determined. Speed governors on diesel generators determine the system frequency by measuring the rotational speed of the engine. The speed transducer of an electronic governor is usually comprised of a magnetic pick-up which is excited by the teeth of the flywheel starter ring gear [70]. Due to the high number of teeth on the ring gear the speed transducer's response time can be very fast (<10 ms). Since the dump load controller must continue to operate when the diesel engine has been stopped, the speed transducer on the engine cannot be used as the frequency input to the dump load controller.

The synchronous generator continues to rotate when the diesel engine has been shut off, therefore a similar electromagnetic or optical encoder could be fitted to the shaft of the synchronous generator for use by the dump load controller. But a frequency transducer on the generator shaft would only be practical if the dump load and diesel generator can be placed in the same location. In practice the dump load will most likely be a deferrable heating load located in the village, which may be several kilometres from the diesel generator.

To determine the system frequency at the site of the dump load the electrical frequency of the grid voltage can be measured directly with a frequency-to-voltage converter, or indirectly by comparing the grid's electrical phase to a stable reference frequency. The

susceptibility of these types of frequency transducers to noise and waveform distortion has not been considered in this study.

5.1.3.1 Phase Detector

A dump load controller operating with a phase detector as its frequency transducer is essentially a phase-locked loop frequency controller. Phase control is the control technique employed by Hydro-Québec at AWTS [75] and by Consoli et al. [76]. A phase detector is used to measure the phase difference between the grid voltage and a stable reference frequency generated locally. In both applications the phase detector employed is a digital phase-frequency detector [77]. The output of the detector is the integral of positive pulses for a leading phase and negative pulses for a lagging phase. Consoli et al. measure only a single phase of the three-phase system, therefore the detector's pulse train is only 60Hz for a 60Hz system. Hydro-Québec, on the other hand, passes all three phases through a bridge rectifier and measures the phase of the resulting fundamental frequency which is six times higher than the grid frequency. This results in a detector pulse train of 360Hz for a 60Hz system.

The model of the phase detector implemented by Hydro-Québec is shown in Figure 5.3. It was determined from the block diagram of the dump load regulator in Jean et al. [75]. The phase detector is approximated in the model by an integral of the frequency error followed by filters to band limit the signal and remove the fundamental and harmonics of the detector pulse train from the DC output signal.

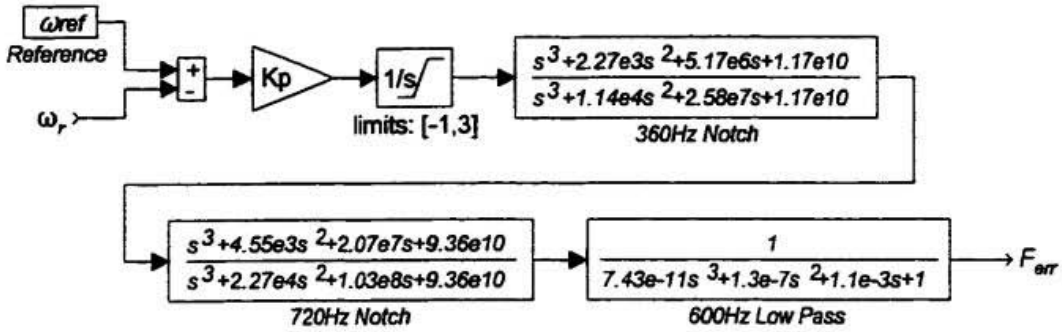

Figure 5.3 Phase detector model.

5.1.3.2 Frequency Detector

Commercial frequency transducers are generally intended for supply monitoring. Although they are quite accurate, they require several frequency cycles to determine the grid frequency. The response times of these types of frequency transducers are usually in the range of 150 to 400 ms [78,79], which is too slow for this application.

A frequency detector comparable to Hydro-Québec's phase detector is a frequency-to-voltage converter (FVC), such as the LM2907 [80], which produces a DC voltage proportional to the input frequency. The input to this FVC is the 360Hz from the 3-phase bridge rectifier. The LM2907 actually has an output pulse rate that is double the input frequency. But for direct comparison with the phase detector, a hypothetical FVC with an output pulse rate of 360Hz is considered here. By using the same filters as the phase detector the model of the 360Hz FVC is the same as that of the phase detector illustrated in Figure 5.3 without the integrator block.

To demonstrate the effect the speed of the frequency transducer has on the system,

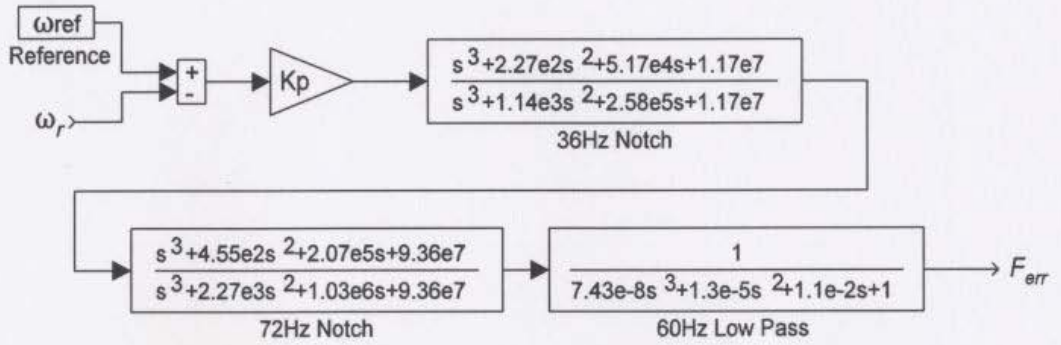

Figure 5.4 36Hz frequency-to-voltage converter model.

an FVC that is one tenth as fast (output pulse rate of 36Hz) is also included. Figure 5.4 shows the model of the 36Hz FVC. This slower frequency transducer has a response time of 65 ms, which is still significantly less than that of the commercial frequency transducers. Response time is defined here as the time for the step response to reach 90% of its final value.

5.1.4 Dump Load Controller Design

The dump load controller is a proportional-plus-integral-plus-derivative (PID) controller, where the transfer function of the PID controller is:

$$G_{PID}(s) = K_p\left(1 + \frac{K_i}{s} + K_d s\right) \tag{5.6}$$

From the perspective of the dump load controller, the input to the plant is the dump load power setting (power at nominal voltage), and the output of the plant is the output of the frequency transducer, as illustrated in Figure 5.5. The PID controllers were tuned according to Ziegler-Nichols second method [81], which is based on the critical gain, K_{cr}, and the

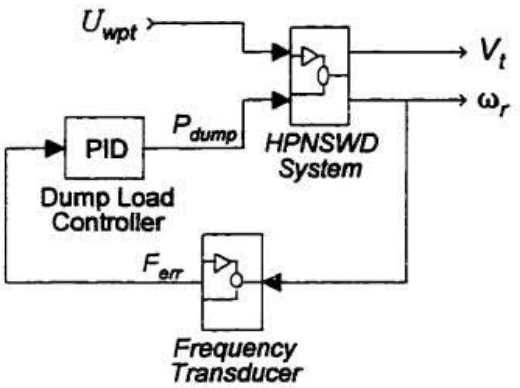

Figure 5.5 Dump load controller block diagram.

corresponding period, P_{cr}, of the plant. The critical gain is the proportional gain for which sustained oscillations occur, and the critical period is the period of the oscillations. The Ziegler-Nichols tuning rules for PI (proportional-plus-integral) and PID controllers are given in Table 5.1.

Table 5.1 Ziegler-Nichols Tuning Rules (Second Method)

Type of Controller	K_p	K_i	K_d
PI	0.45 K_{cr}	$1.2/P_{cr}$	0
PID	0.6 K_{cr}	$2/P_{cr}$	0.125 P_{cr}

To determine the critical gain and period, the open-loop frequency response of the plant was calculated by linearizing the wind-diesel system using SIMULINK's *linmod* function. As mentioned in Section 5.1, the dump load controller must be designed to operate with the three system configurations of: the wind turbine alone (*wind-only*); the wind turbine and the diesel in parallel (*wind-plus-diesel*); and the diesel alone (*diesel-only*). The Bode diagrams for frequency control of the wind-diesel plant in all three configurations, and under

different wind and load conditions, are given in Appendix C. The wind and load conditions were found to have an influence on the frequency response of the plant, but the effects are only in the lower frequencies, which are well away from the critical design frequencies.

The dump load controller parameters determined for the three different frequency transducers are listed in Table 5.2. The proportional-plus-derivative (PD) parameters for the phase detector were first determined from the Ziegler-Nichols parameters for a PI controller with the 360Hz FVC. This is based on the fact that a phase detector integrates the frequency error, thus a phase detector followed by a PD controller functions the same as a frequency detector followed by a PI controller, i.e.,

$$\left(\frac{1}{s}\right) K_p\left(1 + K_d s\right) = K_d K_p\left(1 + \frac{1}{K_p s}\right) = K_p'\left(1 + \frac{K_i'}{s}\right) \tag{5.7}$$

The Ziegler-Nichols parameters for the phase detector in the *wind-plus-diesel* configuration yields only a 25° phase margin in the *wind-only* configuration. Therefore the parameters were adjusted manually to attain a minimum of a 45° phase margin in all three system configurations.

Table 5.2 Dump Load Controller Parameters

Frequency Transducer	K_p	K_i	K_d
Phase Detector	144	0	0.1
360Hz FVC	60	20	0.0125
36Hz FVC	9.6	12.5	0.02

5.1.5 Dump Load Controller Performance

The Bode diagrams of the dump load control loop with the phase detector, the 360Hz FVC and the 36Hz FVC are shown in Figures 5.6, 5.7 and 5.8, respectively. The bandwidth of the 360Hz FVC frequency control loop is approximately 2.5 times larger than that of the phase control loop even though they operate at the same pulse rate. This is because the phase controller is essentially a PI controller, while the frequency controller is a PID controller. In order to have a PID control response with a phase detector frequency transducer, the dump load controller would have to have a proportional, derivative and second-order derivative response.

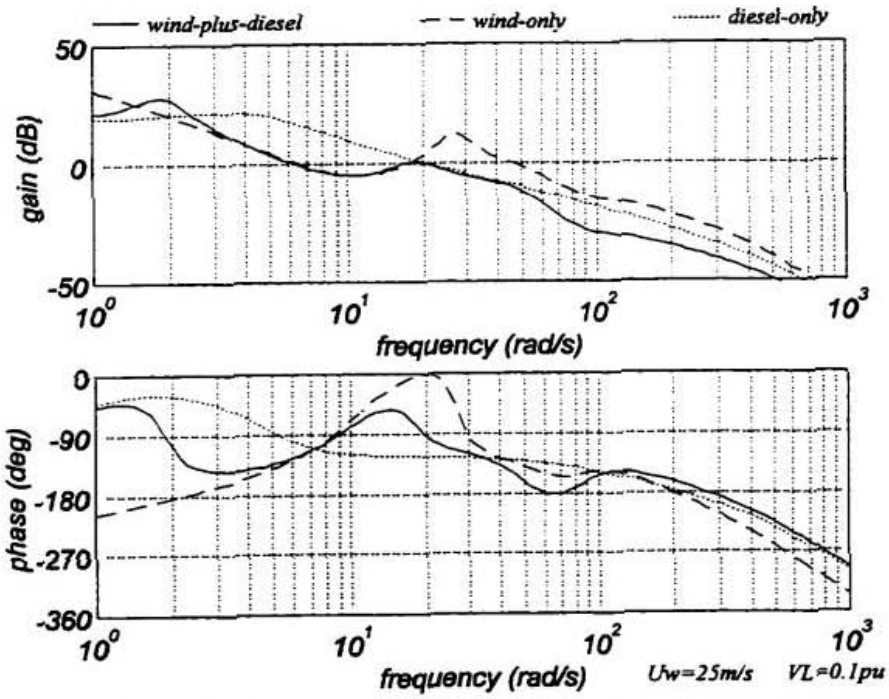

Figure 5.6 Bode diagram of phase detector dump load control loop.

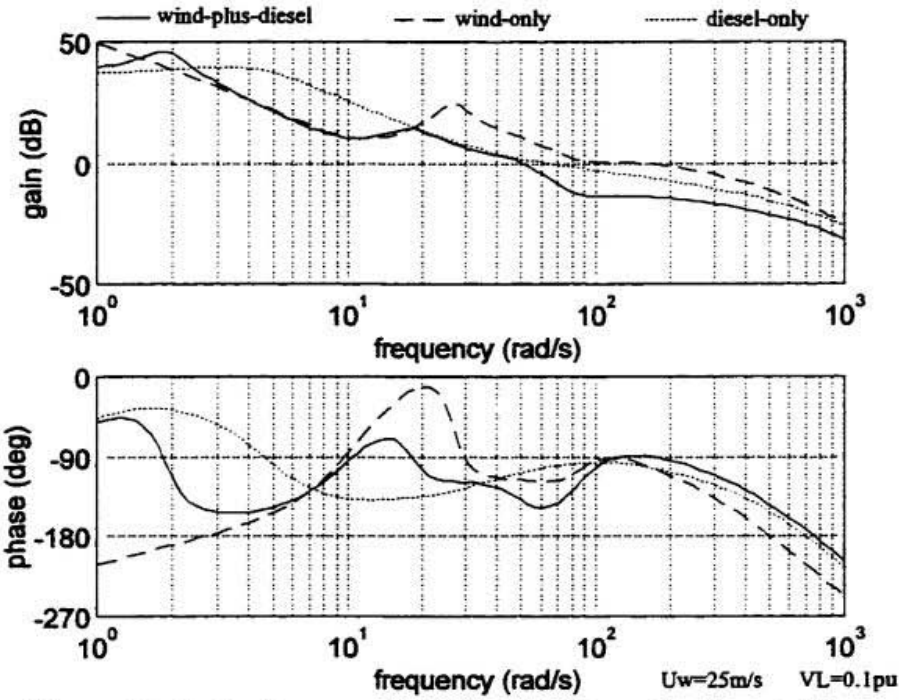

Figure 5.7 Bode diagram of 360Hz FVC dump load control loop.

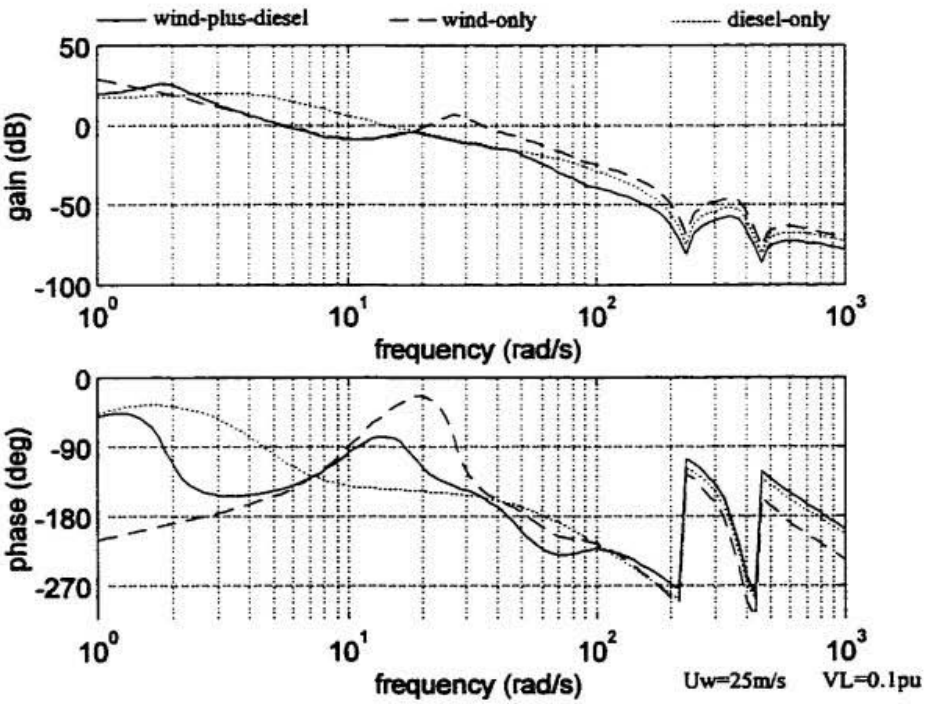

Figure 5.8 Bode diagram of 36Hz FVC dump load control loop.

As expected, the bandwidth of the 36Hz FVC frequency control loop is approximately one tenth that of the 360Hz FVC frequency control loop. The response of the 36Hz FVC frequency controller is underdamped (see Figures 5.9 and 5.10), but satisfactory. Referring to Figure 5.8, the *wind-only* configuration of the 36Hz FVC control loop has a 180° phase shift at 2.5 rad/s and at 50 rad/s. If the speed of the frequency transducer were slightly slower, the gain of the control loop above 2.5 rad/s would be reduced to the point where the system would have an instability at 2.5 rad/s. Therefore 65ms can be considered as the approximate lower limit for the frequency transducer speed.

The dump load controller easily meets the CSA specification of a maximum 10% frequency dip on full load application (Figure 5.9), where 'full load' is the diesel's rated full load, i.e., 0.625pu at 0.8PF lagging. The ripple that remains in all three responses after the transients settle is due to the dump load having a discrete rather than a continuous response.

A more extreme, non-fault load transient that must not disrupt the operation of the

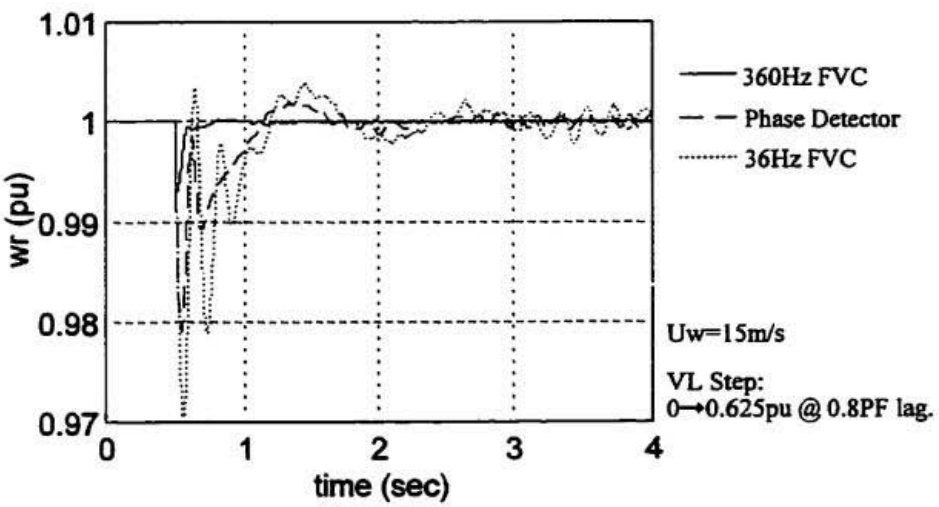

Figure 5.9 *Wind-only* frequency response to a (diesel) full load step.

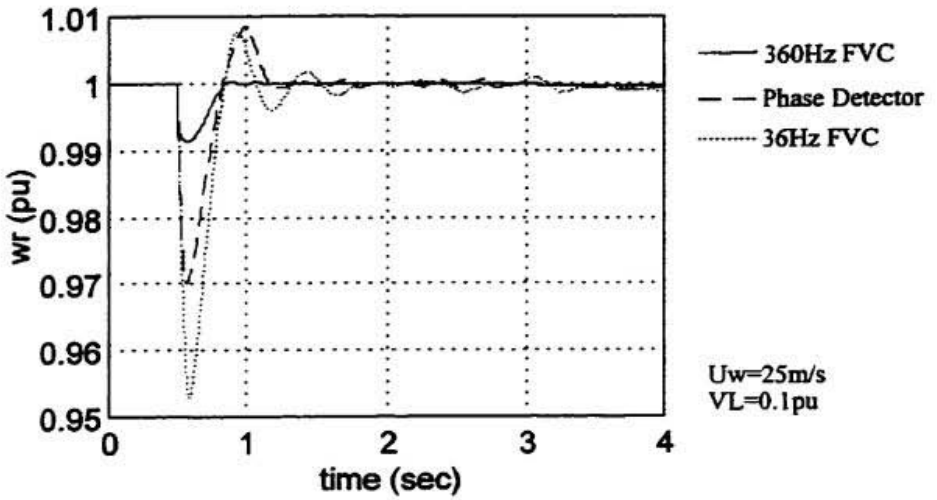

Figure 5.10 ***Wind-plus-diesel*** **response to a WT disconnect at 25m/s.**

wind-diesel system is the disconnection of the wind turbine at full output power. This corresponds to the high wind wind turbine shut-down discussed in the previous chapter. This event is likely to occur from time to time, therefore the system should at least meet the full load step requirement. The system frequency transients with the three frequency transducers is shown in Figure 5.10. The village load in this case is 0.1pu, which is the same as the diesel minimum loading level of 20%, therefore, ideally, the diesel should not see any significant active power transient. This is nearly the case with the fast acting 360Hz FVC frequency controller, but with the slower acting controllers it takes longer to turn off the dump load, thus requiring the diesel generator to bring the system back up to nominal frequency. As the village load increases, the dump load level before the wind turbine shut-down decreases. Therefore there is less impact from the delay in turning off the dump load, and the resulting response tends toward the response of the diesel generator to the net load step.

Another benefit of a faster acting dump load controller is that it dampens the swing

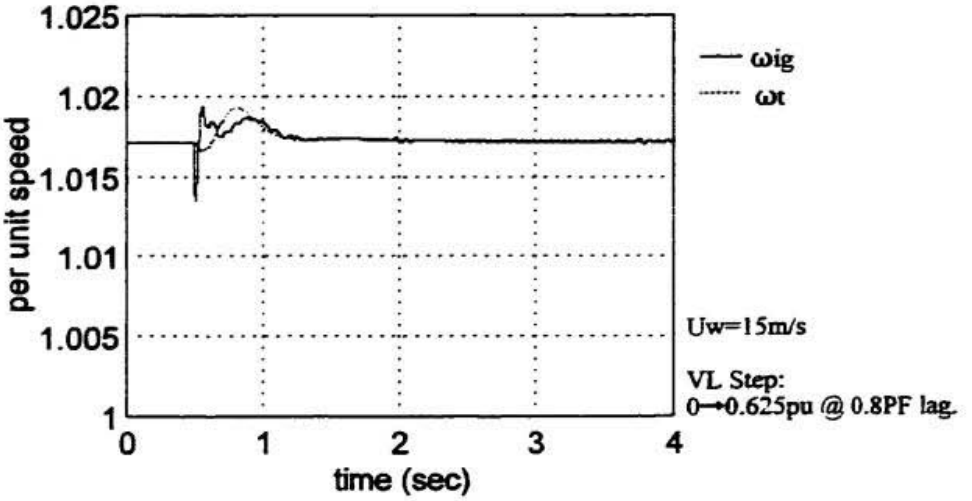

Figure 5.11 ***Wind-only*** **WT swing with 360Hz FVC.**

of the system against the wind turbine's rotor. This should have a significant effect on fatigue in the wind turbine. For comparison, Figures 5.11 through 5.13 illustrate the swing of the induction generator (ω_{ig}) against the turbine's rotor (ω_t) for a 0.625pu, 0.8PF lagging load step in the *wind-only* configuration. The swing is very small and well damped with the

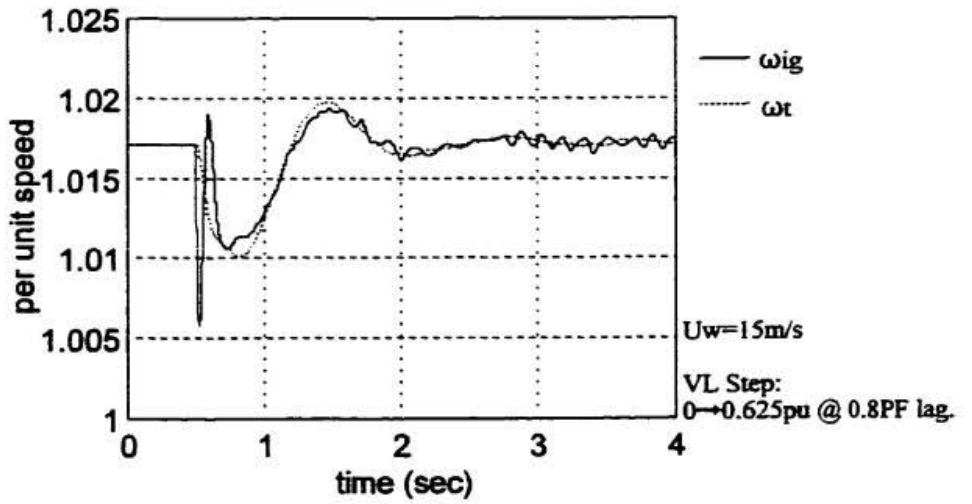

Figure 5.12 ***Wind-only*** **WT swing with phase detector.**

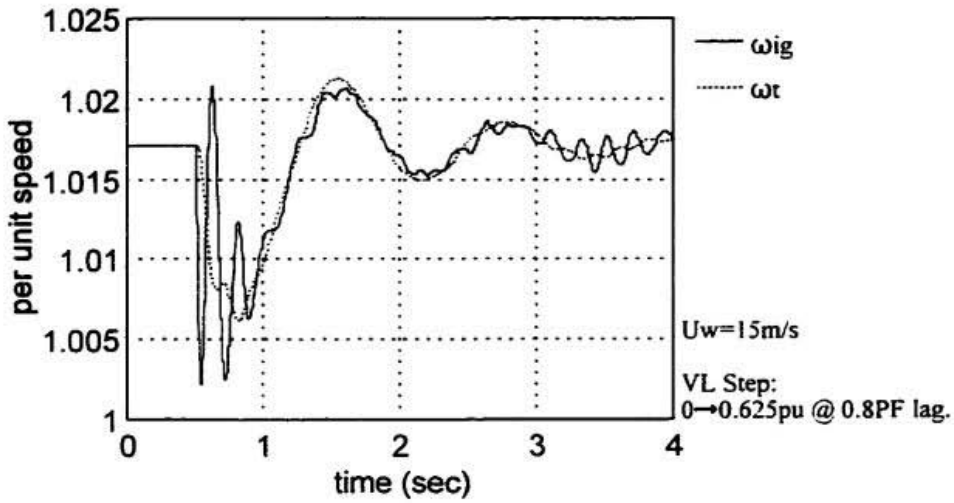

Figure 5.13 ***Wind-only*** **WT swing with 36Hz FVC.**

360Hz FVC frequency controller (Figure 5.11), meanwhile it becomes large and lightly damped with the much slower 36Hz FVC frequency controller (Figure 5.13).

5.2 Voltage Control

The voltage of the network is most effectively regulated by controlling the reactive power in the system. The AVR of the diesel generator regulates the network voltage by controlling the amount of reactive power produced (or absorbed) by the diesel's synchronous generator. The synchronous generator remains operational at all times. When the diesel engine is off the synchronous generator functions as a synchronous condenser.

A village load normally consists of many small loads. Therefore the synchronous generator typically sees relatively small reactive and active power fluctuations. The wind

turbine, on the other hand, is an electric machine with a capacity comparable to, if not larger than, the capacity of the synchronous generator. The induction generator of the wind turbine also requires a large amount of reactive power for excitation. The start-up and shut-down of the wind turbine cause sudden changes in the reactive and active power in the system. In addition, both the reactive and active power of the turbine can fluctuate widely in turbulent wind conditions. These rapid power fluctuations can cause voltage variations that are detrimental to the operation of voltage sensitive loads and/or result in objectionable disturbances to lighting levels.

5.2.1 Allowable Voltage Variation

Voltage variation can be divided into slow variations, averaged over a few minutes or hours, and rapid fluctuations, or flicker. CSA Standard CAN3-C235-83 [82] sets the slow voltage variation limits, under normal operating conditions, to +4.2/-8.3% of nominal. The International Electrotechnical Commission's (IEC) Publication 38 [10] recommends less stringent voltage limits of ±10% of nominal.

Light fixtures tend to flicker when exposed to rapid voltage fluctuations. Television receiver and other sensitive electronic equipment may also be adversely affected. Due to the sensitivity characteristics of the human eye, the degree to which light flicker is objectionable depends not only on its magnitude but also on its frequency. Figure 5.14 illustrates the visual sensitivity resulting from sinusoidal voltage fluctuations on incandescent lighting [83]. Also included in the figure is the IEC Publication 555-3 flicker limit, as presented in Reference

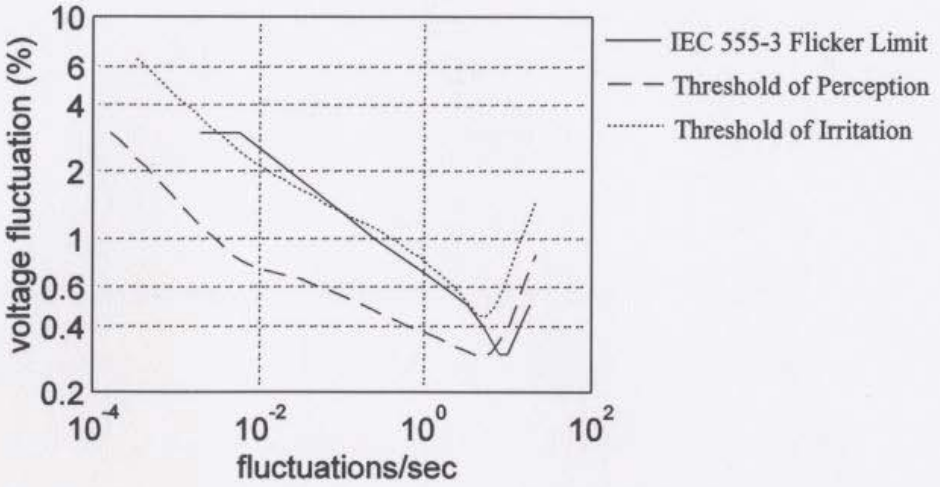

Figure 5.14 Visual response to flicker and IEC Flicker Limit.

84.

Concerning the connection and disconnection transients of the wind turbine, a utility engineer's rule of thumb, quoted by Brothers, Rong and Moll [85], states that the connection of any load should not cause more than a 5 volt (4.2%) variation locally. Alternatively, the connection transients could be likened to large motor starts in Miller [83], which are limited to 1-3%, depending on the frequency. This latter limit would likely fall within the IEC flicker limit.

5.2.2 Voltage Quality from the Synchronous Generator

The HPNSWD system was simulated with the synchronous generator as the only source of voltage control. To predict the network voltage transients caused by disconnecting the wind turbine, both a high wind shut-down ($U_w = 25$ m/s) and a low wind cut-out ($U_w = 0$ m/s) were simulated. The transients due to the wind turbine connection are not considered because a soft-start device is used and the transients are assumed to be minimal. The frequency with

which the wind turbine connections and disconnections occur depends on the wind conditions and the wind turbine's start-stop time-outs programmed in the supervisory control. It is assumed that the time-outs are set such that the minimum time between connections is at least 5 minutes. Thus the transients due to the wind turbine disconnection should meet the voltage fluctuation limits set for load connections and large motor starts of 3-4%.

The network voltage fluctuations due to the disconnection of the wind turbine are shown in Figure 5.15. The voltage presented in the figure is the voltage at the village junction point (node 4 in Figure 3.15). The magnitudes of the voltage fluctuations are 8% and 12.5% for a low wind cut-out and a high wind shut-down, respectively. Both are well above the specified limit of 3-4%. Due to the high gain of the AVR and the low network impedance the steady-state voltage error is negligible.

Because of the randomness of the wind and the frequency dependence of flicker limits, the actual flicker emission levels that can be expected due to wind turbulence is difficult to predict. Thiringer [84] predicts the voltage fluctuations on different feeder line

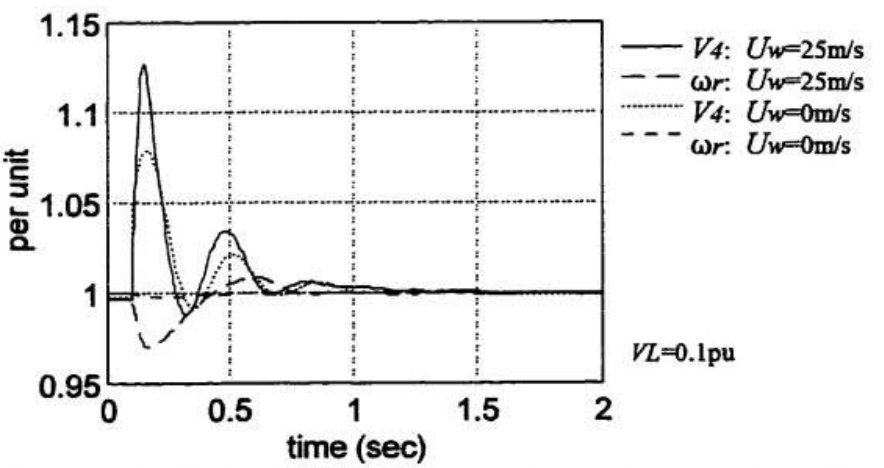

Figure 5.15 Wind turbine disconnect with synch. generator only.

impedances due to a two-turbine wind park, but his analyses only include steady-state voltage variation resulting from slow windspeed variation, and the measured periodic power pulsations of the turbines due to wind shear and tower shadow. No attempt was made to predict flicker emission levels due to wind turbulence.

Sørensen et al. [86] present a method to predict flicker emission levels for any grid and wind condition once a *flicker coefficient* has been determined for the wind turbine. The method is quite involved and beyond the scope of this thesis.

For the purposes of this study, voltage fluctuations due to sudden changes in the point windspeed are simulated in order to determine the susceptibility of the system to turbulence induced flicker. The wind turbulence used for determining the flicker emission is shown in Figure 5.16. It is based on a nominal windspeed of 8 m/s. The point windspeed, U_{wpt}, has a step increase to 20 m/s at t = 0s, followed by a step decrease to 5 m/s at t = 10s. The windspeed then returns to nominal at t = 20s. The effective windspeed, U_w, and the torque developed by the wind turbine's rotor, T_R, are also included in the figure. This turbulence is not presented as typical, but only as a test to illustrate the system's response to abrupt turbulence.

The flicker emissions of the wind-diesel system due to this test turbulence are shown in Figure 5.17. The diesel engine is operating and the village load is a constant 0.1 pu active power. The amplitude of the largest voltage fluctuation is 0.9%, with a fundamental frequency of approximately 0.5 Hz. According to Figure 5.14, this would place it above the threshold of irritation and the IEC flicker limit. With this response, certain wind conditions may cause the HPNSWD system to fail the IEC flicker standard and/or generate customer

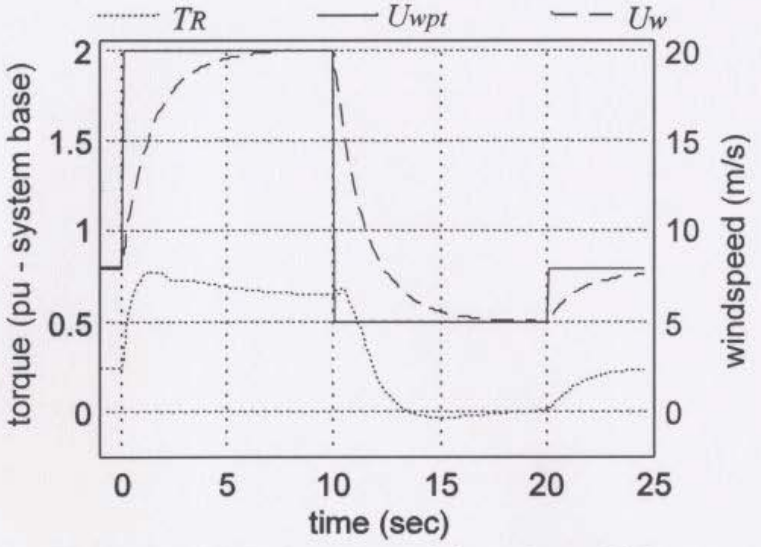

Figure 5.16 Windspeed used for voltage flicker test.

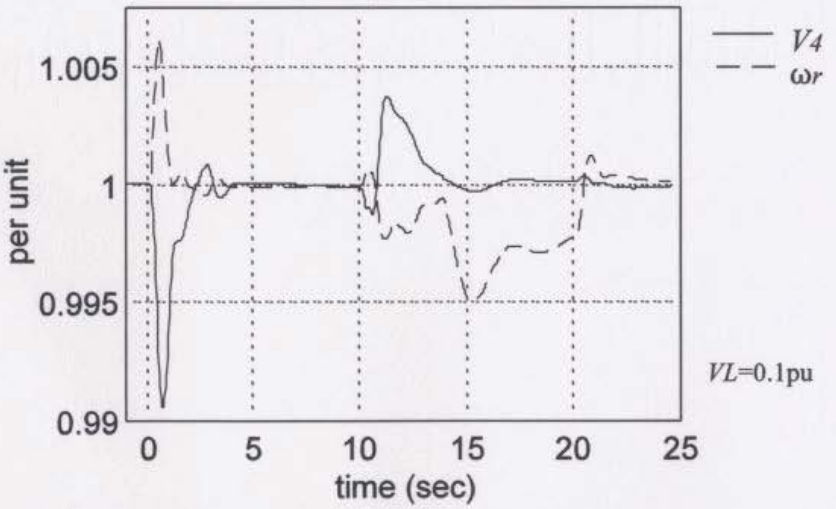

Figure 5.17 Flicker with synchronous generator only.

complaints. Detailed characterization of the wind at the proposed wind turbine site would be required to determine whether such wind conditions were likely to occur.

5.2.3 Voltage Quality with an Added Capacitor Bank

Upon disconnection of the wind turbine the network sees a 0.24 to 0.31pu reactive power load step. Additional power losses are also incurred in the transmission lines and transformers that carry these high reactive currents between the synchronous generator and the induction generator. In many installations a capacitor bank is connected near the wind turbine to offset the reactive load of the wind turbine on the grid. In this application the capacitor bank is connected to the wind turbine at node 6 of Figure 3.15. It is represented as a constant reactance in the network admittance model.

The capacitor bank is switched on and off in conjunction with the wind turbine. Therefore it reduces the reactive power load step upon disconnection of the wind turbine to the difference between the reactive power of the capacitor bank and the reactive power of the wind turbine.

Figure 5.18 illustrates the voltage fluctuations due to a wind turbine disconnection with a 30 kVAr (0.3pu) capacitor bank connected to the wind turbine. The magnitudes of the

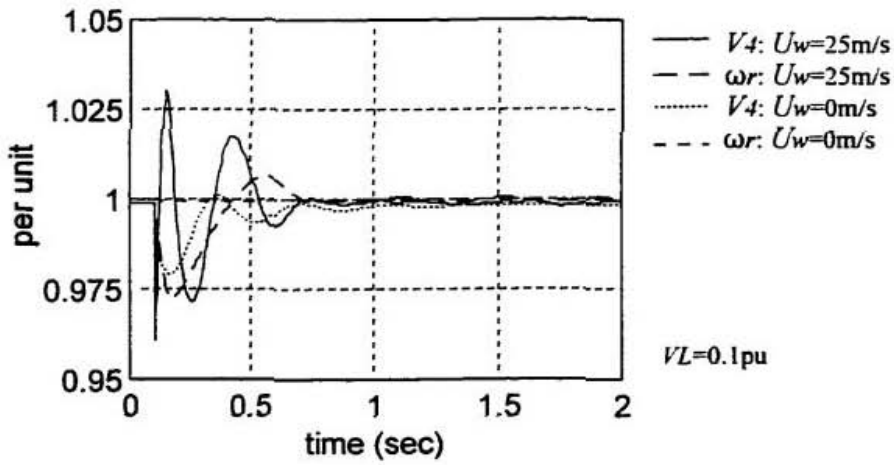

Figure 5.18 Wind turbine disconnect with capacitor bank.

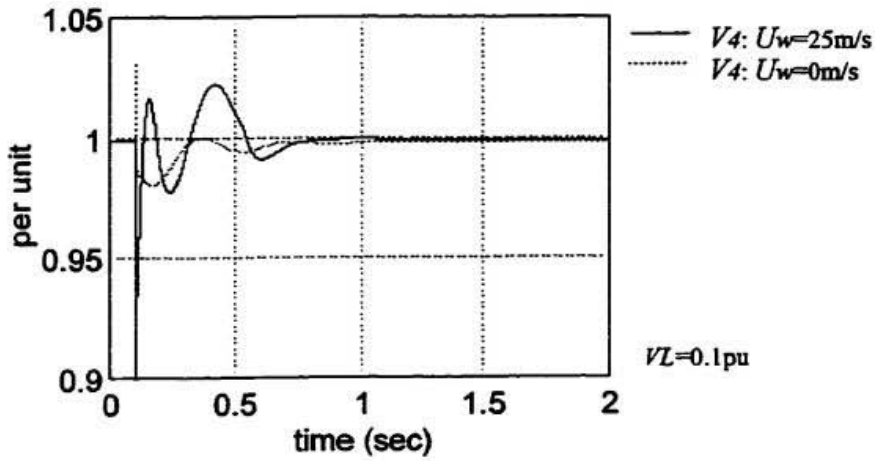

Figure 5.19 WT disconnect with capacitor bank, full-order model.

voltage fluctuations are approximately 2% and 3% for a low wind cut-out and a high wind shut-down, respectively.

Because the voltage response is marginal and the frequency dip for the high wind shut-down is significant (3%), this scenario is repeated using the full-order generator models to include the frequency transient effects. The response of the full-order model in Figure 5.19 reveals that for a high wind shut-down the first positive transient is significantly smaller (1.5% instead of 3%), as is the negative transient that follows (2.2% instead of 3%).

The negative voltage spike immediately after the wind turbine disconnects, which is mostly caused by the delayed response of the dump load controller, is substantially larger at approximately 8%, instead of the 4% spike predicted by the third-order synchronous generator model. It would take a much faster acting voltage controller than can be achieved with the slow response of the synchronous generator to compensate for this voltage spike. Because the frequency transient is negligible for the low wind cut-off, the voltage fluctuation remains virtually the same for the reduced-order and full-order simulations.

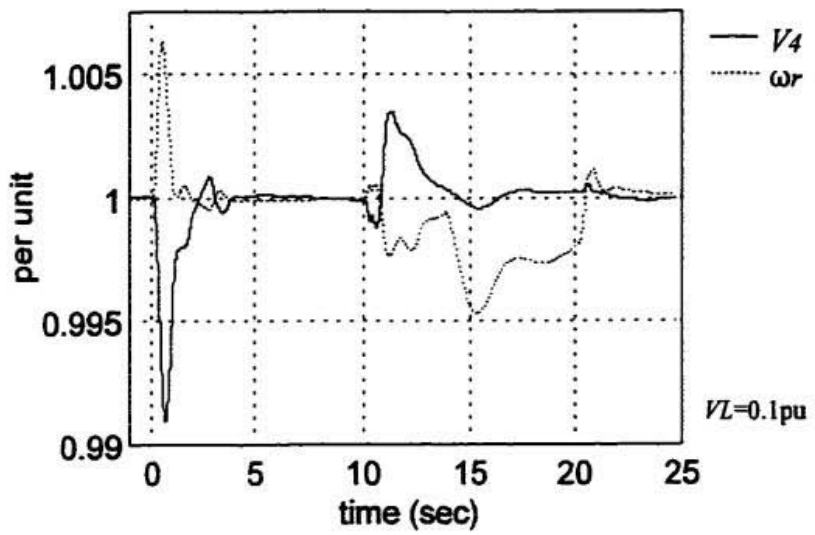

Figure 5.20 Flicker with added capacitor bank.

The flicker emissions due to the test turbulence with the capacitor bank connected is shown in Figure 5.20. Because the capacitor bank does not change the magnitude of the power fluctuations due to turbulence, the flicker remains virtually unchanged.

5.2.4 Static VAR Compensator

The results with fixed reactive power compensation (i.e. a capacitor bank) in the previous section indicate that dynamic reactive power compensation is required. Either a static VAR compensator (SVC) or a synchronous condenser can provide dynamic reactive power compensation. However, because of their high capital and operating costs, synchronous condensers have been largely superseded by SVC's [58]. In addition, synchronous condensers generally have slow control responses compared to SVC's [83].

A modern SVC comprises a force-commutated inverter. The inverter operates at the high switching frequencies made possible by employing fast switching devices such as

insulated-gate bipolar transistors (IGBTs) or gate-turn-off thyristors (GTOs). With these high switching frequencies the SVC's harmonic currents are low and its response time can be very fast. Modern force-commutated SVCs are capable of compensating the harmonic currents generated by other sources up to at least the seventh harmonic [87]. SVCs are also capable of balancing the phase voltages, and, with sufficient internal energy storage, they can even balance the phase active powers. An SVC could be used to regulate the grid voltage while the diesel generator is shut down. The SVC would replace the function of the synchronous condenser, thus eliminating the need for a clutch on the diesel generator. An AC-DC-AC force-commutated converter on a variable speed wind turbine, such as the experimental converter on the Lagerwey wind turbine at AWTS, could also be incorporated with SVC functionality, thus removing the requirement for a clutch on the diesel generator or a dedicated SVC.

For the purposes of this study, only the reactive power compensation and system voltage stabilization capabilities of an SVC are investigated.

A simple model of an SVC used as an *instantaneous reactive power compensator* can be found in Akagi, Kanazawa and Nabae [87]. A variation of that model is presented in Figure 5.21. The differences in the model employed here are: a time constant has been added to the SVC's output; and an optional voltage control loop has been included.

The primary function of the SVC is to negate the instantaneous reactive power of the wind turbine. This is accomplished by measuring the instantaneous wind turbine currents and the instantaneous voltage at node 6 of Figure 3.15. Node 6 is the low voltage side of the transformer, where both the wind turbine and the SVC are connected to the network. The

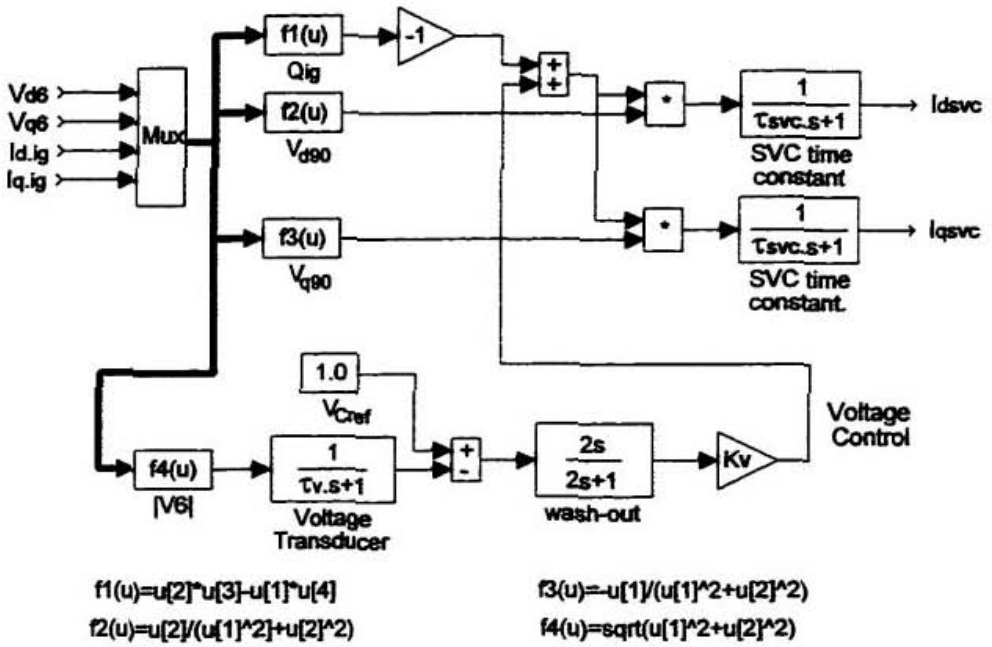

Figure 5.21 Dynamic model of the SVC.

actual phase voltages and currents can be transformed into their direct and quadrature components using Park's transformation (3.18). Akagi et al. transformed the per phase components directly to the stationary reference frame. While, Schauder and Mehta [88] employed a vector resolver (Park's transformation) and a vector phase-locked loop to transform the per phase variables into the synchronously rotating reference frame. In the case of the SVC model represented here, the synchronous generator's rotor reference frame is used. The rotor reference frame is the same as the synchronous reference frame except for the offset of the rotor angle.

The instantaneous reactive power of the wind turbine is:

$$Q_{ig} = V_{q6} I_{d.ig} - V_{d6} I_{q.ig} \tag{5.8}$$

With positive reactive power defined as lagging, the output current of the SVC must lag its terminal voltage by 90° for a positive output, and lead by 90° for a negative output. This is accomplished by determining a vector, V_{90}, which lags the terminal voltage, V_6, by 90°. The magnitude of V_{90} is inversely proportional to the magnitude of V_6, since the output power is proportional to the voltage. The required output current of the SVC, I_{svc}, is then just the vector V_{90} times the negative of instantaneous reactive power Q_{ig}. Thus,

$$V_6 = V_{d6} + jV_{q6} \qquad V_{90} = V_{d90} + jV_{q90} \qquad I_{svc} = I_{dsvc} + jI_{qsvc} \tag{5.9}$$

$$V_{d90} = \frac{V_{q6}}{V_{d6}^2 + V_{q6}^2} \qquad V_{q90} = -\frac{V_{d6}}{V_{d6}^2 + V_{q6}^2} \tag{5.10}$$

$$I_{dsvc} = -V_{d90}\,Q_{ig} \qquad I_{qsvc} = -V_{q90}\,Q_{ig} \tag{5.11}$$

The SVC's output time constant, τ_{svc}, depends on the output filters, which are determined by the switching frequency of the inverter. An arbitrary value of 5 milliseconds has been chosen for this study.

A voltage control loop is included in the SVC to improve its performance. The voltage control loop has a proportional gain, K_v, which modifies the SVC's reactive power output. A wash-out filter was added to the voltage control loop to force the SVC to respond only to voltage transients. The steady-state voltage control remains with the synchronous generator. The time constant of the voltage transducer, τ_v, represents the necessary voltage filtering. A time constant of 5 milliseconds was chosen since it is typical for AVRs used with similarly rated synchronous generators.

The SVC is incorporated into the wind-diesel model by adding another port to the

network admittance model (documented in Appendix B) and by transforming the SVC's output current to a Thevenin voltage behind a large resistance (documented in Appendix A). The Thevenin resistance is large to reduce the error it introduces.

5.2.4.1 SVC as a Reactive Power Compensator

Initially the SVC was configured only to compensate the wind turbine's reactive power (K_v=0). The voltage fluctuations due to a high wind shut-down of the wind turbine with the SVC (Figure 5.22) are similar to those with the capacitor bank (Figure 5.18) since the reactive power step seen by the network is zero in both cases. The voltage fluctuations due to a low wind cut-off are considerably lower with the SVC than with the capacitor bank, since the reactive power step always remains zero with the SVC.

The flicker emissions due to wind turbulence are greatly reduced by the SVC, since the SVC cancels the reactive power fluctuations produced by the wind turbine. Figure 5.23 demonstrates that the flicker has become negligible with the SVC operating as a reactive

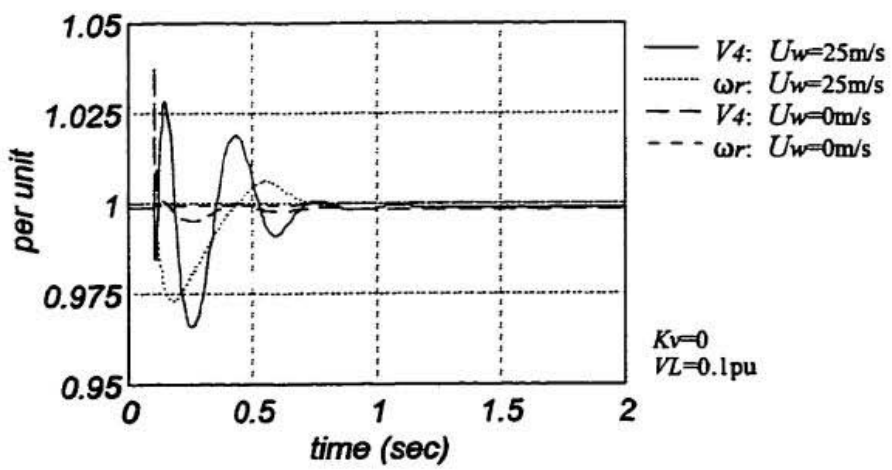

Figure 5.22 Wind turbine disconnect with SVC (K_v=0).

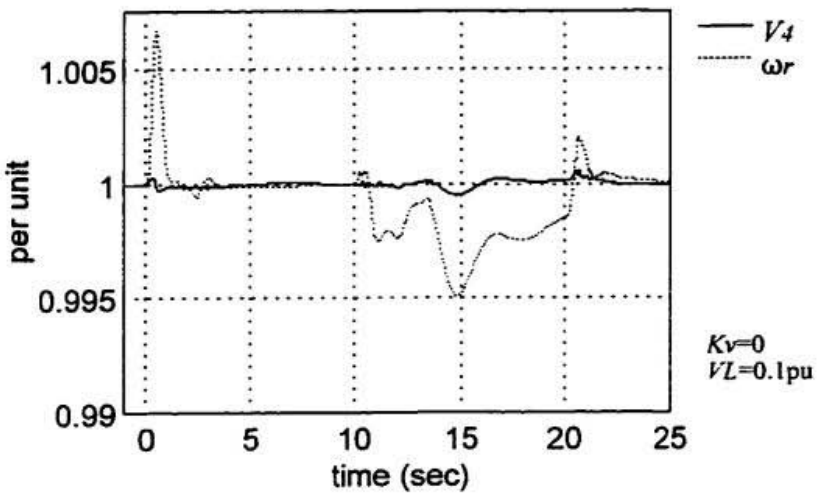

Figure 5.23 Flicker with SVC (K_v=0).

power compensator for the wind turbine.

5.2.4.2 SVC as a Reactive Power Compensator plus Voltage Stabilizer

With just a small amount of gain in the voltage control loop of the SVC (K_v=10) the voltage transients due to the disconnection of the wind turbine are significantly reduced. As Figure 5.24 illustrates, the SVC responds quickly to the sudden changes in network loading, thus dampening the response of the synchronous generator. The voltage feedback loop also improves the voltage stability of the system.

Figures 5.25 and 5.26 show the network voltages due to the test wind turbulence for K_v=0 and K_v=10, respectively. The high frequency oscillations in Figure 5.25 are the synchronous generator's response to rapid changes in the dump load power. These oscillations are greatly reduced in Figure 5.26 by the voltage control of the SVC. The flicker at the village junction (V_4) is slightly larger with SVC voltage control than without SVC

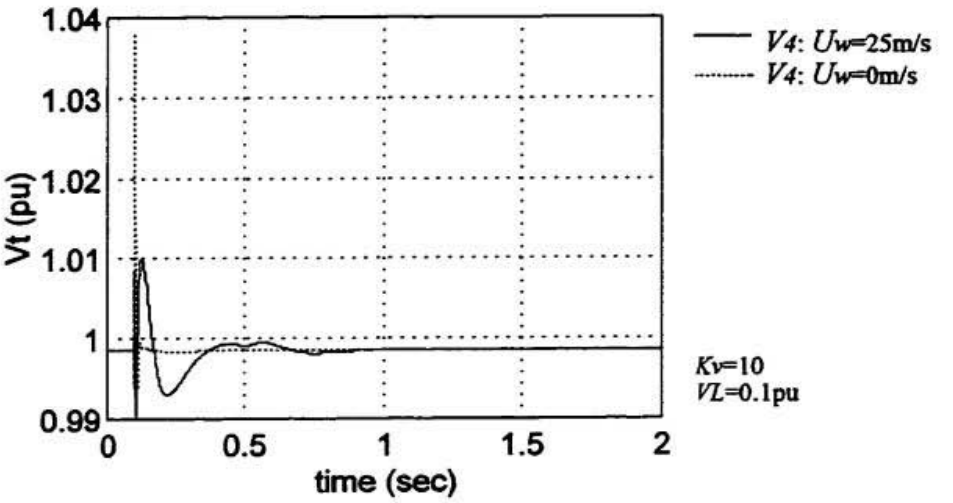

Figure 5.24 Wind turbine disconnect with SVC (K_v=10).

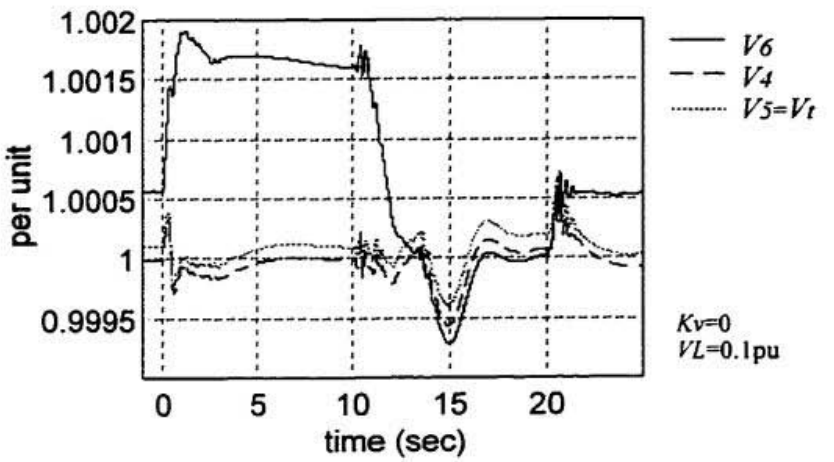

Figure 5.25 Network voltages with SVC (K_v=0).

voltage control since the SVC is attempting to regulate the voltage at the wind turbine (V_6)instead of the village junction (V_4).

Because of the fast response of the SVC with the voltage control loop, the flicker level due to wind turbulence and wind turbine disconnections should lie well within the IEC flicker limits. The voltage spikes caused by the delayed response of the dump load

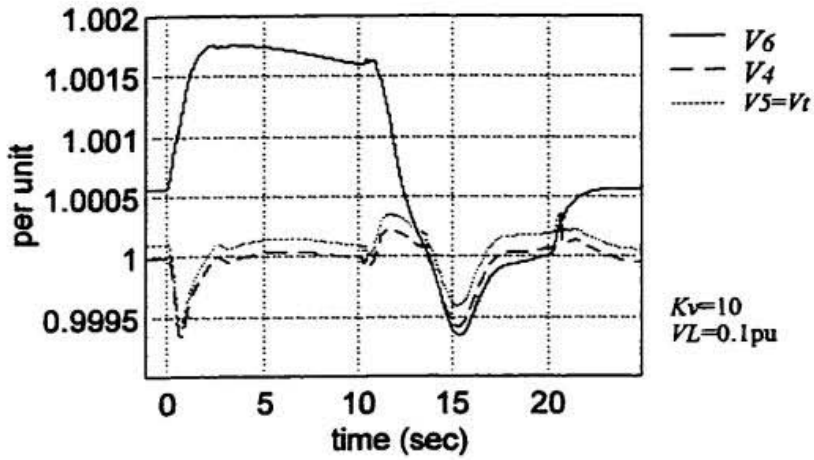

Figure 5.26 Network voltages with SVC (K_v=10).

immediately following the wind turbine's disconnection are also greatly reduced by the SVC with voltage control.

Chapter

6 Conclusions

6.1 Summary of Conclusions

Studies have shown that the integration of wind turbines into an autonomous diesel-electric system (i.e., wind-diesel) can be economically viable. The potential market for wind-diesel is considerable. There are approximately 170 remote communities in Canada where the wind resource is sufficient to make wind-diesel practicable. Worldwide, the existing diesel generating capacity in regions with good wind resources is estimated to be 15 GW, with a growth potential in excess of 26 GW.

Diesel generators have very poor efficiencies at low loads (e.g., no-load fuel consumption rates of 25-30% of full-load) and should not be operated for extended periods of time below a minimum loading level of approximately 30-40% of their rated output. Therefore, substantial fuel savings can only be achieved by shutting off the diesel generators for prolonged periods. Intermittent diesel operation can be realized with the addition of energy storage, or the implementation of high wind power penetration. Due to the high cost

and complexity of suitable storage devices, *high-penetration, no-storage wind-diesel* (HPNSWD) is considered to be more economical.

A HPNSWD system requires a fast-acting dump load controller to maintain the system frequency stability and quality, and, under some applications, additional voltage control is needed to maintain the voltage quality.

In this thesis a comprehensive nonlinear dynamic model of a HPNSWD system is presented. Unlike other wind-diesel models, this model includes both a detailed mechanical and a detailed electrical system. Significant factors of each system component are clearly identified and their implementation or omission is justified.

The model is based on the wind-diesel test-bed at the Atlantic Wind Test Site (AWTS) in PEI, Canada, and is implemented in MATLAB and SIMULINK. The numeric computation and visualization software package MATLAB and its associated dynamic system simulation software, SIMULINK, are broadly used in academia and industry. A complete list of the modelling parameters used in this thesis can be found in Appendix B.

Wherever possible, components of the model are validated with available measurements from the AWTS system. The validation of the wind turbine model is limited to the steady-state due to the lack of available characterization data.

A single diesel generator and wind turbine of similar size are found to be capable of representing all the significant dynamics of a HPNSWD system. Alternate machines can be modelled by adjusting the parameters and/or modifying the component models in SIMULINK. Additional machines and storage could be added to the model if required for future studies.

The dynamic model of the stall regulated wind turbine includes: spatial filtering to

convert a point windspeed to an effective windspeed; induction lag; quasi-steady power coefficient versus tip speed ratio; and torsion of the low speed shaft.

A torque fit equation and dead-time are incorporated in the naturally aspirated diesel engine model. The diesel generator model also includes a unidirectional coupling (clutch) between the engine and the synchronous generator. Both the commercial diesel governor and the commercial automatic voltage regulator are modelled in detail.

A wide variety of reduced-order electric machine models are used in wind-diesel modelling. While many of these reduced-order models may be valid for large machines on interconnected grids, care must be taken when applying them to a small autonomous system where the machines are smaller and the frequency less stable. In this study, the electric machines are modelled at the following levels to determine their effect on the overall model performance:

Synchronous Generator:

First-Order - one-axis voltage behind transient reactance model.

Second-Order - two-axis voltage behind transient reactance model, where the q-axis damper winding is treated as a transient circuit.

Third-Order - two-axis voltage behind subtransient reactance model.

Full-Order - fifth-order model which includes the stator transients and speed terms.

Induction Generator:

Second-Order - two-axis voltage behind transient reactance model.

Full-Order - fourth-order model which includes the stator transients and speed terms.

The algebraic portions of the electric machines and the electrical network are represented in a form that can be solved directly, therefore an iterative solution to the network voltages and currents (commonly found in other wind-diesel models) is avoided.

Simulations of the reduced-order models are compared with the simulations of the *full-order* models and the actual system measurements. The *first-order* model of the synchronous generator, commonly used in wind-diesel modelling, gives unfavourable results, except under the condition of slow electrical transients, i.e., >100 ms. The performance of the model is vastly improved by increasing the order of the synchronous generator model to a *second-order* system.

The effects of system frequency fluctuation (synchronous generator rotor speed transients) can be significant in an autonomous wind-diesel system. The *full-order* electric machine models are the only models that include these effects. Since the diesel generator's characterization measurements contain significant rotor speed transients, the *full-order* synchronous generator model is required to get a good match between the measured and simulated voltage responses. In cases where simulations using a reduced-order model result in marginal voltage performance and the corresponding frequency fluctuation is significant (say, greater than 0.02pu), the simulation should be repeated with the *full-order* model.

Under the condition of constant frequency, the differences between the *second-order*, *third-order* and *full-order* models are small and most likely less significant than the simulation errors due to inaccurate modelling parameters.

The addition of magnetic saturation in the electric machine models increases the damping of the voltage control system slightly, but the net effect is also likely less than the

simulation errors due to inaccurate modelling parameters. Magnetic saturation has a negligible effect during the subtransient period of the electric machine's response.

With the validity of the HPNSWD dynamic model established, the allowable frequency and voltage variation are discussed and the system's power quality is investigated.

The practical implementation of a dump/deferrable load to control the system frequency remote from the diesel generator is considered. Unlike most other wind-diesel models, the dump load controller operates independently of the diesel's governor and speed signals. This requires fast electrical frequency detection. Three different frequency transducers (one phase detector and two frequency detectors) are modelled and incorporated into the design of a PID dump load frequency controller. All three controller designs provide good frequency regulation. Comparing the phase detector with the frequency detector of the same speed (360 Hz pulse rate), the controller with the frequency detector has a superior performance since the integral action of the phase detector results in an effective 'PI' response from the PID controller.

The controller with the fast frequency detector (360 Hz pulse rate) effectively dampens the swing of the system against the wind turbine's rotor. The controller with the phase detector dampens this mode less effectively, but is still acceptable. The system employing the controller with the slow frequency detector (36 Hz pulse rate) is only lightly damped in this mode, and may not be acceptable due to the increased fatigue of the wind turbine.

Other HPNSWD studies have not investigated the response of the system to large disturbances. Rapid windspeed fluctuations and wind turbine disconnections at full output

power and no output power are used to simulate the large disturbances a HPNSWD system would normally see. Simulations of the voltage control of the synchronous generator indicate that the existing system is not able to adequately cope with these large disturbances.

Due to the large reactive power load steps, the voltage transients that result from the disconnection of the wind turbine are well above the specified limit. The addition of a capacitor bank at the wind turbine (switched on and off in conjunction with the wind turbine) reduces all but one of these voltage transients to an acceptable level. The wind-diesel system with the capacitor bank has an eight percent voltage dip upon a wind turbine high wind shut-down. This short duration (< 20 ms) voltage dip corresponds to a load spike caused by the delayed response of the dump load controller.

The susceptibility of the system to flicker emissions from wind turbulence are virtually the same with and without the capacitor bank. Wind conditions may exist that would cause the system to exceed the IEC flicker limits.

In this study a static VAR compensator (SVC) is uniquely applied to the wind-diesel system to improve its voltage stability. With the SVC configured to compensate the reactive power of the wind turbine, the wind turbine disconnections yield similar responses as with the capacitor bank, but the flicker emissions due to wind turbulence are virtually eliminated.

Adding a novel voltage control loop to the SVC reduces the voltage transients from the wind turbine disconnections to well within the specifications. In addition, the voltage stability of the entire system is improved.

6.2 Recommendations for Further Study

This thesis has not considered the susceptibility of the modelled frequency transducers to noise and waveform distortion, as may be present during the soft-start of the wind turbine. More detailed, per phase models of the frequency transducers, along with portions of the wind-diesel model presented here, could be used with simulated or recorded phase voltages to investigate the effects of noise and waveform distortion on the dump load controller. In addition, the per phase wind-diesel model documented in Appendix C could be modified to simulate the transients associated with the direct connection of the wind turbine, or extended to model its connection with a soft-start device.

The practical application of the dump/deferrable loads in a HPNSWD system may come in many different forms. The wind-diesel model can form the basis for studying alternative dump/deferrable loads such as: thyristor controlled resistive loads; induction motor loads (variable power or incrementally fixed) in the form of ice making, water desalination or water pumping; or any combination of these.

The frequency control strategy implemented in this study operates with droop regulation during diesel governing (diesel is in droop mode) and isochronous regulation during dump load governing. Many customers on well established autonomous diesel powered grids rely on electric clocks that derive their time from the grid frequency (such as some video cassette recorder models). Thus accurately set, isochronous diesel operation is desirable. For these applications, additional research is required to implement a load share control between the diesel and the dump load for the isochronous operation of the diesel. In

this implementation, an option is foreseen that would monitor and correct any cumulative error in the system frequency.

Only a single diesel generator and a single wind turbine have been modelled in this thesis. The model can be expanded to include more machines and/or a storage device, such as a flywheel, for further or more specific studies.

During *wind-only* operation of the HPNSWD system, the supervisory controller, which is not covered in this thesis, must closely monitor the wind turbine and village powers to anticipate a power shortfall and start the diesel engine ahead of time to prevent a system frequency collapse. In addition, the supervisory controller should maximize the diesel's off time while minimizing the diesel's start-stop cycling. Although the start-stop cycling versus storage capacity of a wind-diesel system with storage has been studied [3,10,20], the author recommends further research specifically on optimal HPNSWD supervisory control algorithms.

A reduced-order linear model of the wind-diesel model presented in this thesis could be determined using MATLAB tools. This reduced-order model is then used to simulate the system's response to longer-term data, and to develop and analyse supervisory control algorithms. The author envisions a self-tuning supervisory controller which can optimize its performance for the specific conditions of the installation site. MATLAB and SIMULINK are well suited for this task since they offer substantial resources for controller design, especially fuzzy logic and neural networks–which are likely candidates for this application.

References

[1] R.S. Rangi, and R.J. Templin, "Canadian Wind Energy Technical and Market Potential", Workshop Report, *Fifth International AWEA/CanWEA Wind-Diesel Hybrid Power Workshop*, White River Junction, Vermont, USA, June 1991, 9 p.

[2] W.R. King, and B.L. Johnson, "Worldwide Wind/Diesel Study: Potential Applications and Technical Issues", *AWEA Windpower '90 Proceedings*, Washington, DC, USA, September 1990, pp. 233-240.

[3] N.H. Lipman, and D.G. Infield, "Wind-diesel systems", in *Wind Energy Conversion Systems*, ed. L.L. Freris, Prentice Hall International (UK) Ltd, Hertfordshire, UK, 1990, pp. 330-356.

[4] R. Reid, B. Saulnier, and D. Champagne, "An Economic Evaluation for a 800kW Northern Quebec High Penetration No Storage Wind-Diesel System", Workshop Report, *Eighth International CanWEA/AWEA Wind-Diesel Workshop*, Charlottetown, PEI, Canada, June 1994, pp. 134-143.

[5] R. Reid, J.P. Laflamme, "Case Study: High Penetration No Storage Wind-Diesel System for Inukjuak, Northern Quebec", Workshop Report, *Ninth International CanWEA/AWEA Wind-Diesel Workshop*, Hanover, New Hampshire, USA, June 1995, 30 p.

[6] D. Harris, "Newfoundland & Labrador Hydro's Rural Isolated Systems: Opportunities and Obstacles to Wind-Diesel Integration", Workshop Report, *Eighth International CanWEA/AWEA Wind-Diesel Workshop*, Charlottetown, PEI, Canada, June 1994, pp. 19-27.

[7] P. Gipe, *Wind Energy Comes of Age*, John Wiley & Sons, Inc., New York, NY, USA, 1995, 536 p.

[8] R. Reid, and B. Saulnier, "Wind/Diesel Potential for Remote Power Systems: Technico-Economic Aspects", *Proceedings of the Canadian Wind Energy Conference '86*, Québec City, Québec, Canada, October 1986, pp. 329-366.

[9] "Renewables part of Kyoto protocol", *Windpower Monthly News Magazine*, Vol. 14, No. 1, January 1998, pp. 23-24.

[10] R. Hunter (editor), and G. Elliot (editor), *Wind-Diesel Systems, A guide to the technology and its implementation*, Cambridge University Press, Cambridge, UK, 1994, 249 p.

[11] J.L. Sulley, and N.L. Holding, "Optimum Economic Penetration of Aerogenerators into Small Island Systems", *Fourth International Conference on Energy Options, The Role of Alternatives in the World Energy Scene*, London, UK, April 1984, pp. 134-137.

[12] P. Caselitz, G. Hackenberg, and W. Kleinkauf, "Short-Time Behaviour of Diesel-Generators When Integrated With Wind Energy Converters", *Proceedings of the European Wind Energy Conference 1984*, Hamburg, FRG, October 1984, pp. 674-680.

[13] D.G. Infield, G.W. Slack, N.H. Lipman, and P.J. Musgrove, "Review of Wind/Diesel Strategies", *IEE Proceedings*, Vol. 130, Pt. A, No.9, December 1983, pp. 613-619.

[14] U. Hassan, and D.M. Sykes, "Wind structure and statistics", in *Wind Energy Conversion Systems*, ed. L.L. Freris, Prentice Hall International (UK) Ltd, Hertfordshire, UK, 1990, pp. 11-32.

[15] E. Welfonder, R. Neifer, and M. Spanner, "Development and Experimental Identification of Dynamic Models for Wind Turbines", *Control Engineering Practice*, Vol. 5, No. 1, 1997, pp. 63-73.

[16] D.J. Hammerstrom, and L.A. Schienbein, "Addition of a Controlled Static Converter to a High Penetration, No Storage Wind-Diesel System", *Wind Engineering*, Vol. 20, No. 5, 1996, pp. 333-348.

[17] *MATLAB High-Performance Numeric Computation and Visualization Software - User's Guide*, The Math Works, Inc., Natick, MA, USA, 1992, 223 p.

[18] *SIMULINK Dynamic System Simulation Software - User's Guide*, The Math Works, Inc., Natick, MA, USA, 1992, 271 p.

[19] D.G. Infield, P. Lundsager, J.T.G. Pierik, V.A.P. van Dijk, M. Falchetta, Ø. Skarstein, and P.D. Lund, "Wind/Diesel System Modelling and Design", *Proceedings of the European Community Wind Energy Conference 1990*, Madrid, Spain, September 1990, pp. 569-574.

[20] Ø. Skarstien, and K. Uhlen, "Design Considerations With Respect to Long-Term Diesel Savings in Wind/Diesel Plants", *BWEA/EWEA/IEE Workshop on Wind-Diesel Systems*, Didcot, UK, May 1989, 30 p.

[21] M.E. Jones, "The Development of a Quasi Steady State Wind/Diesel Model for Multiple Non-Identical Wind Turbines and Diesels", *Wind Engineering*, Vol. 17, No.1, 1993, pp. 35-57.

[22] A.R. McFarlane, P.S. Veers, and L.L. Schluter, " Simulating High Frequency Wind for Long Durations", *Wind Energy - 1994: ASME Energy-Sources Technology Conference*, New Orleans, USA, January 1994, pp. 175-180.

[23] J.F. Manwell, J.G. McGowan, E.I. Baring-Gould, W. Jeffries, and W. Stein, "Hybrid Systems Modeling: Development and Validation", *Wind Engineering*, Vol. 18, No.5, 1994, pp. 241-256.

[24] J. Green, "HYBRID2 - A Versatile Model of Hybrid Power Systems", Workshop Report. *Tenth Annual International CanWEA/AWEA Wind-Diesel Workshop*, Halifax, Nova Scotia, Canada, June 1996, Section 18, 7 p.

[25] P. Lundsager, P.H. Madsen, and H.A. Madsen, "Theoretical and Experimental Results from the Operation of RISØ's Experimental Wind/Diesel System", *Proceedings of the European Community Wind Energy Conference and Exhibition 1986*, Rome, Italy, October 1986, F19, 7 p.

[26] P. Lundsager, H. Bindner, D. Infield, A. Scotney, K. Uhlen, T. Troftevaag, J. Pierik, and M. Falchetta, "The JODYMOD Dynamic Wind Diesel Simulation Program Part 1: Description of the Model and its Validation", *BWEA/SERC Workshop on Wind Energy Penetration into Weak Electricity Networks*, UK, June 1993, pp. 133-149.

[27] H. Bindner, "The JODYMOD Dynamic Wind/Diesel Simulation Program Part 2: Presentation of the Program. Demonstration and Examples", *BWEA/SERC Workshop on Wind Energy Penetration into Weak Electricity Networks*, UK, June 1993, pp. 150-160.

[28] K. Uglen, and Ø. Skarstein, "A Short Term Dynamic Simulation Model for Wind/Diesel Systems", *Wind Energy Conversion 1988: Proceedings of the 10th British Wind Energy Association Conference*, London, UK, 1988, pp. 235-242.

[29] K. Uhlen, T. Toftevaag, Ø. Skarstein, and B. Foss, "Model Validation and Voltage Control of Wind/Diesel Systems", *Fifth International Wind-Diesel Hybrid Power Workshop*, Vermont, USA, June 1991, 15 p.

[30] J.T.G Pierik, and L.A. Bulten, "Technical Feasibility Study of the Holec Autonomous Wind-Diesel System", *Proceedings of the European Community Wind Energy Conference 1990*, Bedford, UK, September 1990, pp. 683-687.

[31] J.T.G. Pierik, "Short term dynamics of AWIDIMOD compared to measurements", *BWEA/RAL workshop on: Wind Energy Penetration into Weak Electrical Networks*, Abingdon, UK, June 1993, pp. 161-171.

[32] A.J. Tsitsovits, and L.L. Freris, "Dynamics of an isolated power system supplied from diesel and wind", *IEE Proceedings*, Vol. 130, Pt. A, No. 9, December 1983, pp. 587-595.

[33] W.Q. Jeffries, "Analysis and Modeling of Wind/Diesel Systems Without Storage", *Ph.D. Thesis*, University of Massachusetts, Amherst, MA, USA, September 1994, 274 p.

[34] G.S. Stavrakakis, and G.N. Kariniotakis, "A General Simulation Algorithm for the Accurate Assessment of Isolated Diesel-Wind Turbines Systems Interaction", *IEEE Transactions on Energy Conversion*, Vol. 10, No. 3, September 1995, pp. 577-590.

[35] G. Kariniotakis, G. Stavrakakis, E. Nogaret, and M. Bordier, "Advanced Modelling and Identification of Autonomous Wind-Diesel Power Systems. Application on the French Island Desirade", *Proceedings of the European Community Wind Energy Conference 1993*, Lübeck-Travemünde, Germany, March 1993, pp. 347-350.

[36] I. Kamwa, "Dynamic Modelling and Robust Regulation of a No-Storage Wind-Diesel Hybrid Power System", *Electric Power Systems Research*, Vol. 18, 1990, pp. 219-233.

[37] Y. Jean, D. Champagne, R. Reid, and B. Saulnier, "Dynamic Model of a High Penetration No-Storage Wind/Diesel Scenario", *Canadian Wind Energy Conference '91*, Montréal, Québec, Canada, November 1991, pp. 587-604.

[38] Power Automation, Inc, "Electromagnetic Transients Program (EMTP) Revised: Rule Book Version 2.0, Volume 1: Main Program", *EL-6421-L*, Electric Power Research Institute, Palo Alto, CA, USA, June 1989.

[39] B. Saulnier, R. Reid, and D. Champagne, "Remote Northern Community Applications & Hydro-Québec/AWTS Collaboration", Workshop Report, *Eighth International CanWEA/AWEA Wind-Diesel Workshop*, Charlottetown, PEI, Canada, June 1994, pp. 94-108.

[40] S.D. Haddad, and N. Watson, *Principles and Performance in Diesel Engineering*, Ellis Horwood Ltd., Chichester, UK, 1984, 280 p.

[41] S. Roy, O.P. Malik, and G.S. Hope, "An Adaptive Control Scheme for Speed Control of Diesel Driven Power-Plants", *IEEE Transactions on Energy Conversion*, Vol. 6,

No. 4, December 1991, pp. 605-611.

[42] K.E. Yeager, and J.R. Willis, "Modeling of Emergency Diesel Generators in an 800 Megawatt Nuclear Power Plant", *IEEE Transactions on Energy Conversion*, Vol. 8, No. 3, September 1993, pp. 433-441.

[43] E.N. Hinrichsen, and P.J. Nolan, "Dynamics and stability of wind turbine generators", *IEEE Transactions on Power Apparatus and Systems*, Vol. PAS-101, No. 8, August 1982, pp. 2640-2648.

[44] Y. Jean, A. Noaelli, P. Viarouge, D. Champagne, R. Reid, and B. Saulnier, "Jumelage Éolien Diesel IREQ: Analyse des Essais 1992 Validation du Modèle Dynamique", *Report No. IREQ-93-103C*, L'Institute de Recherche de l'Hydro-Québec, Varennes, Québec, Canada, 1993.

[45] D.J. Sharpe, "Wind turbine aerodynamics",in *Wind Energy Conversion Systems*, ed. L.L. Freris, Prentice Hall International (UK) Ltd, Hertfordshire, UK, 1990, pp. 54-118.

[46] O. Wasynczuk, D.T. Man, and J.P. Sullivan, "Dynamic Behavior of a Class of Wind Turbine Generators During Random Wind Fluctuations", *IEEE Transactions on Power Apparatus and Systems*, Vol. PAS-100, No. 6, June 1981, pp. 2837-2845.

[47] P.M. Anderson, and A. Bose, "Stability Simulation of Wind Turbine Systems", *IEEE Transactions on Power Apparatus and Systems*, Vol. PAS-102, No. 12, December 1983, pp. 3791-3795.

[48] W.A.A.M. Bierbooms, "A Dynamic Model of a Flexible Rotor Including Unsteady Aerodynamics", *Third IEA Symposium on the Aerodynamics of Wind Turbines*, Harwell, UK, 1990, 22 p.

[49] J. Wilkie, W.E. Leithead, and C. Anderson, "Modelling of Wind Turbines by Simple Models", *Wind Engineering*, Vol. 14, No.4, 1990, pp. 247-274.

[50] W.E. Leithead, S.A. de la Salle, and D. Reardon, "Classical control of active pitch regulation of constant speed horizontal axis wind turbines", *International Journal of Control*, Vol. 55, No.4, 1992, pp. 845-876.

[51] S. Øye, "Unsteady Wake effects caused by pitch-angle changes", *IEA Symposium - Joint Action on Aerodynamics of Wind Turbines*, London, UK, 1986, 17 p.

[52] M.T. Iqbal, A.H. Coonick, and L.L. Freris, "Some control aspects of a small isolated wind turbine", *Proceedings of the 15th British Wind Energy Association Conference*,

York, UK, October 1993, pp. 321-325.

[53] G. Gross, and M.C. Hall, "Synchronous machine and torsional dynamics simulation in the computation of electromagnetic transients", *IEEE Transactions on Power Apparatus and Systems*, Vol. PAS-97, No. 4, July/August 1978, pp. 1074-1086.

[54] R. Chedid, N. LaWhite, and M. Ilic, "A Comparative Analysis of Dynamic Models for Performance Calculation of Grid-Connected Wind Turbine Generators", *Wind Engineering*, Vol. 17, No.4, 1993, pp. 168-182.

[55] A.L. Coonick, "Dynamic Aspects of a Wind/Diesel System with Flywheel Energy Storage", *Ph.D. Thesis*, University of London, London, UK, January 1991.

[56] P.L. Dandeno, R.L. Hauth, and R.P. Schulz, "Effects of Synchronous Machine Modeling in Large Scale System Studies", *IEEE Transactions on Power Apparatus and Systems*, Vol. PAS-92, 1973, pp. 574-582.

[57] P.C. Krause, *Analysis of Electric Machinery*, McGraw-Hill, Inc., New York, NY, USA, 1986, 564 p.

[58] P. Kundur, *Power System Stability and Control*, McGraw Hill, Inc., New York, NY, USA, 1994, 1176 p.

[59] P. Anderson, and A. Fouad, *Power System Control and Stability*, Revised Printing, IEEE Press, New York, NY, USA, 1994, 464 p.

[60] R.H. Park, "Two-Reaction Theory of Synchronous Machines - Generalized Method of Analysis - Part I", *AIEE Transactions*, Vol. 48, July 1929, pp. 716-727.

[61] P.C. Krause, F. Nozari, T.L. Skvarenina, and D.W. Olive, "The Theory of Neglecting Stator Transients", *Transactions on Power Apparatus and Systems*, Vol. PAS-98, No. 1, January/February 1979, pp.141-148.

[62] A. Windhom, Kato Engineering, MN, USA, personal communication on KCR-360 modelling, February 1997.

[63] IEEE Standard 421.5-1992, "IEEE Recommended Practice for Excitation System Models for Power System Stability Studies", August 1992.

[64] Ontario Hydro, "Extended Transient-Midterm Stability Program (ETMSP): Version 3.1, Volume 2: User's Manual (Revision 1)", *EPRI TR-102004-V2R1*, Electric Power Research Institute, Palo Alto, CA, USA, 1994.

[65] C.E. Tindall, J.P. Martin, D.J. Morrow, and P.A.J. Calvert, "Transient Characteristics of Small Salient-Pole Alternators", *Transactions on Energy Conversion*, Vol. 11, No. 3, September 1996, pp. 539-546.

[66] S.S. Choi, and R. Larkin, "Performance of an autonomous diesel-wind turbine power system", *Electric Power Systems Research*, Vol. 33, 1995, pp. 87-99.

[67] M. Steinbuch, and F. Meiring, "Simulation and Analysis of a Wind Turbine with Variable Speed", *AFME International Workshop on the Dynamic Behaviour of Wind Turbines*, Valbonne, France, April 1986, 8 p.

[68] Northeast Power Coordinating Council, "Effects of synchronous machine modeling in large-scale system studies", *Final Report, NPCC-10, Task Force on System Studies, System Dynamic Simulation Techniques Working Group*, 1971.

[69] D. Levy, Westinghouse Canada Inc., Nova Scotia, Canada, personal communications regarding AOC wind turbine induction generator parameters, March 1997.

[70] L.L.J. Mahon, *Diesel Generator Handbook*, Butterworth-Heinemann Ltd., Oxford, U.K., 1992, 646 p.

[71] *CSA Standard C22.2 No. 1-94, Audio, Video, and Similar Electronic Equipment*, Canadian Standards Association, Toronto, Ontario, Canada, August 1994.

[72] *CSA Standard CAN/CSA-C22.2 No. 601.1-M90, Medical Electrical Equipment, Part 1: General Requirements for Safety*, Canadian Standards Association, Toronto, Ontario, Canada, November 1990, 232 p.

[73] *CSA Standard CAN3-C17-M84, Alternating-Current Electricity Metering*, Canadian Standards Association, Toronto, Ontario, Canada, August 1984, 126 p.

[74] *CSA Standard CAN/CSA-C282-M89, Emergency Electrical Power Supply for Buildings*, Canadian Standards Association, Toronto, Ontario, Canada, May 1989, 30 p.

[75] Y. Jean, D. Champagne, R. Reid, and B. Saulnier, "Methodology for the implementation of a high penetration wind diesel hybrid power system", *Sixth AWEA/CanWEA International Wind Diesel Workshop*, Mill River, PEI, Canada, June 1992, 20 p.

[76] A. Consoli, F. D'Antonio, A. Raciti, U. Nocera, A. Virgili, and A. Leotta, "Microcontroller Regulation of the Dump Load in a Hybrid Generation System", *29th Universities Power Engineering Conference*, Galway, Ireland, September 1994, pp.

820-823.

[77] R.E. Best, *Phase-Locked Loops. Theory, Design. and Applications*. Second Edition. McGraw-Hill, Inc.. New York, NY. USA. 1993. 373 p.

[78] R.C.A. Cullen. L.L. Freris, A.J. Ruddell, and J.A.M. Bleijis. "An innovative dynamic controller for a wind-diesel system". *Proceedings of the 16th British Wind Energy Association Conference*. Sterling, UK. June 1994. pp. 117-122.

[79] *Electrical Transducers and Monitoring Equipment. Catalog number 292*. Ohio Semitronics. Inc.. Columbus. Ohio. USA. 1997.

[80] *National Application Specific Analog Products Databook*. 1995 Edition. National Semiconductor Corp.. Arlington. TX. USA. 1995.

[81] K. Ogata. *Modern Control Engineering*, Third Edition. Prentice-Hall. Inc.. Upper Saddle River. NJ. USA. 1997. 997 p.

[82] *CSA Standard CAN3-C235-83. Preferred Voltage Levels for AC Systems. 0 to 50.000V*. Canadian Standards Association. Toronto. Ontario. Canada. September 1983. 11 p.

[83] T.J.E. Miller. *Reactive Power Control in Electric Systems*. John Wiley & Sons. Inc.. New York. NY. USA. 1982. 381p.

[84] T. Thiringer. "Power Quality Measurements Performed on a Low-Voltage Grid Equipped with Two Wind Turbines", *IEEE Transactions on Energy Conversion*. Vol. 11. No. 3. September 1996. pp. 601-606.

[85] C. Brothers. J. Rong, and W. Moll. "The Effects of Wind Turbines on Voltage Fluctuations on Radial Feeders - A Field Study". *Proceeding of the Tenth Annual National Conference of the Canadian Wind Energy Association (CanWEA '94)*. 1994.

[86] P. Sørensen. J.O. Tande. L.M. Søndergaard. and J.D. Kledal. "Flicker Emission Levels from Wind Turbines". *Wind Engineering*, Vol. 20. No. 1. 1996. pp. 39-46.

[87] H. Akagi, Y. Kanazawa, and A. Nabae, "Instantaneous Reactive Power Compensators Comprising Switching Devices without Energy Storage Components". *IEEE Transactions on Industry Applications*. Vol. IA-20. No. 3. May/June 1984. pp. 625-630.

[88] C. Schauder. and H. Mehta. "Vector analysis and control of advanced static VAR compensators". *IEE Proceedings-C*, Vol. 140. No. 4. July 1993. pp. 299-306.

Appendix A

SIMULINK Models

A.1 HPNSWD System Model

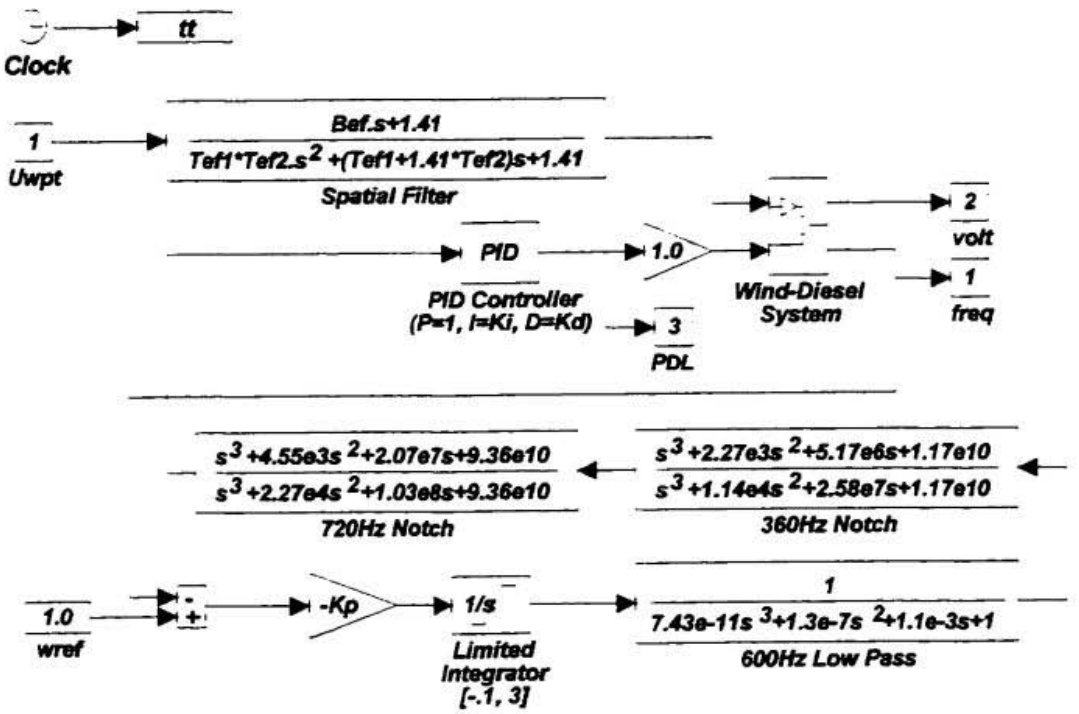

Figure A.1 HPNSWD system with phase detector dump load control.

A.1.1 Wind-Diesel Subsystem - Reduced-Order Model

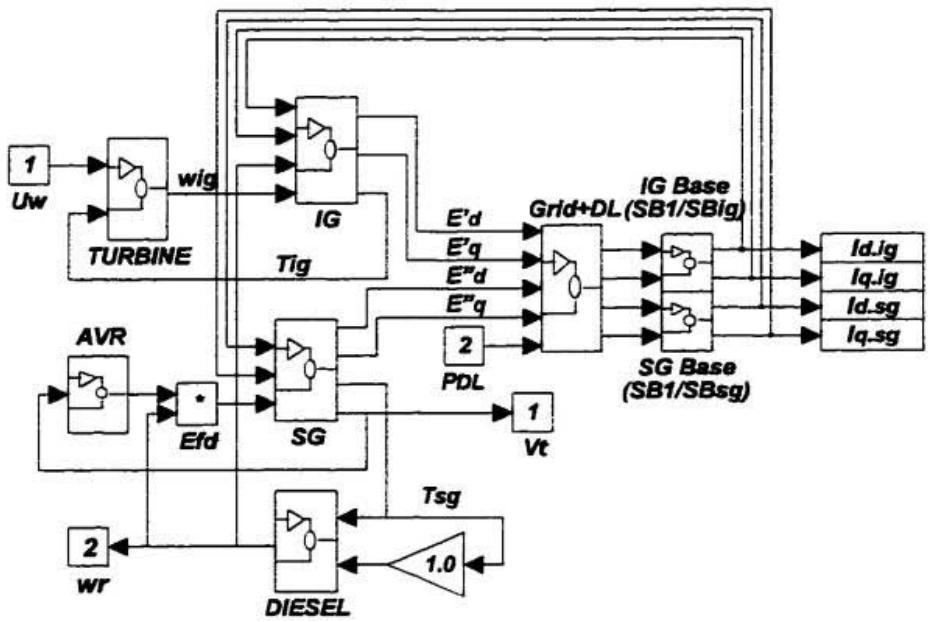

Figure A.2 Reduced-order wind-diesel subsystem model.

A.1.1.1 *Grid+DL* Subsystem for the Reduced-Order Wind-Diesel Model

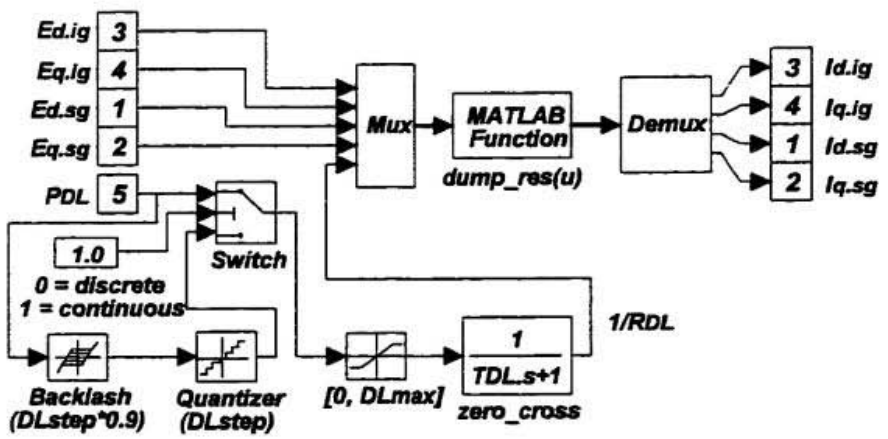

Figure A.3 Network admittance model.

A.1.1.2 *SG* Subsystems for the Reduced-Order Wind-Diesel Model

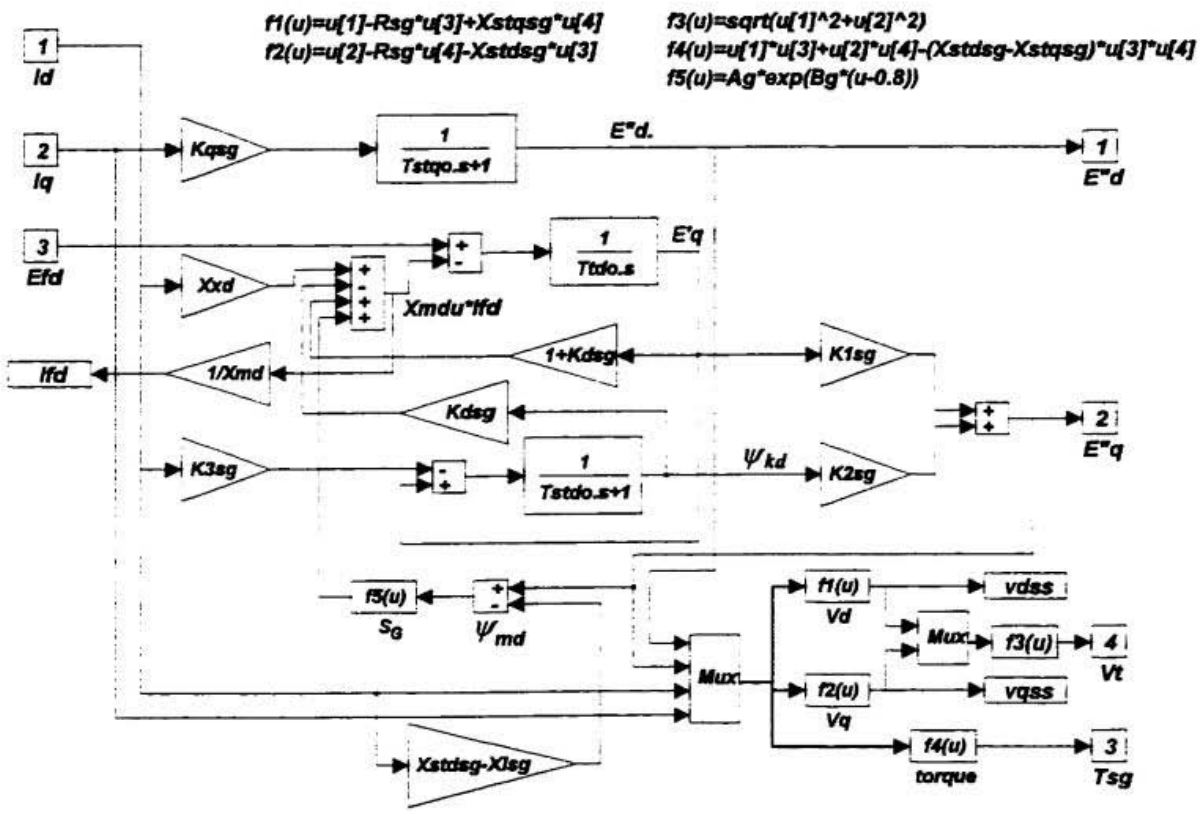

Figure A.4 SG3: 3rd-order synchronous generator model.

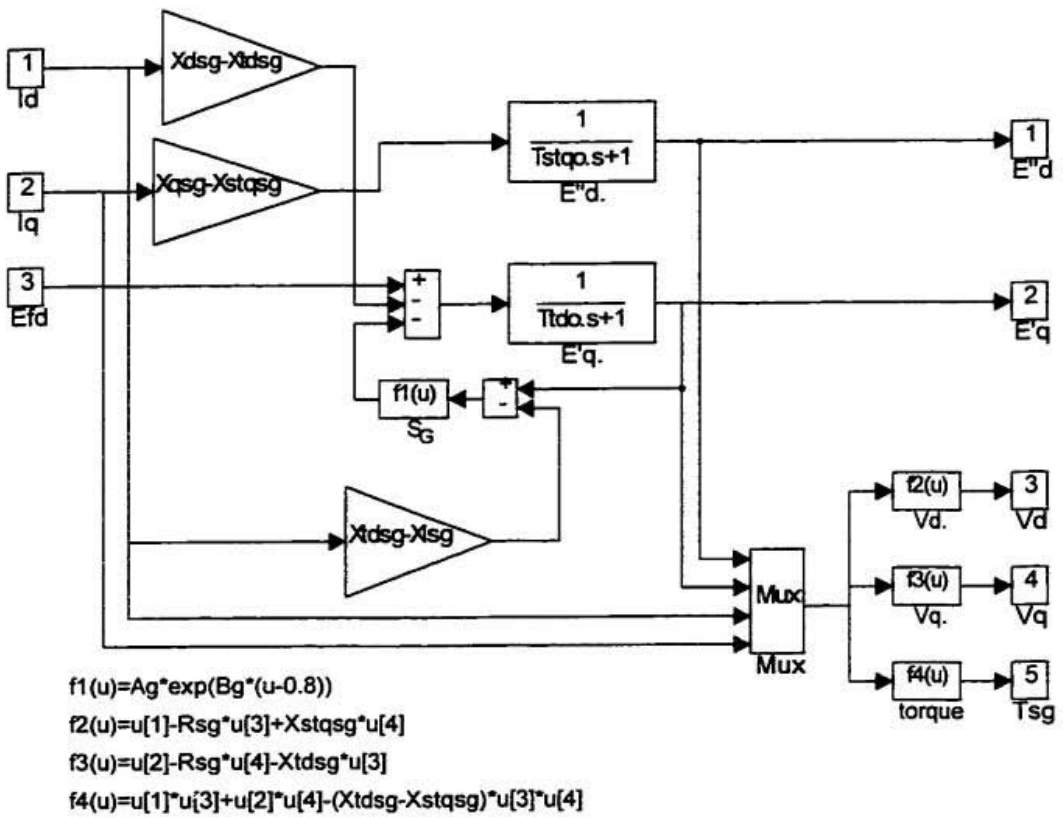

Figure A.5 SG2: 2nd-order synchronous generator model.

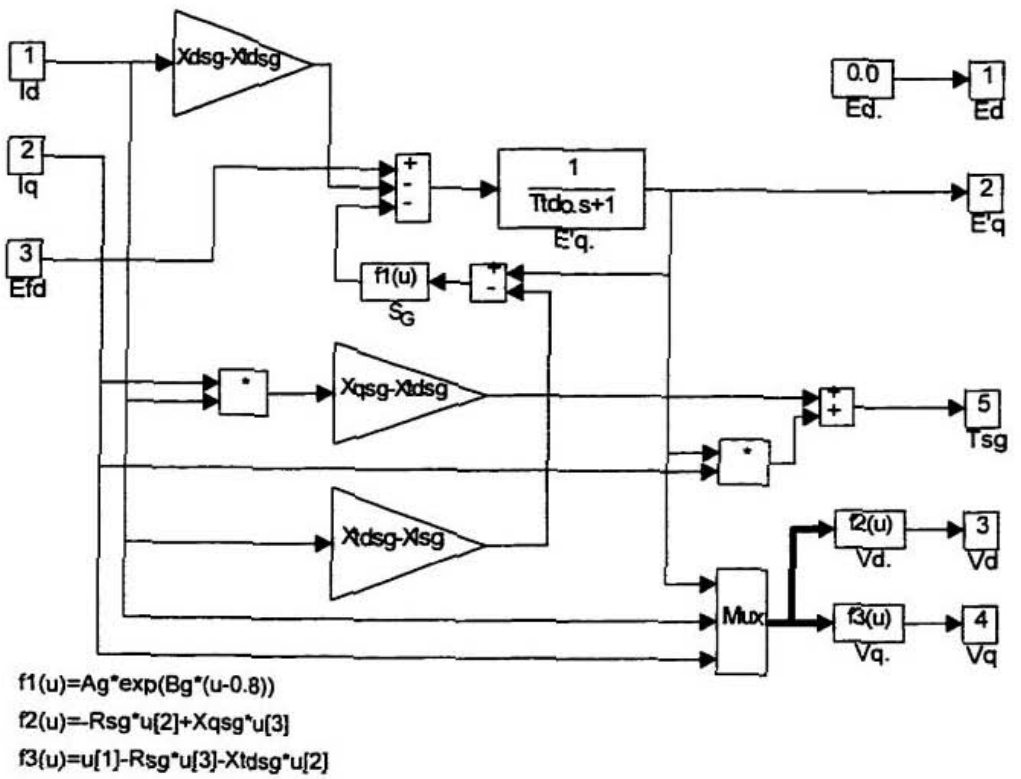

Figure A.6 SG1: 1st-order synchronous generator model.

A.1.1.3 *IG* Subsystem for the Reduced-Order Wind-Diesel Model

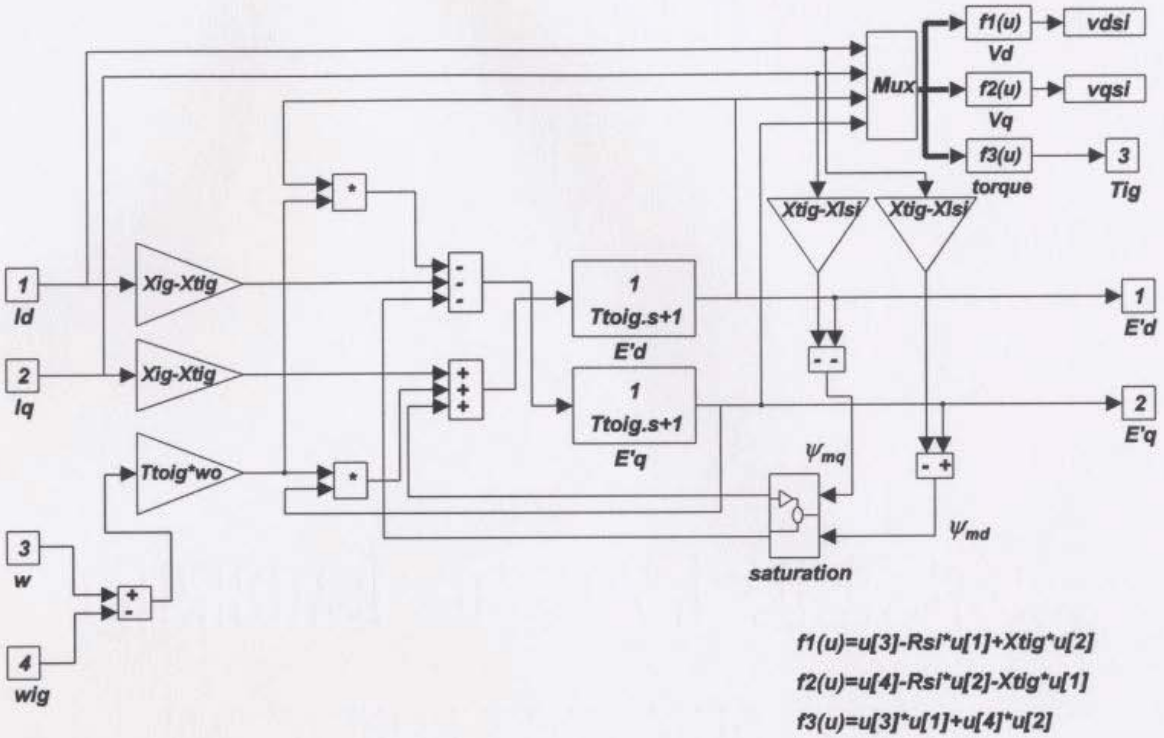

Figure A.7(a) IG2: 2nd-order induction generator model.

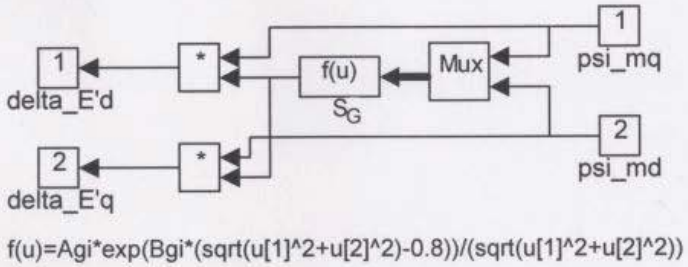

Figure A.7(b) *Saturation* subsystem of IG2 model.

A.1.2 Wind-Diesel Subsystem - Full-Order Model

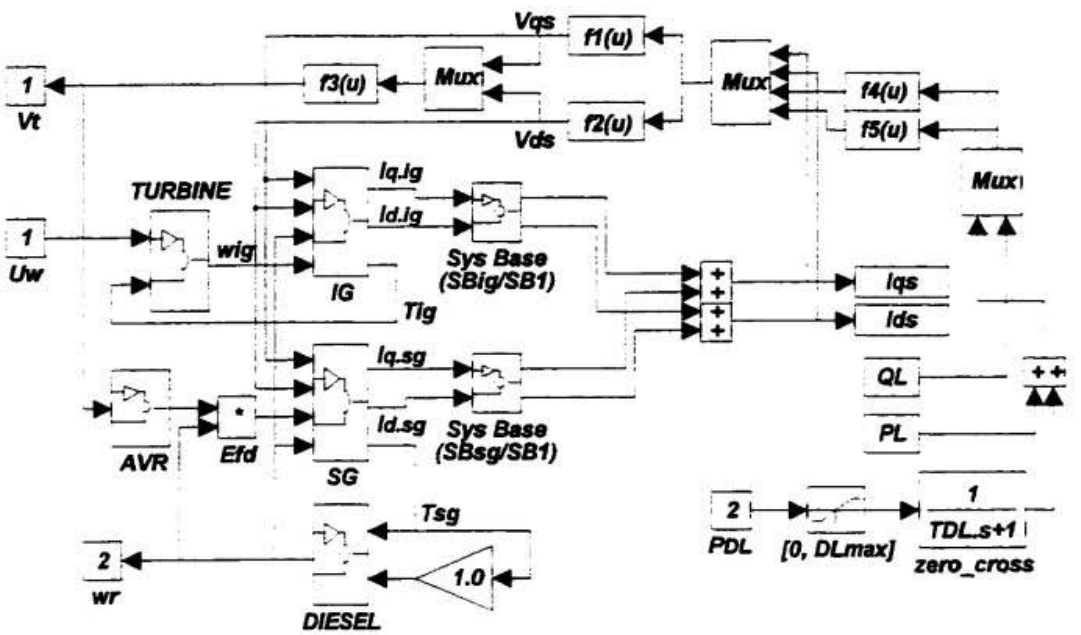

Figure A.8 Full-order wind-diesel subsystem model.

A.1.2.1 *SG* Subsystem for the Full-Order Wind-Diesel Model

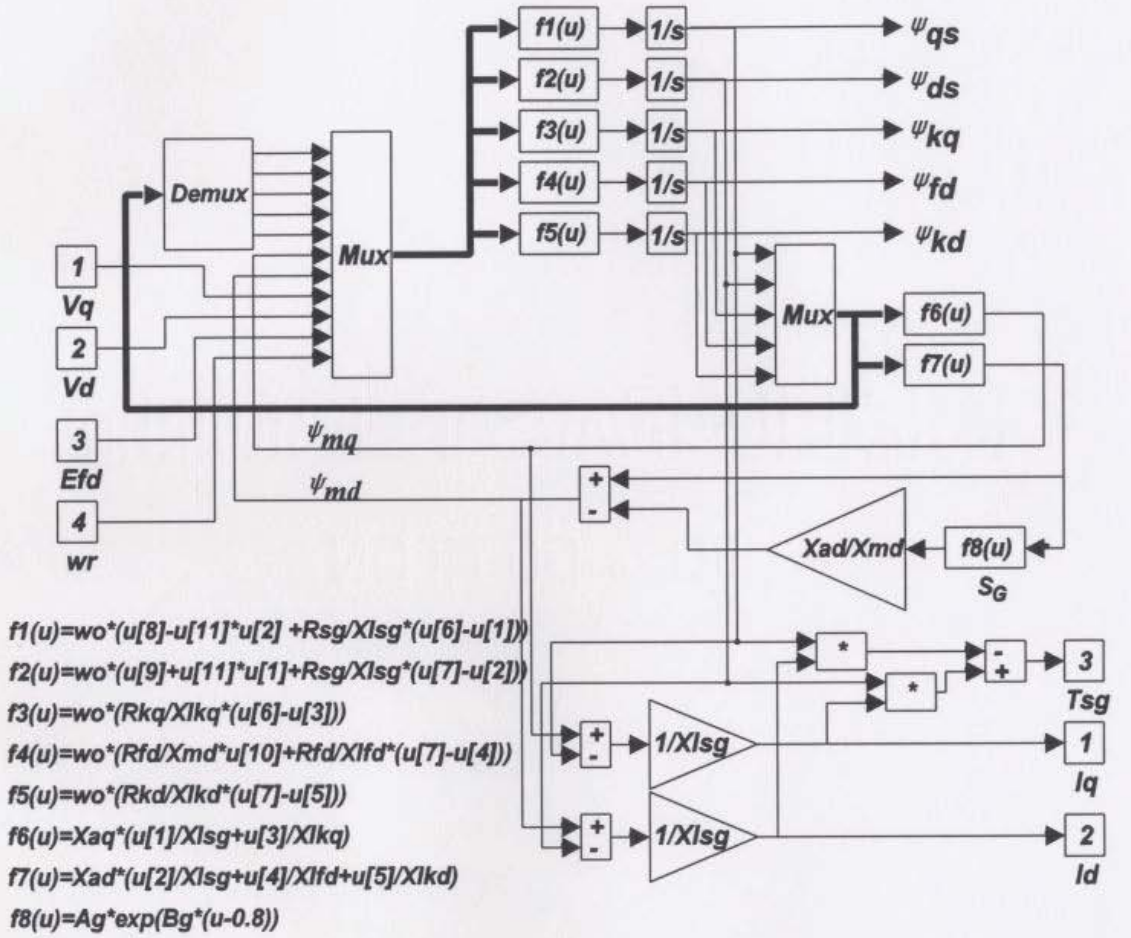

Figure A.9 SG5: full-order synchronous generator model.

A.1.2.2 *IG* Subsystem for the Full-Order Wind-Diesel Model

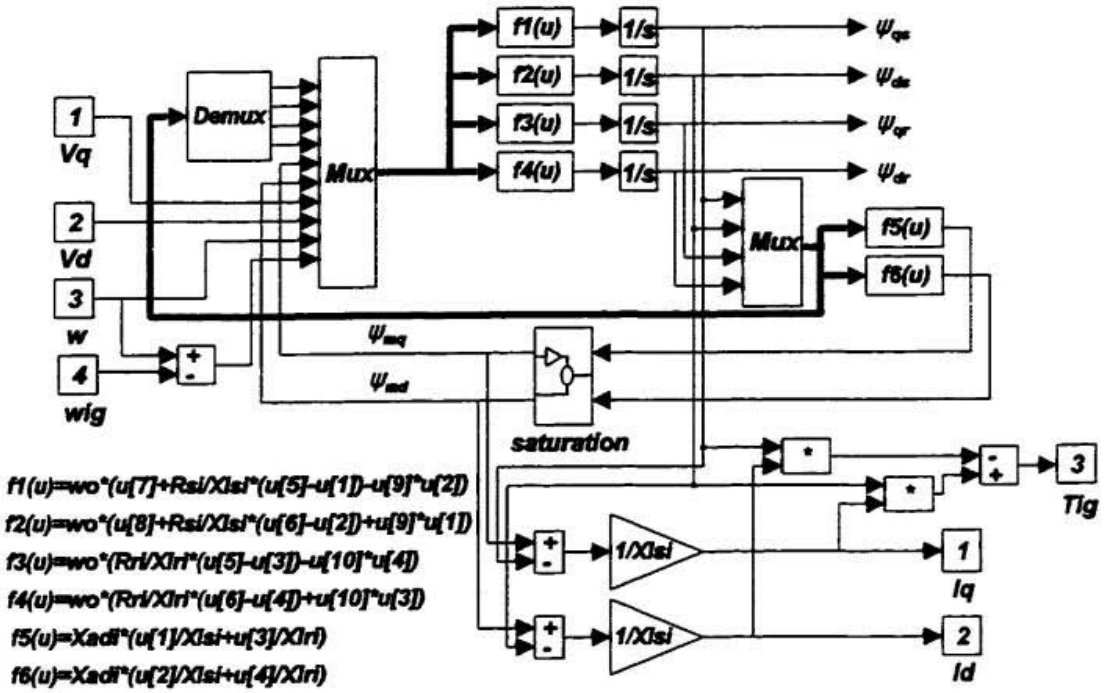

Figure A.10(a) IG4: full-order induction generator model.

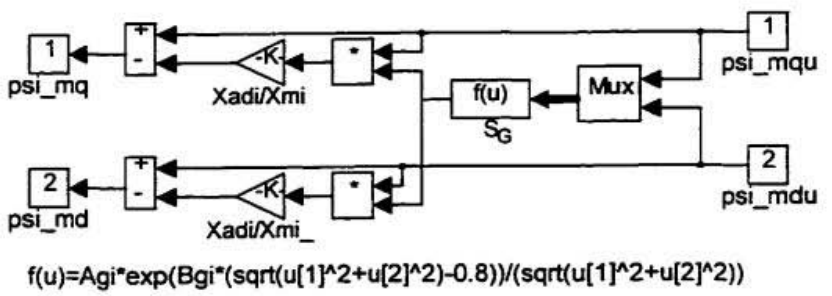

Figure A.10(b) *Saturation* subsystem of IG4 model.

A.1.3 Subsystems Common to the Wind-Diesel Models

A.1.3.1 *DIESEL* Subsystem for the Wind-Diesel Models

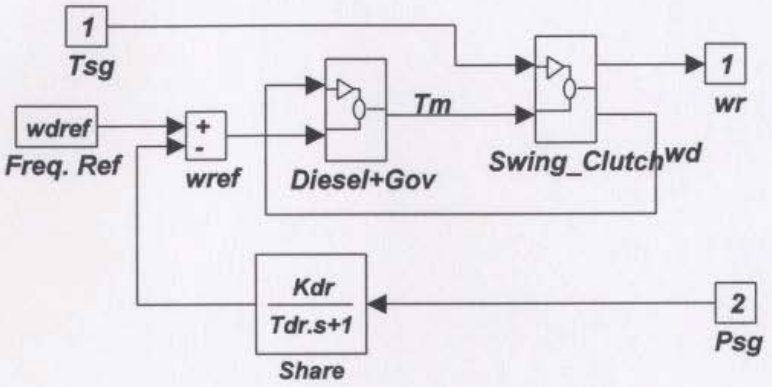

Figure A.11(a) Diesel generator mechanical model.

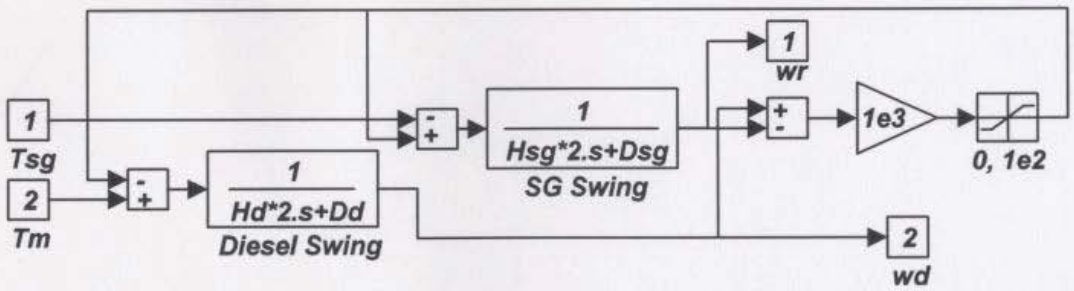

Figure A.11(b) *Swing_Clutch* subsystem of diesel generator model.

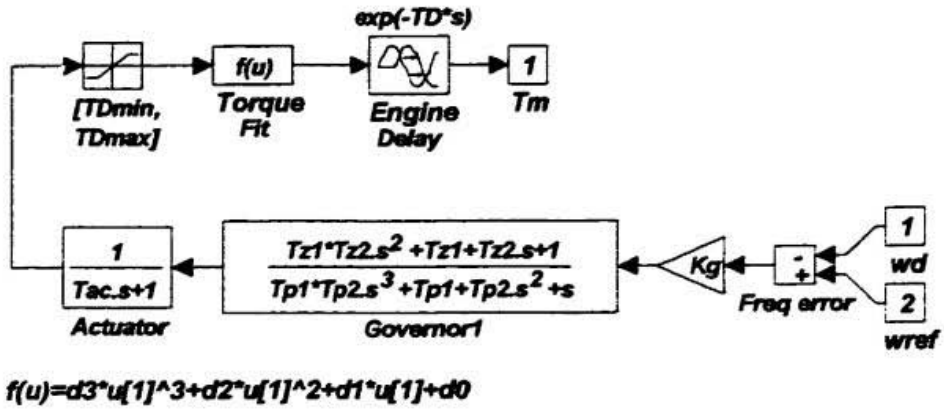

Figure A.11(c) *Diesel+Gov* **subsystem of diesel generator model.**

A.1.3.2 *TURBINE* Subsystem for the Wind-Diesel Models

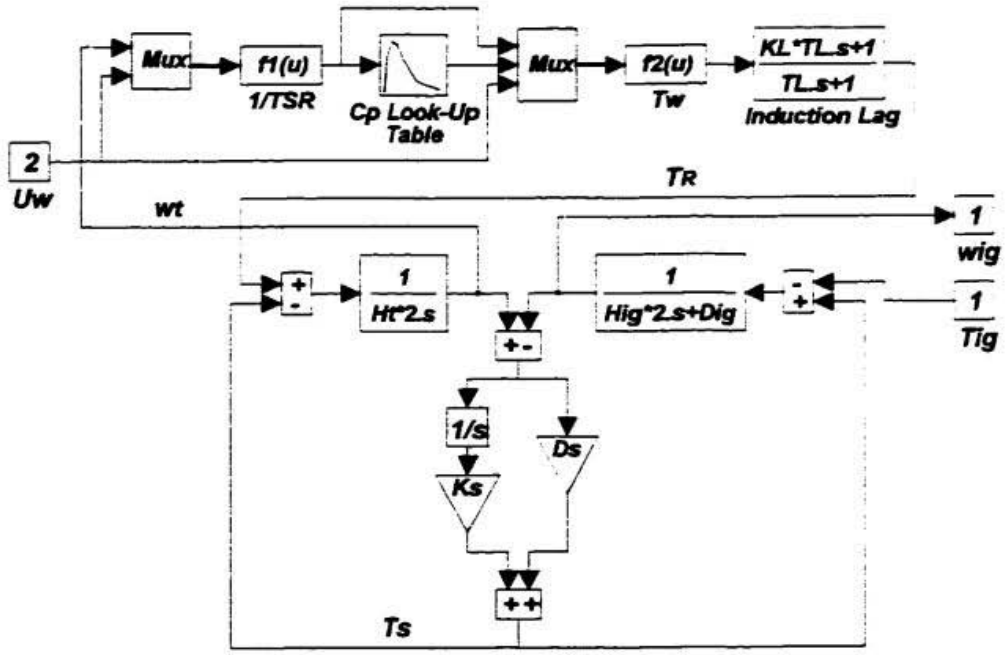

Figure A.12 Wind turbine mechanical model.

A.1.3.3 *AVR* Subsystem for the Wind-Diesel Models

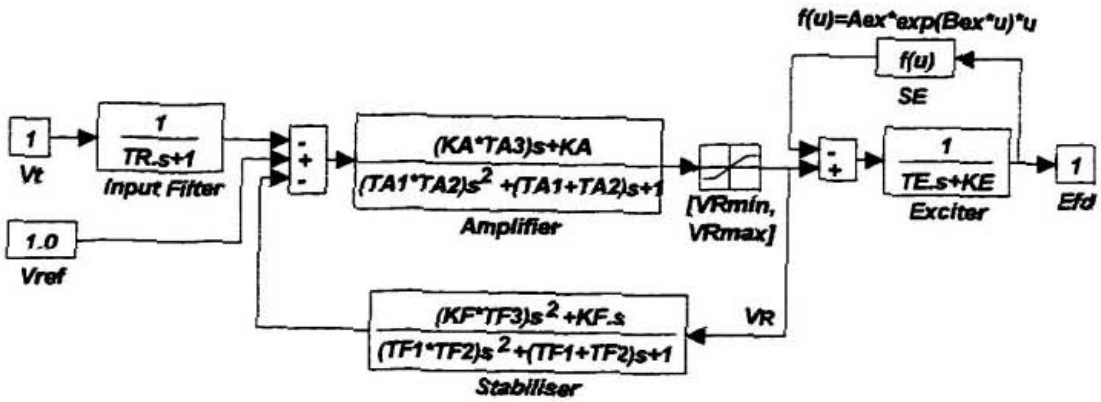

Figure A.13 Excitation system model.

A.2 HPNSWD System Model with SVC

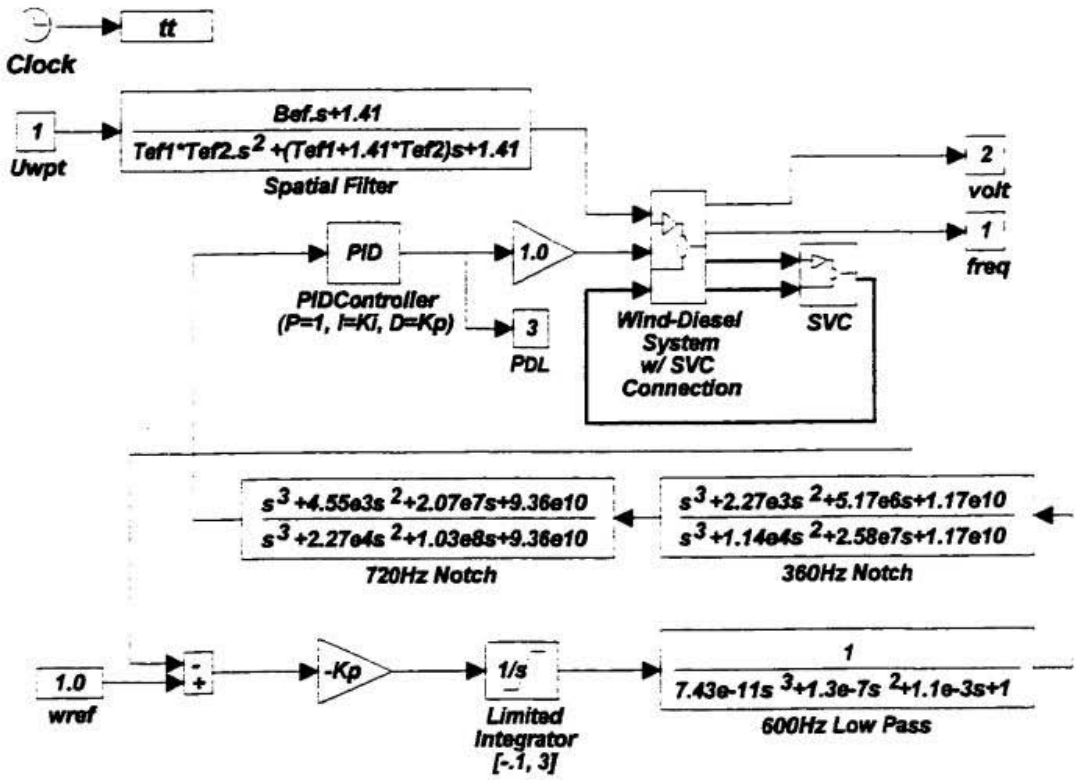

Figure A.14 HPNSWD system with SVC.

A.2.1 Wind-Diesel Subsystem with SVC Connection

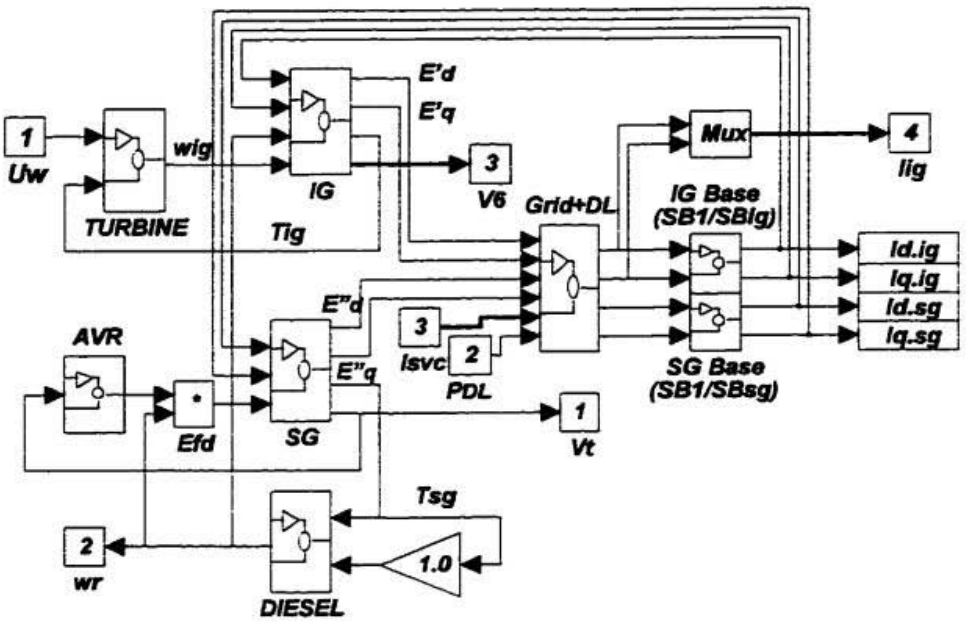

Figure A.15 Reduced-order wind-diesel subsystem with SVC connection.

A.2.1.1 *Grid+DL* Subsystem with SVC Connection

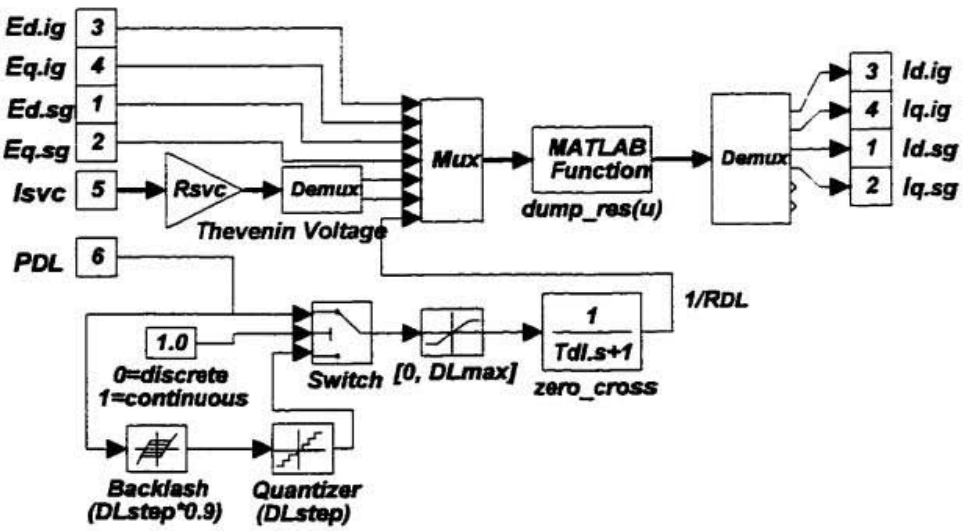

Figure A.16 Network admittance model with SVC connection.

A.2.2 *SVC* Subsystem

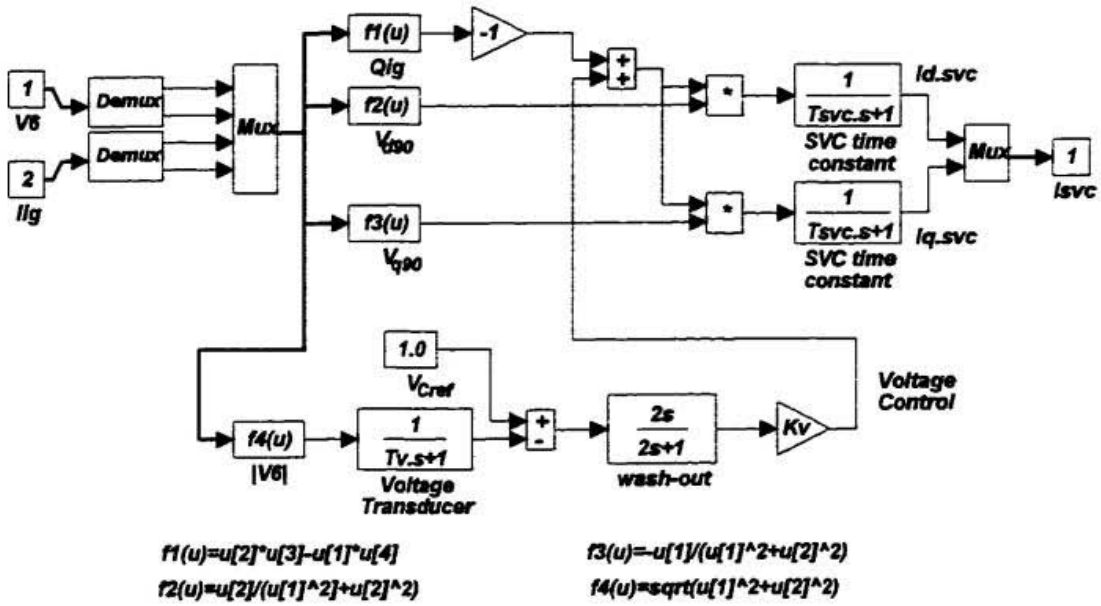

Figure A.17 Static VAR compensator model.

Appendix B

MATLAB Files

B.1 p_wdsys.m - Wind-Diesel Model Parameters

{ } - parameter notation used in the body of the thesis

```
% General System Parameters
wo=2*pi*60;                 % 60Hz system (rad/s)              {ω0}
SB3=100e3;                  % 3-phase VA base (VA)             {SB3}
SB1=SB3/3;                  % 1-phase VA base (VA)             {SB1}
VB=600*sqrt(2/3);           % voltage base, l-n peak (V)       {VB}
IB=SB1*2/VB;                % current base, line peak (A)      {IB}
ZB=VB/IB;                   % impedance base (ohms)            {ZB}


% Synchronous Generator Parameters (Kato KAMAG Brushless)
%     one diesel      two diesels
SBsg=62.5e3/3;          %125e3/3;  % 1-phase VA base (VA)      {SBlsg}
VBsg=VB;                    % voltage base, l-n peak (V)       {VBsg}
IBsg=SBsg*2/VBsg;           % current base, line peak (A)      {IBsg}
ZBsg=VBsg/IBsg;             % impedance base (ohms)            {ZBsg}
Hsg=0.16;                   % inertia constant (pu)            {Hsg}
Dsg=0.03;                   % damping constant (pu)            {Dsg}
Rsg=0.0370;                 % stator resistance @ 125C (pu)    {Rs.sg}
Xdsg=1.902;                 % d synch. react. (pu)             {Xd.sg}
Xqsg=0.805;                 % q synch. react. (pu)             {Xq.sg}
Xtdsg=0.153;                % d transient react. (pu)          {X'd.sg}
Xtqsg=0.805;                % q transient react. (pu)          {X'q.sg}
Xstdsg=0.105;               % d subtr. react. (pu)             {X"d.sg}
Xstqsg=0.097;               % q subtr. react. (pu)             {X"q.sg}
Xlsg=0.062;                 % stator leak. react. (pu)         {Xls.sg}
Ttdo=0.834;                 % d trans. time const. (s)         {τ'd0.sg}
Ttqo=0.167;                 % q trans. time const. (s)         {τ'q0.sg}
Tstdo=8e-3;                 % d subtr. time const. (s)         {τ"d0.sg}
%     adjusted   quoted
Tstqo=35e-3;    %4e-3;      % q subtr. time const. (s)         {τ"q0.sg}
```

```
% constants for reduced-order models
Kqsg=Xqsg-Xstqsg;
K1sg=(Xstdsg-Xlsg)/(Xtdsg-Xlsg);                                    {K1.sg}
K2sg=1-K1sg;                                                        {K2.sg}
K3sg=Xtdsg-Xlsg;
Kdsg=(Xdsg-Xtdsg)*(Xtdsg-Xstdsg)/(Xtdsg-Xlsg)^2;                     {Kd.sg}
Xxd=(Xdsg-Xtdsg)*(Xstdsg-Xlsg)/(Xtdsg-Xlsg);                        {Xxd}

% constants for full-order model
Xmq=Xqsg-Xlsg;                                                      {Xmq.sg}
Xmd=Xdsg-Xlsg;                                                      {Xmd.sg}
Xlkq=Xmq*(Xstqsg-Xlsg)/(Xqsg-Xstqsg);                               {Xlkq.sg}
Xlfd=Xmd*(Xtdsg-Xlsg)/(Xdsg-Xtdsg);                                 {Xlfd.sg}
Xlkd=(Xtdsg-Xlsg)*(Xstdsg-Xlsg)/(Xtdsg-Xstdsg);                     {Xlkd.sg}
Xaq=1/(1/Xmq+1/Xlsg+1/Xlkq);                                        {Xaq.sg}
Xad=1/(1/Xmd+1/Xlsg+1/Xlfd+1/Xlkd);                                 {Xad.sg}
Rfd=(Xmd+Xlfd)/(wo*Ttdo);                                           {Rfd.sg}
Rkq=(Xmq+Xlkq)/(wo*Tstqo);                                          {Rkq.sg}
Rkd=(Xlkd+Xmd*Xlfd/(Xmd+Xlfd))/(wo*Tstdo);                          {Rkd.sg}

% Saturation data
Ag=0.0333;                                                          {AG}
Bg=8.43;                                                            {BG}


% AVR Parameter (Kato KCR-360/Basler SSR 32-12)
TR=0.011;                % input filter time const. (s)             {τR}
KF=0.01;                 % stabilizer gain                          {KF}
TF1=0.075;               % stabilizer time const. (s)               {τF1}
TF2=0.5;                 % stabilizer time const. (s)               {τF2}
TF3=0;                   % stabilizer time const. (s)               {τF3}
KA=870;                  % amplifier gain                           {KA}
TA1=0.036;               % amplifier time const. (s)                {τA1}
TA2=10;                  % amplifier time const. (s)                {τA2}
TA3=0.2;                 % amplifier time const. (s)                {τA3}
KE=1;                    % exciter  constant                        {KE}
TE=0.03;                 % exciter time const. (s)                  {τE}
VRmax=7.5;               % maximum AVR output (pu)
VRmin=0;                 % minimum AVR output (pu)
Aex=0.0027;              % exciter saturation                       {AEX}
Bex=1.04;                % exciter saturation                       {BEX}
```

```
% Governor (Barber-Colman DYNA I & DYNA II) & Diesel Engine
% (Volvo D70CRC 6 cylinder, 4 stroke, 75kW @ 1800rpm)
Tac=75e-3;                  % actuator time constant (s)      {τac}
TD=0.019;                   % engine dead-time (s)            {τD}
TDmin=-0.5;                 % minimum torque (pu)
TDmax=1.2;                  % maximum torque (pu)
Hd=0.579;                   % inertia  constant (pu)          {Hd}
Dd=0.03;                    % damping  constant (pu)          {Dd}
Kdr= 0.04;                  % droop (pu)                      {Kdr}
Tdr= 1.4;                   % droop time constant (s)         {τdr}
d0=-0.13;d1=1.17;d2=0.073;d3=-0.109;  % torque fit
wdref=1.0;                  % governor reference speed        {ωdref}
%     Diesel A+B      Diesel A    % governor constants
Tz1= 0.33;              %0.35;    % zero (s)                  {τz1}
Tz2= 0.05;              %0.55;    % zero (s)                  {τz2}
Tp1= 0.01274;           %0.005;   % pole (s)                  {τp1}
Tp2= 0.01026;           %0.02;    % pole (s)                  {τp2}
Kg=   18.2;             %4.75;    % gain                      {Kg}


% Asynchronous Generator Parameters (Westinghouse)
PBig=66e3;                  % power base (W)                  {PBig}
SBig=PBig/3;                % VA base, 1-phase (VA)
VBig=480*sqrt(2/3);         % voltage base, l-n peak (V)      {VBig}
IBig=SBig*2/VBig;           % current base, line peak (A)     {IBig}
ZBig=VBig/IBig;             % impedance base (ohms)           {ZBig}

Rsi=0.0092;                 % stator resistance (pu)          {Rs.ig}
Rri=0.017;                  % rotor resistance (pu)           {Rr.ig}
Xlsi=0.0459;                % stator leakage react. (pu)      {Xls.ig}
Xlri=0.0623;                % rotor leakage react. (pu)       {Xlr.ig}
%     unsaturated     saturated
Xmi=  3.59;             %2.657;   % mag. react. (pu)          {XM.ig}
Xadi=1/(1/Xmi+1/Xlsi+1/Xlri);                               {Xad.ig}

% reduced-order model constants
Xig=Xlsi+Xmi;               % open circuit react. (pu)        {Xig}
Xtig=Xlsi+Xmi*Xlri/(Xmi+Xlri); % transient react (pu)        {X'ig}
Ttoig=(Xlri+Xmi)/(wo*Rri);  % transient time const. (s)      {τ'0.ig}

% saturation data, from Choi & Larkin [65]
Agi=0.0975;                                                 {AG}
Bgi=6.93;                                                   {BG}
```

```
% rotor - Atlantic Orient AOC 15/50
Uavg=8;                 % average wind speed (m/s)
Rt=7.5;                 % radius (m)                          {Rt}
wt0=6.6;                % base speed (rad/sec)                {ωt0}
Ht=2.0;                 % rotor inertia constant              {Ht}
Ks=576;                 % low speed shaft spring const.       {KS}
Ds=2.9;                 % low speed shaft damping const.      {DS}
KL=1.37;                % induction lag gain                  {KL}
TL=4*Rt/Uavg;           % induction lag time constant         {τL}
Kr=0.5*1.225*pi*Rt^3*wt0/PBig; % torque constant, p=1.225kg/m^3

% Cp look-up table: RST=1/TSR
RST=[.0747 .101 .105 .123 .137 .149 .161 .173 .183 .193 ...
     .205 .218 .238 .266 .316 .35 .4 .45 .5 .53];
CP=[0 .303 .328 .407 .441 .456 .451 .436 .429 .418 .392 ...
     .357 .302 .236 .155 .111 .0733 .0511 .0366 .0310];

% Effective Windspeed - spatial filter
aef=0.55;                                                   {aef}
Bef=1.3*Rt/Uavg;                                            {Bef}
Tef1=Bef*sqrt(aef);
Tef2=Bef/sqrt(aef);

% Dump Load
TDL=0.5/(wo/(2*pi));    % delay of 1/2 cycle (s)            {τDL}
DLstep=1.5e3/SB3;       % 1.5kW steps @ Vt=1 (pu)
DLmax=190e3/SB3;        % 190kW maximum load @ Vt=1 (pu)

% Transmission Line (1kV 4/0 gauge buried cable)
Rtl=0.191;              % ohms/km                           {RTL}
Xtl=0.082;              % ohms/km                           {XTL}
SBtl=SB1;               % same as system (VA)               {SBTL}
VBtl=600*sqrt(2/3);     % volt base l-n peak (V)            {VBTL}
IBtl=SBtl*2/VBtl;       % current base, line peak (A)       {IBTL}
ZBtl=VBtl/IBtl;         % impedance base (ohms)             {ZBTL}

% Capacitor Bank
%   no cap.     30kVA
Xcb=-1e6;       %-12;   % reactance (ohms)

% Transformers
Xtrig=0.01;             % 480/600V                          {XTRig}

% Static VAR Compensator (SVC)
Tsvc=4e-3;              % time constant (s)                 {τsvc}
```

```
Rsvc=1e3;              % thevenin resistance (pu)          {Rsvc}
Kv=10;                 % voltage control gain               {Kv}
Tv=5e-3;               % volt transducer time const. (s)    {τv}

% Village Load
RL=10;                 % series resistance (pu)             {RL}
XL=0;                  % series reactance (pu)              {XL}
```

B.2 `dump_res.m` - Dump Load MATLAB Function

This MATLAB function is called in SIMULINK (*Grid+DL* subsystem) to calculate the nodal currents from the given bus voltages and dump load power setting for the equivalent (reduced) admittance matrix. If the dump load setting has changed since the last function call, it also updates the full and equivalent admittance matrices.

```
function [Ibus] = dump_res(VbusDL)
global KMTX LMTX LTMTX MMTX YDL DL0 Yfull
% Input:  port voltages and dump load power setting (PDL)
% Output:  port currents
% This function calculates the network's output currents from the
% network's input voltages. If the dump load setting has changed
% it will update the full and equivalent (reduced) admittance
% matrices.
nn=size(VbusDL,1);          % get size of input vector

if VbusDL(nn)~=DL0          % only calculate if load has changed
 Gdl=VbusDL(nn);            % dump load conductance (pu)= PDL (pu)
 Mdl=MMTX;                  % adjust admittance matrix
 Mdl(1,1)=Mdl(1,1)+Gdl; Mdl(2,2)=Mdl(2,2)+Gdl;
 YDL=KMTX-LMTX*inv(Mdl)*LTMTX;   % equivalent admittance matrix
 Yfull(nn:(nn+3),nn:(nn+3))=Mdl; % full admittance matrix
 DL0=VbusDL(nn);            % update last dump load value
end;

Ibus=YDL*VbusDL(1:(nn-1)); % return port currents
```

B.3 yb_svc.m - Admittance Matrix Calculation (with SVC)

MATLAB program to calculate the full and equivalent (reduced) admittance matrices. This version includes the SVC connection (i.e., 3 port network). The dump load impedance is omitted from this calculation and added later by the function dump_res.m.

```
% AWTS System with SVC
% Diesel(node#1) - WT(node#2) - Village(node#3) - SVC(node#9)

clear KMTX LMTX LTMTX MMTX YDL Yfull
global KMTX LMTX LTMTX MMTX YDL DL0 Yfull

% calculate branch admittances

% diesel(node#1) to village junction(node#4)
r14=Rsg*SB1/SBsg+Rtl*0.02/ZBtl;
xd14=Xstdsg*SB1/SBsg+Xtl*0.02/ZBtl;
xq14=Xstqsg*SB1/SBsg+Xtl*0.02/ZBtl;
g14=r14/(r14^2+xd14*xq14);
b14d=-xd14/(r14^2+xd14*xq14);
b14q=-xq14/(r14^2+xd14*xq14);

% WT(node#2) to WT transformer(node#6)
r26=Rsi*SB1/SBig;
x26=Xtig*SB1/SBig;
g26=r26/(r26^2+x26^2);
b26=-x26/(r26^2+x26^2);

%SVC(node#9) to WT transformer(node#6)
g69=1/Rsvc; b69=0;

% capacitor bank(node#6)
g60=0; b60=-1/(Xcb/ZB);

% village junction(node#4) to WT transformer(node#6)
r46=Rtl*0.05/ZBtl;
x46=Xtl*0.05/ZBtl+Xtrag;
g46=r46/(r46^2+x46^2);
b46=-x46/(r46^2+x46^2);

% Village(#4)
```

```
r40=RL+Rtl*0.01/ZBtl;
x40=XL+Xtl*0.01/ZBtl;
g40=r40/(r40^2+x40^2);
b40=-x40/(r40^2+x40^2);

% define Yfull (full admittance matrix)
G11=g14; B11d=b14d; B11q=b14q; G12=0; B12=0;
G14=-g14; B14d=-b14d; B14q=-b14q; G16=0; B16=0; G19=0; B19=0;
G22=g26; B22=b26; G24=0; B24=0; G26=-g26; B26=-b26; G29=0; B29=0;
G99=g69; B99=b69; G49=0;B49=0; G69=-g69; B69=-b69;
G44=g40+g14+g46; B44d=b40+b14d+b46; B44q=b40+b14q+b46; G46=-g46;
B46=-b46;
G66=g60+g26+g46+g69; B66=b60+b26+b46+b69;


Yfull=[G11   -B11q  G12   -B12   G19   -B19  G14   -B14q G16   -B16;...
       B11d   G11   B12    G12   B19    G19  B14d   G14   B16    G16;...
       G12   -B12   G22   -B22   G29   -B29  G24   -B24   G26   -B26;...
       B12    G12   B22    G22   B29    G29  B24    G24   B26    G26;...
       G19   -B19   G29   -B29   G99   -B99  G49   -B49   G69   -B69;...
       B19    G19   B29    G29   B99    G99  B49    G49   B69    G69;...
       G14   -B14q  G24   -B24   G49   -B49  G44   -B44q G46   -B46;...
       B14d   G14   B24    G24   B49    G49  B44d   G44   B46   G46;...
       G16   -B16   G26   -B26   G69   -B69  G46   -B46   G66   -B66;...
       B16    G16   B26    G26   B69    G69  B46    G46   B66   G66];

% define Ybus (3 port equivalent admittance matrix)
KMTX=Yfull(1:6,1:6);
LMTX=Yfull(1:6,7:10);
LTMTX=Yfull(7:10,1:6);
MMTX=Yfull(7:10,7:10);

Ybus=KMTX-LMTX*inv(MMTX)*LTMTX;

% initial dump load setting to ensure that the dump load gets
% calculated by the first dump_res.m execution
DL0=10;
```

Appendix C

Bode Plots for Dump Load Frequency Control

The wind-diesel system is considered to be the plant in the dump load frequency control loop. The plant's input is the dump load power setting (in per unit), and the plant's output is the system frequency (in per unit). Linear state-space models of the wind-diesel system are extracted around the specified operating points using SIMULINK's *linmod* function [18]. The Bode plots are generated using the *bode* function in MATLAB's *Controls Toolbox* [17].

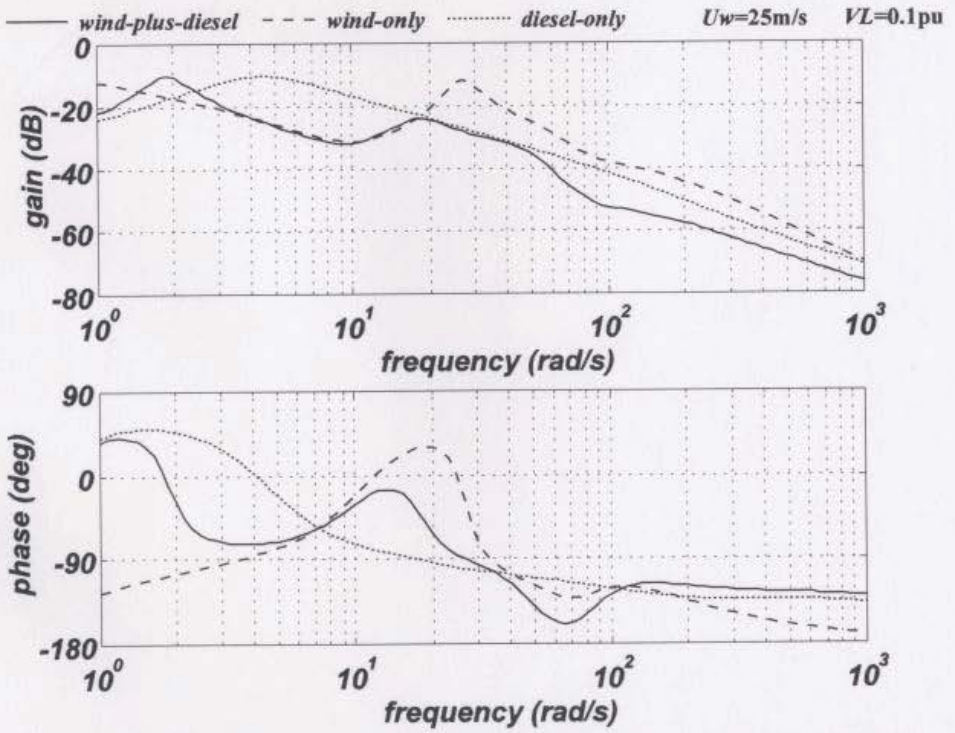

Figure C.1 Bode diagram of the plant configurations at U_w=25m/s.

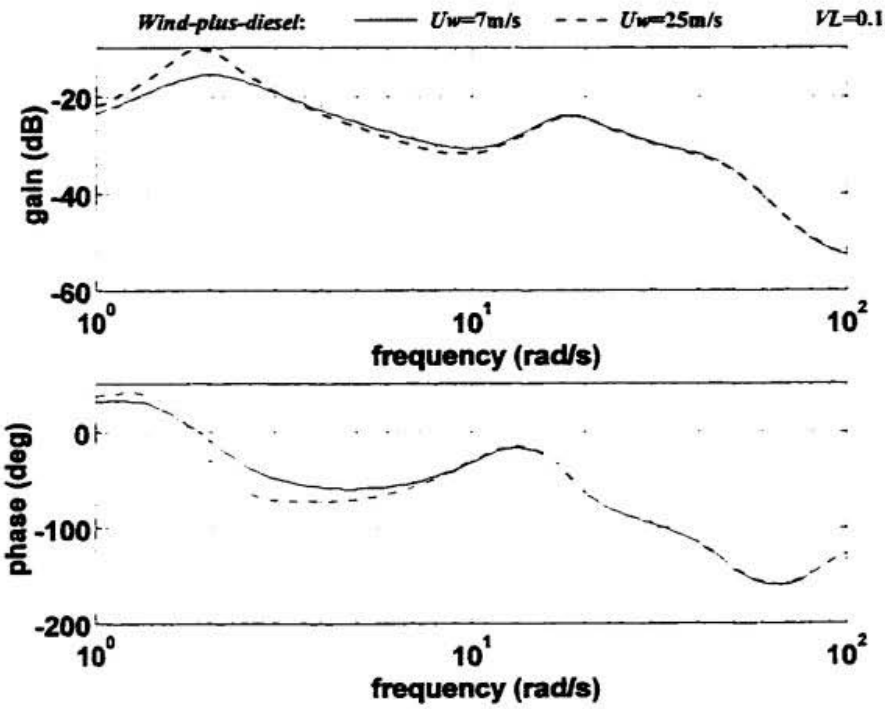

Figure C.2 Bode diagram of *wind-plus-diesel* configuration.

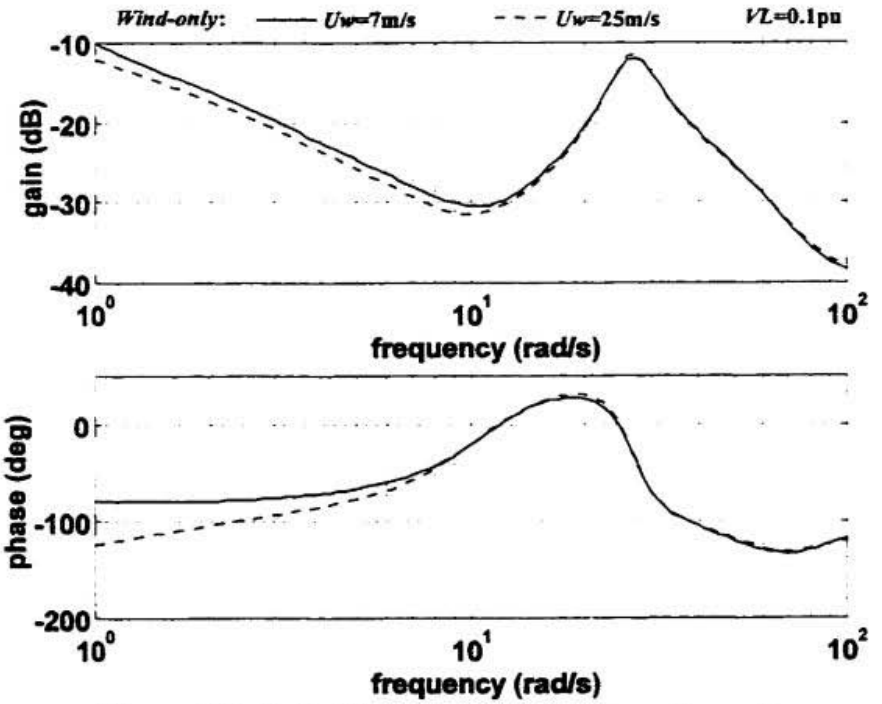

Figure C.3 Bode diagram of *wind-only* configuration.

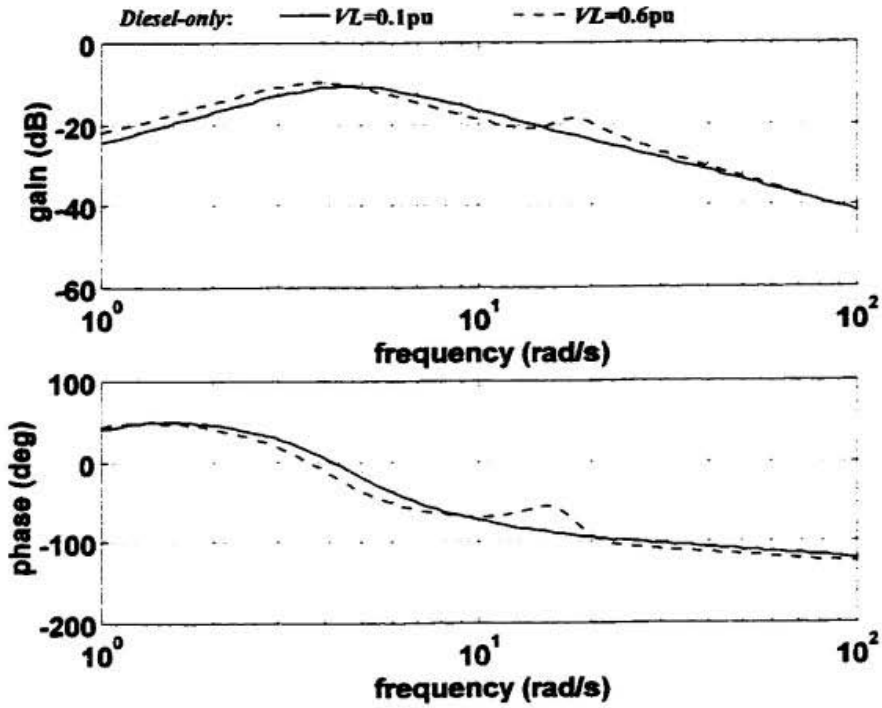

Figure C.4 Bode diagram of *diesel-only* configuration.

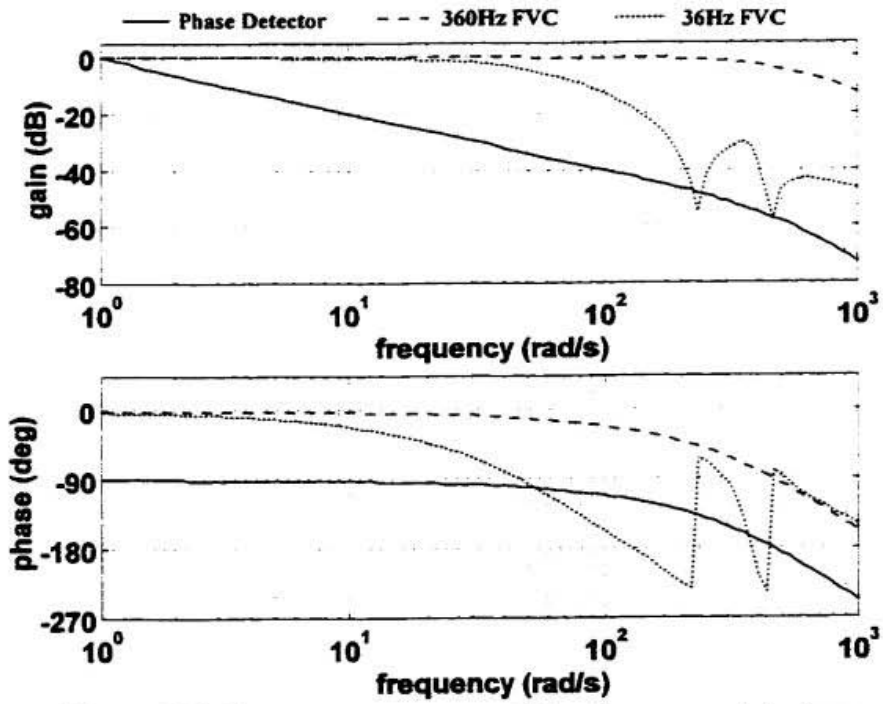

Figure C.5 Frequency response of the frequency detectors.

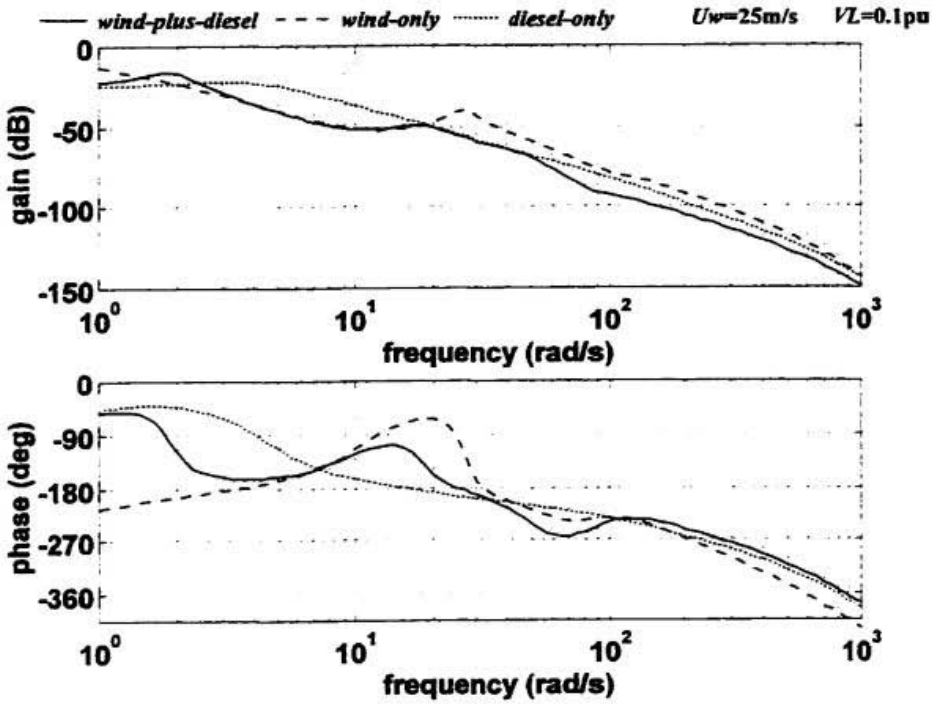

Figure C.6 Bode plot of the plant plus the phase detector.

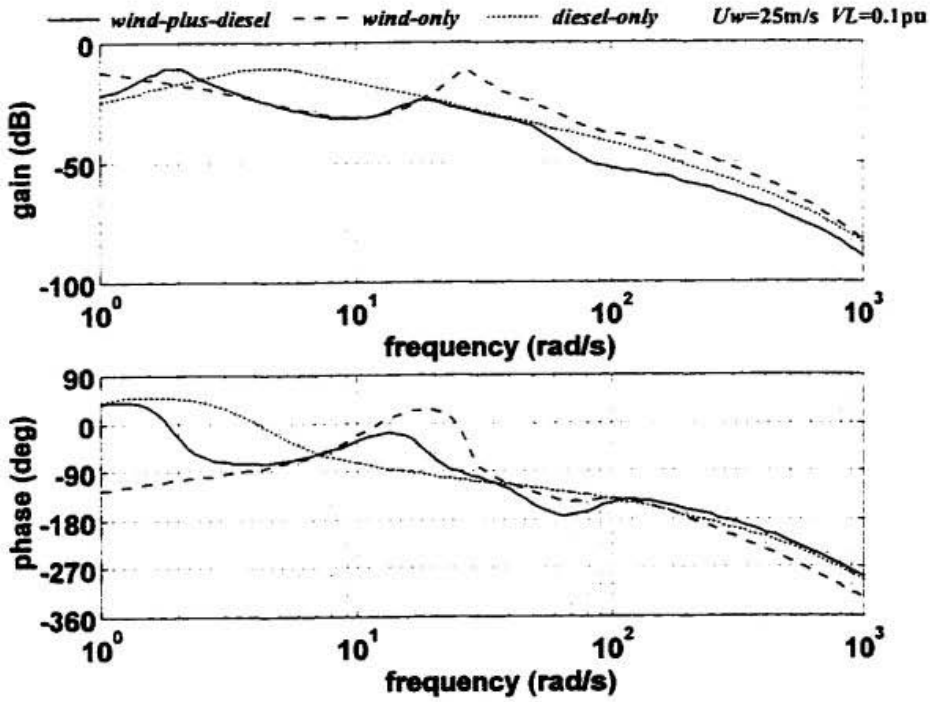

Figure C.7 Bode diagram of the plant plus the 360Hz FVC.

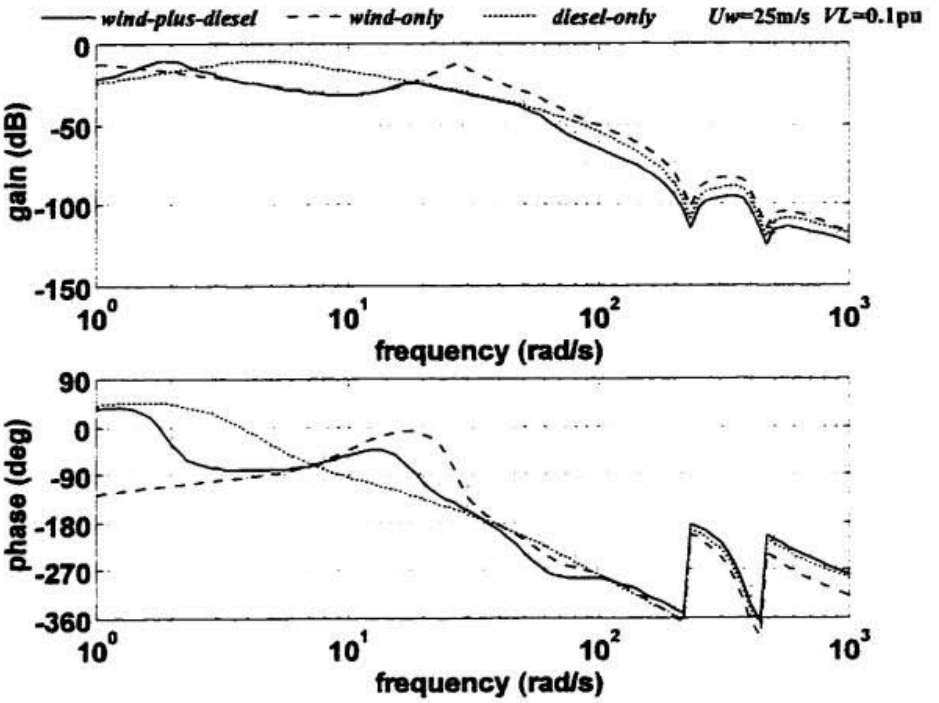

Figure C.8 Bode diagram of the plant plus the 36Hz FVC.

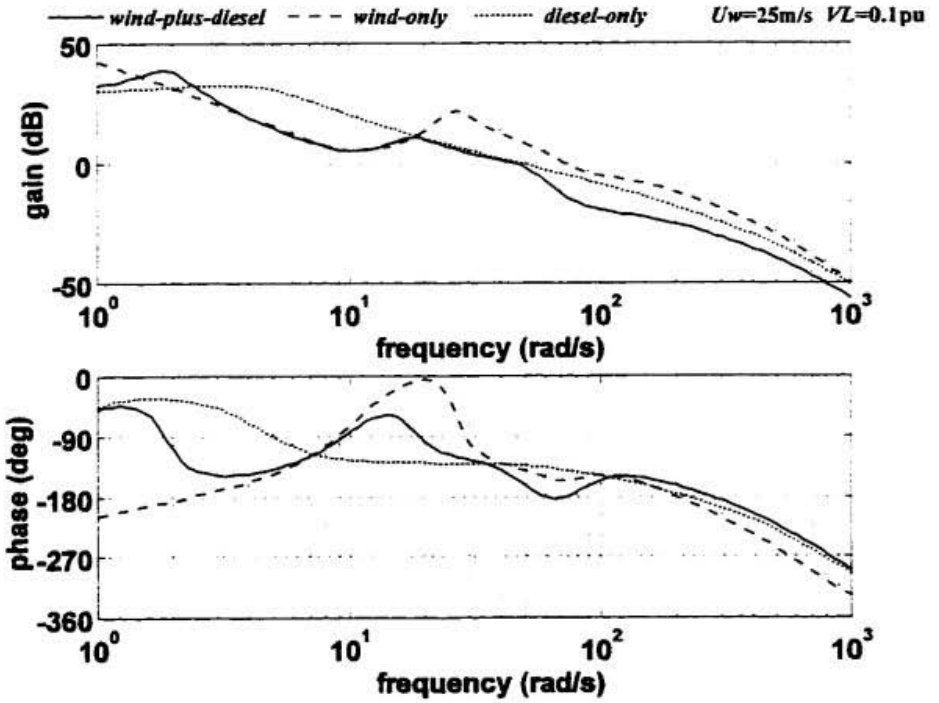

Figure C.9 Phase control with Ziegler-Nichols PI parameters.

Appendix D

Per-Phase Wind Turbine

Disconnection

The per-phase electrical model is based on the simulation of opening phase *a* of a 3-phase induction machine described in Krause [57]. Each phase of the wind turbine's 3-phase induction generator is opened by a zero-crossing relay (ZCR) when its respective current crosses zero. The SIMULINK model of the ZCR is shown in Figure D.2. Full-order models of both the induction generator and the synchronous generator are used. The induction generator is simulated in the stationary reference frame (i.e., $\omega = 0$). While the synchronous generator is simulated in its rotor reference frame, which is assumed to be rotating at nominal speed (i.e., $\omega_r = 1.0$). With phase *a* open-circuited and phases *b* and *c* still connected on the induction generator, the phase *a* current, $I_{a.ig}$, is zero and the induction generator's phase *a* open circuit voltage is given by Krause [56] as

$$V_{a.igO} = \frac{X_{M.ig}}{\omega_0 (X_{lr.ig} + X_{M.ig})} \frac{d\psi^s_{qr.ig}}{dt} \tag{D.1}$$

Since the induction generator is connected by a 3-wire system there can be no zero-

sequence currents. Therefore the remaining two phase voltages seen by the induction generator are

$$V_{b.ig} = V_{b.sg} - V_{ng} \tag{D.2}$$

$$V_{c.ig} = V_{c.sg} - V_{ng} \tag{D.3}$$

where,

$$V_{ng} = \frac{1}{2}(V_{b.sg} + V_{c.sg}) + \frac{1}{2}V_{a.igO} \tag{D.4}$$

Phases *b* and *c* cross zero current and open simultaneously since, with only two wires connected, the two phase currents must be equal but opposite.

Refer to Figures D.1 through D.4 for the SIMULINK implementation of the per-phase wind turbine disconnection.

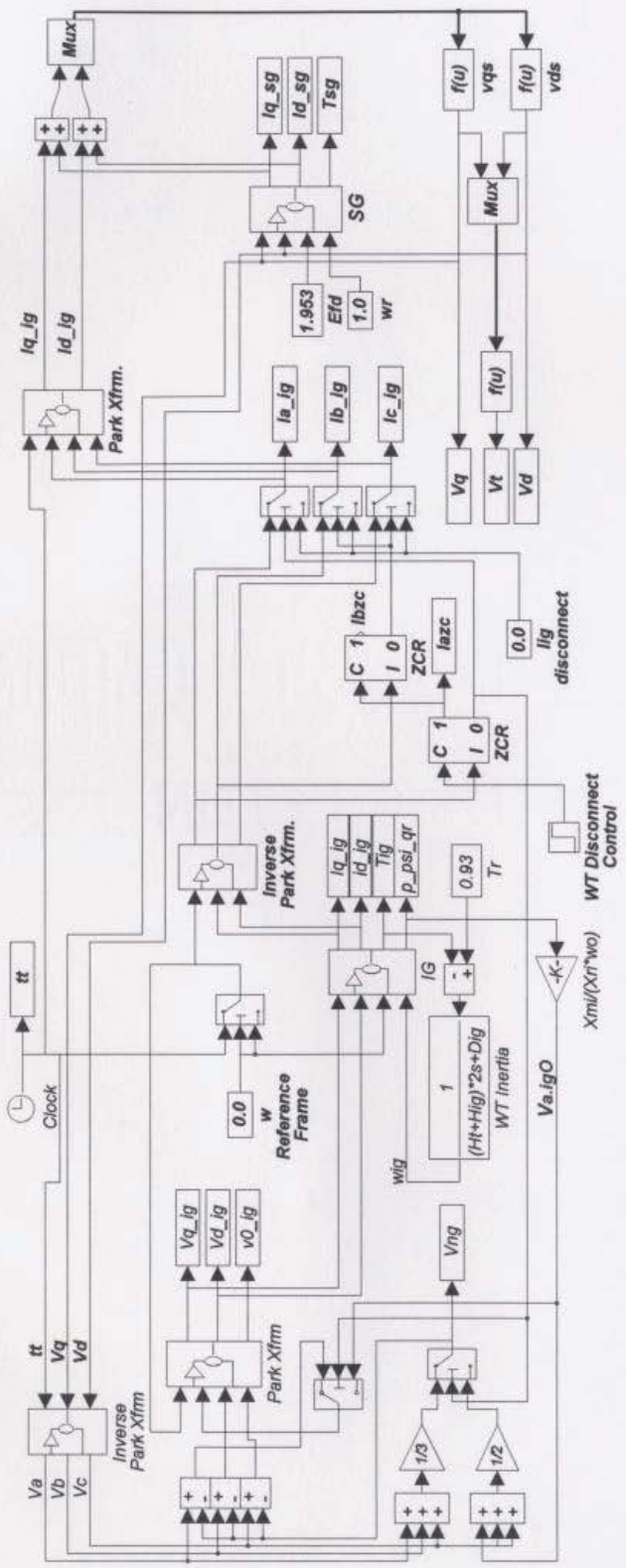

Figure D.1 Per-phase electrical wind-diesel model.

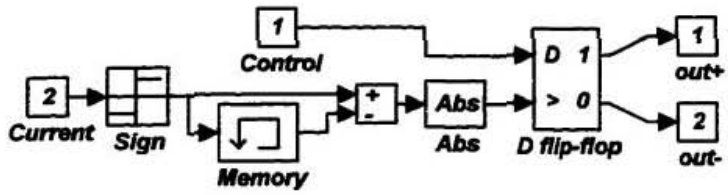

Figure D.2 Zero -crossing relay subsystem.

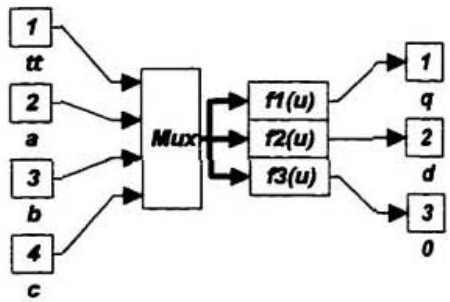


```
f1(u)=2/3*(u[2]*cos(wo*u[1])+u[3]*cos(wo*u[1]-2*pi/3)+u[4]*cos(wo*u[1]+2*pi/3))
f2(u)=2/3*(u[2]*sin(wo*u[1])+u[3]*sin(wo*u[1]-2*pi/3)+u[4]*sin(wo*u[1]+2*pi/3))
f3(u)=2/3*(u[2]*0.5+u[3]*0.5+u[4]*0.5)
```

Figure D.3 Park transformation subsystem.

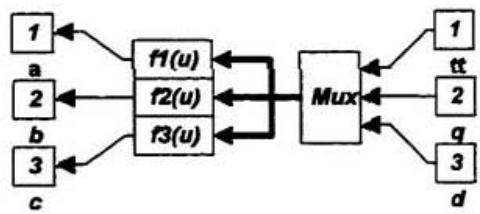


```
f1(u)=u[2]*cos(wo*u[1])+u[3]*sin(wo*u[1])
f2(u)=u[2]*cos(wo*u[1]-2*pi/3)+u[3]*sin(wo*u[1]-2*pi/3)
f3(u)=u[2]*cos(wo*u[1]+2*pi/3)+u[3]*sin(wo*u[1]+2*pi/3)
```

Figure D.4 Inverse Park transformation subsystem.